Numerical Modelling of Dielectric Barrier Discharge Plasma Dynamics in Pure and Multi-Species Fluids

by

Mitchell Andrew Collett

A thesis submitted to the Faculty of Graduate and Postdoctoral Affairs

in partial fulfillment of the requirements for the degree of

Master of Applied Science

in

Aerospace Engineering

Carleton University

Ottawa, Ontario, Canada

January 2022

Abstract

Dielectric barrier discharge (DBD) plasma actuators have been shown to influence several features of surrounding flow fields. This work models DBD plasma generation and movement in quiescent fluids. The work is restricted to plasma dynamics and does not consider the impact on the bulk flow field. A model is developed for an asymmetrically oriented DBD at 1200 V, in atmospheric conditions, operating within pure gases of N_2, H_2, CO_2, CO, and H_2O, along with various mixtures including a simplified post-combustion environment. Charged particle densities are dependent on rates of ionization and recombination, and simulations show ion densities up to $10^{21}\,\mathrm{m}^{-3}$. Plasma velocity is dominated by ion mobility, with averages between $3.90\,\mathrm{mm\,\mu s}^{-1}$ and $11.59\,\mathrm{mm\,\mu s}^{-1}$. Plasma in mixtures is found to exhibit certain qualities of each constituent species, but is generally governed by the major components of the mixture.

Acknowledgements

The completion of this work would not have been possible if not for the assistance of several groups and individuals. I would first like to express my great appreciation to Dr. Jason Etele for his guidance, mentorship, and invaluable advice throughout my time at Carleton University. My questions and concerns were consistently met with eagerness and patience, and the insight you provided during our many discussions was immensely helpful.

I wish to acknowledge Aliaksandr Murzionak for developing the foundation of this research and for offering his much appreciated expertise. I would also like to extend my gratitude to Carleton University and the Department of Mechanical and Aerospace Engineering for offering me the opportunity to pursue this degree.

Finally, a special thanks to my family for their constant encouragement, to the Thompson family for welcoming me into their home in Ottawa, and to Alexandra Held for her unwavering support and enthusiasm.

Table of Contents

List of Tables

List of Figures

List of Acronyms

Acronym	Definition
AC / DC	Alternating Current / Direct Current
AFC	Active Flow Control
BLC	Boundary Layer Control
CFD	Computational Fluid Dynamics
CO_2 / CO_2^+	Carbon Dioxide / Carbon Dioxide Ion
CO / CO^+	Carbon Monoxide / Carbon Monoxide Ion
DBC	Dirichlet Boundary Condition
DBD	Dielectric Barrier Discharge
DICPCG	Diagonal Incomplete Cholesky Preconditioned Conjugate Gradient
DILUPBiCG	Diagonal Incomplete LU Preconditioned Bi-Conjugate Gradient
EHD	Electro-hydrodynamic
FVM	Finite Volume Method
GCI	Grid Convergence Index
H.O.T	Higher Order Terms
H_2 / H_2^+	Hydrogen / Hydrogen Ion
H_2O / H_2O^+	Water / Water Ion
LOx	Liquid Oxygen
MCC	Monte Carlo Collision
N_2 / N_2^+	Nitrogen / Nitrogen Ion
NBC	Neumann Boundary Condition

PA	Plasma Actuator
PDE	Partial Differential Equation
PIC	Particle-In-Cell
PIV	Particle Image Velocimetry
RP-1	Rocket Propellant-1 or Refined Petroleum-1
rms	Root Mean Square

Nomenclature

Symbol	Definition	Units
$\mathbf{A}$	Coefficient matrix	-
$\mathbf{b}$	Source vector	-
C	Courant/Control number	-
C_p	Specific Heat Capacity	$[\mathrm{J\,K^{-1}\,kg^{-1}}]$
D_k	Diffusion coefficient of particle k	$[\mathrm{m^2\,s^{-1}}]$
$\boldsymbol{E}$	Electric field	$[\mathrm{V\,m^{-1}}]$
E	Total Energy	[J]
E_i	Estimated fractional error of i^{th} grid	-
$\boldsymbol{F}$	Vector field	-
F_s	Safety factor	-
f_i	Numerical solution of i^{th} grid	-
e_i	Discretization error of i^{th} grid	-
e_0	Elementary charge	$[1.602 \times 10^{-19}\,\mathrm{C}]$
$\boldsymbol{g}$	Gravitational acceleration	$[9.8067\,\mathrm{m\,s^{-2}}]$
h_i	Normalized spacing of i^{th} grid	-
k	Thermal conductivity	$[\mathrm{W\,m^{-1}\,K^{-1}}]$
k_B	Boltzmann constant	$[1.3806 \times 10^{-23}\,\mathrm{J\,K^{-1}}]$
$\mathbf{M}$	Pre-conditioner matrix	-
N	Number density	$[\mathrm{m^{-3}}]$
$\boldsymbol{n}$	Surface normal vector	-
P	Pressure	[Pa or Torr]

Pr	Prandtl Number	-
p	Order of convergence	-
$\boldsymbol{q}$	Heat flux vector	$[\mathrm{W\,m^{-2}}]$
q_k	Electric charge of particle k	[C]
r	Grid refinement ratio	-
$\mathbf{r}$	Residual vector	-
S_k	Source term of particle k	$[\mathrm{m^{-3}\,s^{-1}}]$
s_k	Charge sign of particle k	-
T	Temperature	[K]
t	Time	[s]
$\boldsymbol{U}, \boldsymbol{u}$	Velocity	$[\mathrm{m\,s^{-1}}]$
V	Volume	$[\mathrm{m^3}]$
$V_{dr,e}$	Electron drift velocity	$[\mathrm{m\,s^{-1}}]$
X	Atom/molecule	-
$\mathbf{x}$	Solution vector	-
y	Number density fraction	-
α	Ionization coefficient	$[\mathrm{m^{-1}}]$
β	Recombination rate coefficient	$[\mathrm{m^3\,s^{-1}}]$
$\boldsymbol{\Gamma}$	Species flux	$[\mathrm{m^{-2}\,s^{-1}}]$
γ	Secondary emission coefficient	-
δ	Surface charge delta	[0 or 1]
ε	Relative error	-
ϵ	Absolute permittivity	$[\mathrm{F\,m^{-1}}]$
ϵ_0	Absolute permittivity of a vacuum	$[8.8541 \times 10^{-12}\,\mathrm{F\,m^{-1}}]$

ϵ_r	Relative permittivity	-
ζ	Degree of Ionization	-
λ_d	Debye Length	[m]
μ_k	Mobility of particle k	$[\mathrm{m^2\,V^{-1}\,s^{-1}}]$
μ_v	Dynamic viscosity	[Pa s]
ρ	Density	$[\mathrm{kg\,m^{-3}}]$
ρ_c	Volume Charge Density	$[\mathrm{C\,m^{-3}}]$
σ_c	Surface charge density	$[\mathrm{C\,m^{-2}}]$
$\boldsymbol{\tau}$	Deviatoric stress tensor	-
Φ, φ, ϕ	Electric potential	[V]
∇	Del or nabla operator	-

Subscripts

c	Electric charge
e	Electrons
i	$i^{\,th}$ species
i/j	Mesh or Matrix cell indices
k	Electron, positive ion or negative ion
n	Neutral
pp	Peak-to-Peak
$+$	Positive ions
$-$	Negative ions
$\perp$	Perpendicular

Chapter 1

Introduction

1.1 Dielectric Barrier Discharge

Plasma, typically referred to as the fourth classical state of matter, makes up over 99% of the visible universe. Plasma has proven to be useful in everyday applications including television, neon or fluorescent lights and welding, while being extensively researched in a wide range of scientific fields. The study of dielectric barrier discharge (DBD) has become of recent interest to the aerospace community in the form of DBD plasma actuators. Specifically, DBD plasma actuators have demonstrated the promising capability of active flow control in fluid dynamics. Plasma actuators are beneficial in that they are lightweight, exhibit fast response time, and are entirely electronic thus require no moving parts, enabling them to be utilized in a variety of applications.

Plasma actuators can be arranged in a number of configurations, all of which yield unique modifications to the surrounding flow field. One of the most often studied configurations is that of the asymmetrical flat-plate surface dielectric barrier discharge (SDBD) plasma actuator, illustrated in Figure 1.1. Consisting of two parallel-plate electrodes, one exposed to the working fluid, the other embedded beneath a dielectric barrier, the plates are oriented such that the embedded electrode is downstream of the exposed electrode, i.e. asymmetric. By supplying a high-voltage to the electrodes,

a strong electric field is generated above the surface of the dielectric. At a sufficient electric potential the gas will become ionized by means of Townsend Discharge, and a region of plasma is formed. The electrically charged particles within the plasma are subject to the electrodynamic force exerted by the external electric field. As these charged particles are accelerated through the electric field, they collide with the neutral background gas resulting in a transfer of momentum, and the fluid in the vicinity of the actuator is altered. The actuator in Figure 1.1 generates a wall-parallel jet along the surface of the dielectric, but other configurations can generate different flow-field effects, such as wall-normal jets, anti-parallel jets, and vortices.

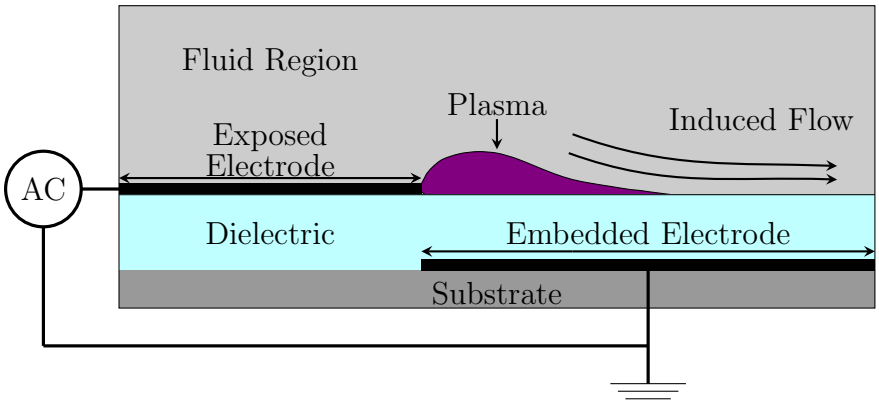

Figure 1.1: Conventional configuration of an SDBD plasma actuator with the induced flow directed away from the exposed electrode along the dielectric surface.

1.2 Problem Statement

Both experimental and numerical studies concerned with DBD actuation are vital components in progressing the application of plasma actuators. Experimental studies are abundant, and provide extensive evidence for the benefits of plasma actuation,

whereas numerical studies offer valuable insight into the mechanisms of plasma actuation without the cost of experimentation. Much of the research done on DBD plasma actuators, numerical or experimental, is carried out in an air or air-like environment, typically pure nitrogen or an 80:20 nitrogen-oxygen mixture. In an effort to expand the applicability of the DBD actuator, this work models the generation of plasma in atypical fluids, specifically those that would be commonly found in a post-combustion environment. While the composition of exhaust can vary widely depending on the fuel/oxidizer used, the exhaust of the SpaceX Merlin 1D+ engine was chosen as the working fluid, which employs a RP-1 kerosene fuel with a LOx oxidizer. On a mass basis, the main components of exhaust are carbon monoxide, water vapor, molecular hydrogen and carbon dioxide (CO, H_2O, H_2, CO_2) [1]. By simulating each of these pure gases in a DBD actuator domain, the influence of their individual properties on the plasma characteristics can be determined. The modelling is then extended to various mixtures of said gases to analyze the interaction of multiple species. Pure nitrogen is modelled as a means of validation while also offering a standard by which other species can be consistently compared. Despite the function of DBD actuators as active flow control modules, the scope of this work is limited to plasma dynamics rather than the interaction between plasma and the bulk flow field.

Chapter 2

Literature Review

2.1 Review

Research into DBD plasma actuators (PA) has become extensive in recent years and the broad range of applications of such devices has led to ample results in both experimental and numerical modelling. Flow control can generally be separated into two categories: passive flow control and active flow control. Passive flow control is focused on geometry and materials modification such as winglets, riblets and fluid-solid interface materials. Active flow control (AFC) devices require an auxiliary power source and include suction or blowing devices, synthetic jets and DBD PAs. Possible AFC applications for DBD actuators include, but are not limited to, flow separation control, reduced fuel consumption and noise reduction [2]. Kriegseis, Simon and Grundmann [3] offer a thorough review of the research, applicability and feasibility of DBD PAs, discussing the various requirements DBD actuation must meet to become practical instruments in the aerospace field.

The study of DBD PAs in quiescent air and the induced wall-jet is a thoroughly researched topic aimed at understanding the momentum transfer effects of DBD actuation. Though the results cannot be directly transferred (superimposed) to real, non-quiescent flow due to the non-linearity of the flow field [3], the research is nevertheless important in comparison of data or validation of numerical modelling. It

has been found that wall-jet velocity in quiescent air is on the order of a few $\mathrm{m\,s^{-1}}$ and no more than $8\,\mathrm{m\,s^{-1}}$ [4, 5]. In non-quiescent flow, velocity profile modification shows promise in boundary layer control (BLC), as additional momentum is known to change the stability properties in the near-wall region [3]. Figure 2.1 illustrates one of many possible velocity profile modifications near the dielectric surface as a result of the induced wall-jet. Several studies have shown that PAs are able to delay laminar to turbulent transition by 50 to 300 mm [6–9].

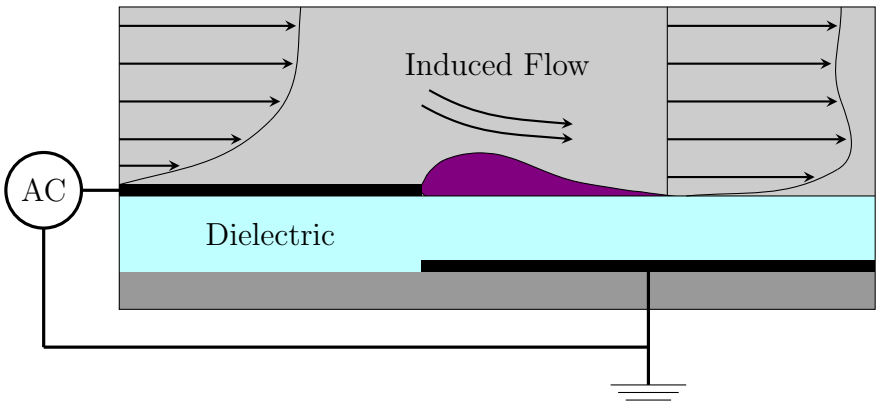

Figure 2.1: Conventional configuration of an SDBD plasma actuator with induced wall-jet altering the velocity profile downstream of the actuator's exposed electrode.

The review of Kriegsreis et al. [3] points out that while PA technology has verified potential in BLC and the reduction of energy consumption for future aircraft, there are two major challenges facing DBD PAs used for AFC: limited force production and inefficient momentum transfer. While these disadvantages may be overcome with the advancement of PA technology, there is also a complex relationship between the plasma dynamics and the environment in which it operates. With changes to pressure, temperature, humidity, etc. comes significant changes to the performance of the actuator. As such, this work is aimed at furthering the understanding of

plasma dynamics in varying species to explore the feasibility of plasma actuators in alternative environments.

2.2 Numerical Modelling

Alongside the abundance of experimental research on DBD actuation, numerical modelling may be applied in various ways to understand the function of plasma actuation without using costly experimental procedures. Accurate and reliable numerical modelling is a crucial component in the advancement of DBD plasma actuators. Numerical modelling of dielectric barrier discharge is often categorized into 3 types: phenomenological, kinetic and fluid models.

Phenomenological models are not derived from first principles, but instead describe empirical relationships that are in agreement with fundamental theories. These models establish a relationship between parameters and variables, but do not attempt to explain why they interact in such a way. In the study of DBD plasma and its effect on flow fields, phenomenological models estimate the body force within the Navier-Stokes equations, though the method for this estimation varies for different models.

A kinetic approach, such as particle-in-cell (PIC), analyzes the effect on the flow by accounting for the interaction of particles and the resulting transfers of momentum, heat, etc. These models often use "superparticles", a collection of large numbers of individual particles that are modelled as a single entity in an effort to reduce computational cost. However, kinetic models remain relatively complex and are less common in the study of DBD simulation, typically limited to 1-D or 2-D simulations.

A fluid approach models the plasma as a multi-fluid species by looking at macroscopic quantities such as velocity, density or flux. The complexity of the fluid composition can vary from a simple two-element, electron-ion fluid, to a comprehensive fluid consisting of all unique elements present. Because additional species greatly increases the computational cost, complex fluid models are usually restricted to 1-D or 2-D, and rarely used for 3-D simulations. However, fluid models are valuable in that they retain the fundamental physics involved while remaining relatively computationally efficient.

Modelling is predominately focused on the standard configuration shown in Figure 1.1, in which flow field actuation is intended to induce downstream velocity through momentum transfer. Though there are a wide range of alternative configurations in which the actuators may be arranged, the literature discussed here will refer to the standard configuration unless otherwise specified.

2.2.1 Phenomenological Models

Shyy, Jayarama and Andersson

The study of Shyy et al. [10] models the paraelectric force as a body force in the weakly ionized plasma region to understand the resulting flow field and heat transfer effects. The electric field is simplified such that the field strength decreases linearly as one moves away from the edge of the exposed electrode, allowing for a model of the electric field to be obtained without a detailed computation. The plasma region then coincides with this linearized electric field. This linearized electric field is expressed

as:

$$|\boldsymbol{E}| = E_0 - k_1 x - k_2 y \tag{2.1}$$

$$E_0 = \frac{V}{d} \tag{2.2}$$

where V is the applied voltage, d is the separation of the electrodes in the x direction, and coefficients k_1 and k_2 are governed by the plasma height and length along with the breakdown electric field strength, taken from experiments.

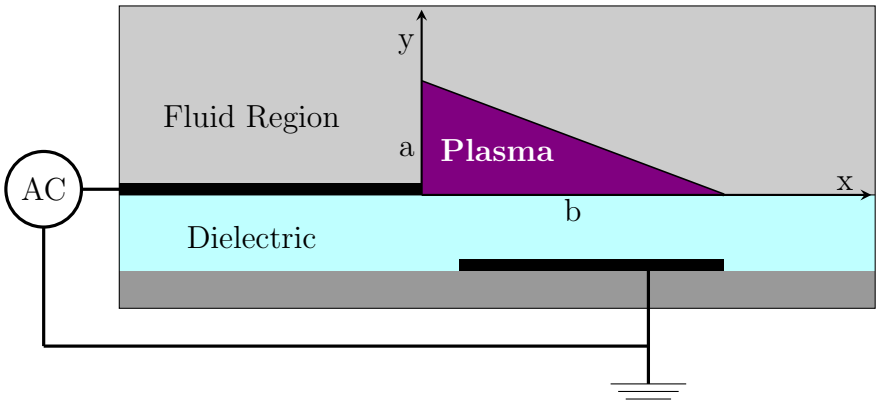

Figure 2.2: Linearized electric field modelled by Shyy et al. The electric field outside the triangular region is not strong enough to ionize the fluid.

Figure 2.2 illustrates the linearized plasma region. The height, a, is taken to be 1.5 mm, and the width, b, to be 3 mm. While the electric field strength is not constant within this region, the charge density is assumed a constant $10^{11}\,\mathrm{cm}^{-3}$. This is then used to model the body force generated in flows over a 20.5 mm flat plate with freestream velocities ranging from 2–10 $\mathrm{m\,s}^{-1}$. Several simulations are performed for various applied AC voltage functions of 3–5 kV rms and 2–6 kHz.

As expected, the work finds that a wall-jet flow is induced by the ion-neutral

interactions, showing significant changes in the velocity profiles and heat transfer effects depending on freestream velocity, applied voltage magnitude and frequency. These findings are consistent with experimental findings cited by Shyy et al [11–14]. Peak wall-jet velocity is shown to vary linearly with both magnitude and frequency of the applied voltage, and that the relative effect of the wall-jet is more pronounced for lower freestream velocities. It is suggested that alterations to the electrode shape and operating conditions could further optimize the influence the plasma has on the flow field.

Suzen and Huang

The model created by Suzen and Huang [15] estimates the body force in the Navier-Stokes equations using the electrohydrodynamic (EHD) force expressed as

$$\boldsymbol{f}_s = \rho_c \boldsymbol{E} \tag{2.3}$$

where $\boldsymbol{f}_s$ is the body force per unit volume, ρ_c is the charge density (which, unlike in Shyy et al., is no longer assumed constant), and $\boldsymbol{E}$ is the electric field. The magnetic field is considered negligible, and Maxwell's equations are reduced to:

$$\nabla \times \boldsymbol{E} = 0 \tag{2.4}$$

implying that the electric field can be derived as a gradient of a scalar potential function:

$$\boldsymbol{E} = -\nabla \Phi \tag{2.5}$$

Gauss's law is then be expressed as:

$$\nabla \cdot (\varepsilon \nabla \Phi) = -\rho_c \tag{2.6}$$

where ε, the permittivity, is the product of the relative permittivity of the medium, ε_r, and the permittivity of free space, ε_0,

$$\varepsilon = \varepsilon_r \varepsilon_0 \tag{2.7}$$

This work also mentions that the force, $\boldsymbol{f}_s$, plays a large role in the modification of the flow field but the temperature rise and viscosity reduction should also be considered to fully understand the role of plasma in actuation.

In this model, the relative permittivity of air is $\varepsilon_r = 1.0$, and for the chosen dielectric material of Kapton, the relative permittivity is $\varepsilon_r = 2.7$. The potential, Φ is assumed to be decoupled into the potential due to the external electric field, φ, and the potential due to the net charge density, ϕ: $\Phi = \varphi + \phi$. When applied to Equation 2.6, two equations for the potential are expressed as:

$$\nabla \cdot (\varepsilon_r \nabla \varphi) = 0 \tag{2.8}$$

$$\nabla \cdot (\varepsilon_r \nabla \phi) = -(\rho_c / \varepsilon_0) \tag{2.9}$$

The applied electric field governs φ, while the potential due to charge density, ϕ, is

dependent on the Debye length, λ_d, such that:

$$\phi = (-\rho_c \lambda_d^2 / \varepsilon_0) \tag{2.10}$$

$$\nabla \cdot (\varepsilon_r \nabla \rho_c) = \rho_c / \lambda_d^2 \tag{2.11}$$

To model the charge density along the wall, experimental results found that the distribution could be represented by a half-Gaussian, rather than a linear distribution employed by Shyy et al. [10], governed as follows:

$$G(x) = \exp\Big[\frac{-(x-\mu)^2}{2\sigma^2}\Big] \tag{2.12}$$

The use of this half Gaussian allows a gradual decay of the charge density from the left to right edge of the electrode, where a value of $\sigma = 0.3$ was chosen.

A square wave of amplitude 5 kV and frequency of 4.5 kHz is applied to the exposed electrode. The work is able to show that flow is pulled into the region above the embedded electrode and accelerated to the right, with a maximum velocity of $1\,\mathrm{m\,s^{-1}}$. It also shows that the charge density is greatest at the region above the left corner of the embedded electrode, as per the half-Gaussian distribution, which agrees with the plasma profile shown in experiments. However, the model is tested against a single experiment in order to validate the approach, and would need to be calibrated further by using more experimental data. The charge density is not calculated but rather prescribed to agree with experimental results, in which the maximum charge density is $0.0008\,\mathrm{C\,m^{-3}}$.

Brauner, Laizet, Benard and Moreau

Brauner et al. [16] mentions the simplified models of Orlov [17], Shyy [10] and Suzen and Huang [15, 18], but also highlights the limitations of such models for their time-independence and/or their reliance on corrections needed to agree with experimental results. This work builds upon the Suzen and Huang model but instead implements a sinusoidal wave to understand the effect of an AC driving frequency. The following parameters are used to validate the phenomenological model and were in agreement with Suzen and Huang, though a sine wave AC voltage function is used rather than the square wave of Suzen and Huang. The model is then further validated by simulating the starting vortex experimentally generated by Whalley and Choi [19, 20].

Table 2.1: Parameters employed to validate the model.

ε_{r1}	ε_{r1}	$\phi^{\max}$ (kV)	f_{AC} (kHz)	λ_d (mm)	$\rho^{\max}$ ($\mathrm{C\,m^{-3}}$)
1.0	2.7	5	4.5	0.17	7.5×10^{-3}

The work found that the assumption made by Suzen and Huang, that the wall-normal component of induced body force can be neglected, is not representative of a realistic simulation of a DBD plasma actuator. Their attempt to extract an experimental model from particle image velocimetry (PIV) data was promising for simulation of a DBD plasma actuator in quiescent fluid, and provides a better match to experimental data than the Suzen and Huang model. However, neither model was able to accurately predict the thickness of the wall-jet close to the actuator. Further, the Suzen and Huang model could be improved upon by limiting the extent of the plasma along the embedded electrode, as it has been determined that the plasma generally does not extend along the entire length.

Khoshkoo and Jahangirian

Khoshkhoo and Jahangirian [21] study the effect of single and multiple plasma actuators, and the induced body forces, for a NACA0015 airfoil. These plasma body forces created by multiple DBD actuators are modelled using a phenomenological plasma method coupled with 2D compressible flow equations. The body force distributions are assumed to vary linearly in the triangular region around the actuator, as assumed in the Shyy model [10].

The model is solved using a time-implicit finite volume method on an unstructured grid, and the response of separated flow is studied in the presence of different numbers of DBDs, which are then compared to a verified model with zero DBDs present. The control model (0 DBDs) is verified with a comparison to the experimental data of Jayaraman and Shyy [22]. Various configurations are simulated to better understand the optimal number of actuators to be used, and their placement along the airfoil. Optimization is determined by the mean lift and drag coefficients, by which a maximum lift to drag ratio is indicative of optimal plasma actuation. The study found that for low angles of attack, flow separation is optimized with a single actuator, medium angles of attack optimized with 2-3 actuators, and high angles of attack optimized with 4 or more actuators. It was also found that decreasing the distance between the first and second actuators improves the aerodynamic coefficients, which provides valuable insight on the benefit of PAs on a real airfoil. It is worth noting that power consumption must also be considered when discussing optimization, thus the total power supplied to the series of actuators is kept constant.

Ibrahim and Skote

A study by Ibrahim and Skote [23] modifies the Suzen and Huang model to account for the dielectric shielding that occurs when a charge density accumulates along the dielectric surface. The work looks at a non-conventional configuration of plasma actuators positioned on the top and bottom of channel flow, as shown in Figure 2.3.

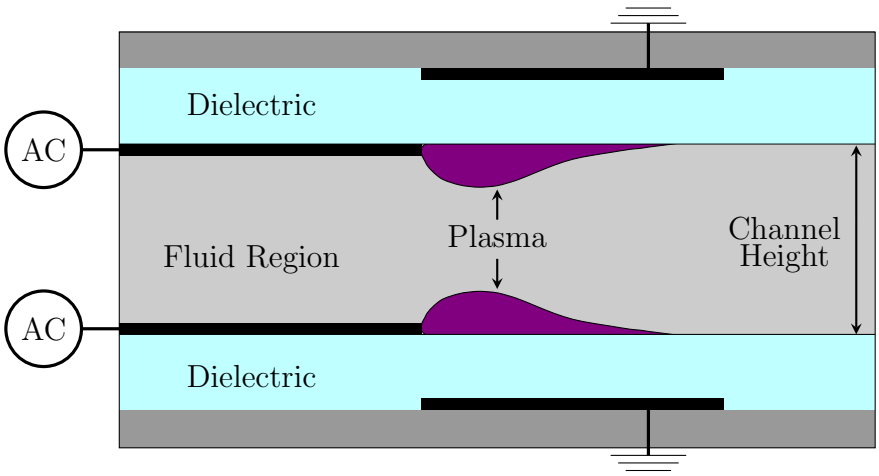

Figure 2.3: Mirrored actuators in channel flow configuration. Channel height varied from 0.004 to 0.03 m.

The model is able to accurately predict the maximum flow velocity induced by the actuators within channels at heights of 0.02 and 0.03 m. Additionally, the model is able to distinguish the 2 velocity peaks that are generated in larger channel heights. For smaller channel heights, the peaks merge into a single core flow, as predicted by Poiseuille flow, but the model underestimates the maximum velocities. However, this unique study may provide a valuable baseline for considering the use of DBD PAs within a post-combustion environment, such as the exhaust flow through a narrow channel of a turbine engine, or a small rocket exhaust passage. The model developed

by Suzen and Huang, as a phenomenological model, does not detail the air chemistry, and thus the composition of a post-combustion fluid would have to be considered if the work of Ibrahim were to be adapted for such an application.

Babou, Martin, Peña

As mentioned, different actuator configurations may also be modelled to illustrate the unique flow field alterations achieved by DBD actuators. Babou et al. [24] models a flipped actuator configuration, in which two standard DBD actuators are mirrored along the wall-normal axis, shown in figure 2.4

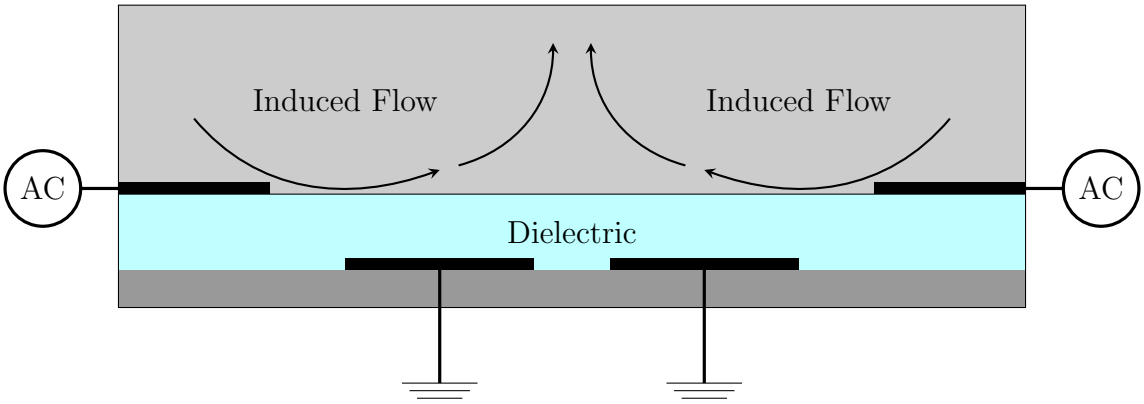

Figure 2.4: Two actuators mirrored along the wall-normal axis, designed to pull fluid in toward the middle and produce a wall-normal jet.

Similar to the conventional configuration, this flipped actuator induces a wall-normal jet with peak velocities that increase with increasing applied voltage magnitude. Additionally, the separation between the two actuators has a non-negligible effect on the peak wall-normal jet velocity, where a 3 mm gap between the two results in a nearly 20% increase to the peak velocity at 5 mm above the dielectric surface. It is suggested that this model can be used to further explore the optimal separation

required to induce maximum velocity in the jet.

2.2.2 Kinetic Models

Font and Morgan

Previous methods had demonstrated the ability to model boundary layer control in pure nitrogen, while the work of Font and Morgan [25] extends the simulation to oxygen, and more importantly, to negative oxygen ions. The presence of negative ions is worth noting because they add momentum in the opposite direction as positive ions and will diminish the net force imparted on the background flow. Due to oxygen's lower ionization energy (12.06 eV for oxygen, 15.6 eV for nitrogen), plasma in air is thought to be dominated by the ionization of oxygen.

The work first considers the charge density of the plasma for a single bias oscillation in which the exposed electron is subject to a square wave of $\pm$ 5200 V, while the embedded electrode is maintained at 0 V. The frequency is not specified but is low enough to ensure the discharge will extinguish before the polarity of the electrodes is reversed, corresponding to a frequency in the 1-10 MHz range. Thus, for the first half-cycle, the exposed electrode is held at -5200 V, and negative particles are pushed downstream towards the dielectric, while positive particles are pulled upstream toward the exposed electrode. When polarity is reversed for the second half-cycle, the negative particles are pulled upstream, while the negative ions are pushed downstream. It is found that when the exposed electrode is negatively biased, there will be a net momentum transfer toward this exposed electrode in a direction opposite that of the freestream flow, and a net momentum transfer toward the embedded electrode

in the same direction as the freestream flow when the electrode is positively biased. This result is attributed to two reasons: 1) the electrons have a small collision cross section and small mass, leading to a diminished momentum transfer, and 2) the positive ions outnumber the negative ions by a factor of 2, implying that the positive ions dominate the direction of net momentum transfer. However, the total force produced when the exposed electrode is positively biased is greater by a factor of at least 10 due to an increased overall charge density, as the negative charges will rest on the dielectric surface at the end of the first half-cycle, but are completely neutralized by the exposed electrode at the end of the second half-cycle. Thus, over the entire bias cycle, there is a net momentum transfer downstream toward the embedded electrode, in the same direction as the freestream flow. The work finds that since the plasma is quasi-neutral, in the limiting case that the negative and positive ions are equally populous, there would be a minimum net force of zero, so the presence of negative ions can never reverse the net force direction.

The importance of this study is to determine the effect of negative ions in DBD plasma actuators, and it was found both in experiment and simulation that the presence of negative ions results in a greater force imparted on the freestream flow. Though the simulations were unable to produce the correct magnitudes of force found in experiment, there was agreement in the increased force production in the presence of oxygen, and that the rate at which force increases with increased voltage is more noticeable in the presence of oxygen. It is worth noting that the discharge lasts tens of nanoseconds, not long enough for neutral particles to move a significant distance, so their motion is not considered. Also, because the study models a single bias cycle, the accumulation of plasma products such as dissociated or meta-stable particles are

not modelled.

Ebato, Ogino and Ohnishi

The work of Ebato et al. [26] employs a Particle-In-Cell (PIC) method to model the plasma and electric field interaction, with a Monte Carlo Collision (MCC) method to model interaction between the plasma and neutrals. Both one and two-dimensional simulations are used to model the plasma behaviour in nitrogen, argon and carbon dioxide, selected to expand the application of DBD PAs to a Martian environment.

In the 1-D simulations, thrust generated by the PA in CO_2 and N_2 is found to be dependent on ambient pressure. A 2000 V, 13.56 MHz square wave is applied to the exposed electrode in a weakly ionized gas, initialized with an electron density of $10^{-7}\%$ that of the neutral particle density. Simulations are then run for ambient pressures ranging from 10-100 kPa. While kinetic simulations can be difficult to compare to phenomenological or fluid models, the work finds that ion densities of N_2^+ and CO_2^+ are on the same order of magnitude ($10^{17}\,m^{-3}$). Though levels of ionization are much lower than other works, these results are presented for 15 kPa, far lower than atmospheric pressure commonly modelled.

2.2.3 Fluid Models

Boeuf and Pitchford

A fluid model developed by Boeuf and Pitchford [27] considers a nitrogen-like gas composed of two charged species, electrons and positive ions, while assuming the temperature and atmospheric pressure of the gas are constant. The force acting on

the neutral particles is a result of the collisions of the electrons and ions with neutral molecules, which transfer momentum to the neutral gas. The model is intended to obtain a rough description of the DBD's impact on flow control and the forces acting on the neutral gas, and thus is not compared to specific experimental results. The study finds that the model is consistent with analytical solutions of momentum transfer and that the force imparted on the neutral gas is only significant in the sheath, i.e. the leading edge of the plasma cloud. The sheath propagates with a velocity of 3-5 mm µs^{-1}, and imparts a high intensity of force of 10^9 N m^{-3}. However, given the fast propagation of the sheath, this force only acts for a very short amount of time. At 1 kHz, the force per unit volume averaged in time is only about 10^3 N m^{-3}, a result comparable to the force of surface corona discharges.

Abdollahzadeh, Páscoa, Oliveira

Abdollahzadeh et al. [28] use the configuration of Boeuf and Pitchford [27] as a preliminary validation case in their study of nano-second pulse actuators. A 0.1 mm exposed electrode and a 0.4 mm embedded electrode are separated by a 0.05 mm Kapton dielectric layer ($\varepsilon = 10$) and supplied a constant 1200 V. The streamer discharge observed is comparable to Nishida and Abe [29] and Boeuf and Pitchford [27], with peak ion densities on the order of 10^{21} m^{-3}. The work notes that the concentration of charges along the dielectric increase the electric potential and extend the electrode to the plasma sheath. As expected, the work confirms that the largest electric field is located at the point of highest ion density, thus increasing the rate of ionization in the plasma sheath. The work then goes on to illustrate the micro-shock wave generated by a 5 kV nanosecond actuator, in which rapid heating of the fluid

near the surface causes a compression wave to travel away from the surface. These micro-shock waves are shown to modify main flow features.

Murzionak, Etele and Pimentel

Murzionak et al. [30] also uses the configuration of Boeuf and Pitchford [27] to model plasma actuation in supersonic flow over a 50 ns time frame. The domain is restricted to within the boundary layer and thus it is assumed that the bulk flow velocity is negligible compared to the velocity of charged particles. The model is verified for quiescent flow, in which charge density and plasma velocity are comparable to previous works, though current density along the charged electrode is overestimated in the first 20 ns, before reaching agreeable values. This initial simulation is then compared to shocks present in supersonic flow of Mach numbers 1.3, 1.5 and 2.0, in which the shock is located 50 µm downstream of the exposed electrode. In all cases, the plasma front reaches the shock at roughly 20 ns, after which the ionization process is inhibited and the downstream progression of the plasma front is reduced. The effect is more pronounced as the Mach number increases. At Mach 1.3, the pressure and temperature change does not entirely extinguish the ionization process, and the plasma front is still able to propagate along the dielectric surface, though at a reduced rate. For Mach 1.5 and 2.0, the ionization process is quickly halted, and the charge density drops off rapidly. This result is reflected in the current density along the exposed electrode dropping to $0\,\mathrm{A\,m^{-1}}$ shortly after the plasma reaches the shock.

Mushyam, Rodrigues and Pascoa

A model developed by Mushyam et al. [31] uses a three-module plasma-fluid model to simulate 2D flow over a DBD actuator. A potential model solves the Poisson equation for the electric field in the fluid and dielectric domain. After the electric field is resolved, charge distribution equations are solved to model the evolution of charged particles, by which the EHD body force generated by the DBD can be calculated. Lastly, the two-dimensional incompressible Navier-Stokes equations solve the fluid flow, with the EHD body force included.

The potential model is tested a $5\,\mathrm{kV_{pp}}$ for frequencies of 2000 Hz and 4500 Hz, and found to be in good agreement with the studies of Kotsonis et al. [32] and Suzen et al. [18]. The plasma model was validated by using a voltage of $10\,\mathrm{kV_{pp}}$ at 5000 Hz and comparing the results with experimental discharge currents. The study found good agreement between the model and the experiments. Results were also compared with an empirical model based on the Debye length. The fluid model was then validated by simulating incompressible channel flow, which generated a characteristic, parabolic velocity profile.

The coupling of the three modules was then simulated for an AC power source of $10\,\mathrm{kV_{pp}}$, 4500 Hz, and results showed good agreement with the work of Suzen et al. [18]. The fluid is considered air with a mixture of oxygen and nitrogen molecules, though it is mentioned that the humidity of the air not considered. The model employs a time step of $2 \times 10^{-8}\,\mathrm{s}$, faster than previous empirical numerical studies, where a non-uniform staggered grid based finite volume approach eliminates the need for a very fine grid in resolving the flow. This makes the model faster and more computationally efficient. The model is successful in generating agreeable results

concerning discharge current, streamline plots and quiescent flow evolution.

Nishida and Abe

Nishida and Abe [29] model nitrogen plasma evolution in a configuration similar to Boeuf and Pitchford [27], then extend the 1.2 kV constant applied voltage to various waveforms. The constant positive 1.2 kV voltage yields electron and ion densities on the order of $10^{20}\,\mathrm{m}^{-3}$ within the first 0.1 µs, with plasma propagation extending to 1.6 mm. Increased applied voltages of 1.4, 1.6 and 1.8 kV are shown to extend both the streamer propagation time and speed, thus lengthening the streamer itself, as expected. These results are contrasted to a -1.2 kV applied voltage, in which breakdown quickly occurs near the edge of the negatively charged exposed electrode. Electrons quickly move to the dielectric surface, shielding the electric field inhibiting streamer discharge, after which the plasma diffuses. The structure and evolution of the plasma is entirely different when the exposed electrode is negatively charged and the model supports the notion that downstream momentum transfer during the positive-going half cycle of an AC applied voltage will be the dominant feature of plasma actuation.

Unfer and Boeuf

Unfer and Boeuf [33] model the gas dynamics generated by a 14 kV, 35 ns voltage pulse rather than a constant DC voltage. Air chemistry is not detailed, with modelling consisting of electrons, positive ions and negative ions. Initial charge densities are on the order of $10^{11}\,\mathrm{m}^{-3}$. The work reports electron densities within the first 10 ns of plasma formation to be on the order of $10^{21}\,\mathrm{m}^{-3}$, with a very high propagation of the

plasma streamer. The variation in temperature and pressure following the voltage pulse are also considered, where temperature reaches a localized maximum of 1000 K, and a micro shock wave increases the pressure by about 1000 Pa.

Sato, Takahashi, Ohnishi

In a more recent study, Sato et al. model the actuated flow field in atmospheric air driven by a DC-voltage combined with nanosecond pulses, known as a two-stroke cycle DBD. The 8 kV DC phase accelerates charged particles downstream, while the -8 kV pulses generate charged particles and neutralize the surface charge built up during the DC phase. The charged particles modelled include electrons, positive ions and negative ions, in which the continuity equations are governed by the first Townsend ionization and attachment coefficients, α and η. The study finds that just after the pulse, when ionization occurs, electron and ion densities are on the order of $10^{20}\,\mathrm{m}^{-3}$ in the region adjacent the exposed electrode. The magnitude of these particle densities are maintained for at least 70 ns. As the applied voltage returns to 8 kV DC, electrons are neutralized by the positively charged exposed electrode, where as positive ions remain and begin building a dielectric surface charge. These ions are shown to linger in densities of $10^{19}\,\mathrm{m}^{-3}$ for more than 200 ns. These charge densities are comparable to that of Boeuf and Pitchford, Murzionak et al., and Unfer and Boeuf [27, 30, 33].

Singh and Roy

Singh and Roy [34] provide a model with detailed air-chemistry involving a number of reactions for nitrogen and oxygen, including N_2, N, N_2^+, O_2, O, O_2^+, O^- and electrons.

For a 1.0 kV AC voltage operating at 10 π kHz, charge densities for each individual charged species is on the order of $10^{14}\,\mathrm{m}^{-3}$, much lower than other studies. While the reason for this discrepancy is unclear, plasma structure and movement is similar to other works. The negative ions present are found to decrease the total average force when compared with only positive ions, but the overall direction of the force remains in the downstream direction as positive ions are the dominant species.

Rogier, Dufour and Kourtzanidis

Rogier et al. [35] follow the model introduced by Boeuf and Pitchford [27] and compare the numerical results with those observed by Roy and Durscher [36, 37]. The study focuses on the resulting body force and induced velocity generated. The actuator is driven by a 14 kHz, 21 kV voltage function in quiescent, atmospheric air above a 3 mm dielectric of $\epsilon_r = 3$. Using a refined, structured mesh for the dielectric surface and electrode coupled with a surrounding unstructured mesh, the simulation was carried out for four periods. The time-averaged surface-parallel force is found to be at a maximum at the anode tip and exponentially decreases with increasing distance from the anode. This force is also found to be zero outside of the 1 mm x 1 mm region adjacent the anode tip. In agreement with other studies, the first half-period generates a positive charge density that causes the parallel body force. For a short time (a few µs), the high ion density screens the electric field and ionization is halted, reducing the body force to zero. In the second half-period in which the applied potential is negative, the deposited charges on the dielectric surface create reversed electric field generating a negative-parallel body force for a short time, after which negative ions pushed downstream induce a positive-parallel body force. These positive-parallel

body forces are commonly referred to as a Push-Push scenario. By then running the simulation for various voltage amplitudes, it is found that the body force reaches a threshold maximum for 26 kV, above which the induced velocity does not increase. The study then uses the mean of the time-average body force as a constant source term for a typical flat plate experiment. The induced parallel and perpendicular velocities are in good agreement with the experiments provided, though some discrepancies do arise, namely in the negative-parallel body force in between the push-push cycle.

Dufour and Rogier

The work of Dufour and Rogier [38] models the dynamics of the plasma by resolving the conservation equations for the densities of the species within the plasma. These equations can be written as

$$\partial_t n_i + \nabla_x \cdot (n_i v_i) = S_i \tag{2.13}$$

where n and v represent the i-th density and velocity, respectively. The S term represents the source term accounting for the creation or destruction of charged species. The solver employed by the study uses a mobility law that is dependent on the local flow velocity and induced electric field to determine the species velocity, and can be expressed as:

$$\boldsymbol{v}_i = \boldsymbol{U}_g + \mu_i \boldsymbol{E} + D_i \frac{\nabla_x n_i}{n_i} \tag{2.14}$$

where $\boldsymbol{U}$ is the background flow, $\boldsymbol{E}$ is the electric field, μ is the mobility coefficient and D is the diffusion coefficient for the species. The electric field is then determined by

solving the Poisson equation of charge induced by the species, ρ, the local permittivity of the material, ε, and the electric potential, φ. Dirichlet type boundary conditions are imposed on the electrodes, while Neumann type boundary conditions are imposed on the exterior boundaries of the computational domain. The number of species is limited to electrons and three species: neutrals, positive ions and negative ions. This limits the number of reactions to four. The coefficients are calculated to be consistent with air of 20% oxygen and 80% nitrogen.

The work also details the complications of mesh refinement and time-scale differences. A refined mesh is preferred for precision but can lead to high computational cost when dealing with a domain large enough for the simulation. Thus, two types of meshes are used: structured in the regions requiring precision (i.e. close to the electrodes and dielectric, where gradients are high), and unstructured in regions away from the electrodes where a less-refined mesh is needed. As for the time-scaling, different sub-cycling, Runge-Kutta, splitting, etc. methods are used for the different parts of the plasma model (drift-diffusion, kinetics, Poisson equation).

Under these numerical parameters, a test case is designed with a sinusoidal 21 kV signal of 14 kHz is applied to the exposed electrode with a dielectric permittivity of 3.0. Additionally, a secondary emission coefficient of 10^{-4} is specified to account for the emission of electrons from the cathode and dielectric surface. This case finds very small discrepancies in the body forces when compared to the experimental findings of Roy [36].

The body forces generated are then used in a Navier-Stokes solver to determine the ionic wind, or induced velocity, generated by the model. The order of magnitude and shape of the streamwise velocity profiles are in agreement with experimental data

but finds that the maximum induced velocity is much smaller ($3.5\,\mathrm{m\,s^{-1}}$ computed vs. $5\,\mathrm{m\,s^{-1}}$ measured experimentally). This discrepancy is attributed to the assumption that the source term is constant in time. By splitting the period into tenths and approximating the source term as a piecewise-constant function, the velocity profiles computed are in better agreement with the experimental data.

Chapter 3

General Theory

3.1 Fluid Domain

Fluid dynamics is governed by three laws of conservation. The conservation of mass (Eq. 3.1), momentum (Eq. 3.2) and energy (Eq. 3.3) are commonly expressed as:

$$\frac{\partial \rho}{\partial t} + \nabla \cdot (\rho \boldsymbol{U}) = 0 \tag{3.1}$$

$$\frac{\partial (\rho \boldsymbol{U})}{\partial t} + \nabla \cdot (\rho \boldsymbol{U} \times \boldsymbol{U}) = -\nabla p + \nabla \cdot \boldsymbol{\tau} + \rho \boldsymbol{g} \tag{3.2}$$

$$\frac{\partial \rho E}{\partial t} + \nabla \cdot (\rho \boldsymbol{U} E) + \nabla \cdot (\boldsymbol{U} p) = -\nabla \cdot \boldsymbol{q} + \nabla \cdot (\boldsymbol{\tau} \cdot \boldsymbol{U}) \tag{3.3}$$

However, the scope of this work is focused on plasma dynamics in quiescent fluids, in which the approach to these equations is greatly simplified. Continuity is dealt with in detail following Equation 3.10. In quiescent conditions, under the assumption of constant pressure and temperature, the energy and momentum equations do not need to be updated. As such, much of the focus lies within the electrical parameters of the simulations.

The electromagnetic relationships are governed by Equations 3.4-3.22. In the case of DBD plasma actuators, because there is no external magnetic field, and the current

generated is not sufficient enough to induce an appreciable magnetic field, magnetic forces are not considered. Thus, the electric field can be expressed by Gauss's Law,

$$\nabla \cdot \epsilon \boldsymbol{E} = \rho_c \tag{3.4}$$

where the electric field, $\boldsymbol{E}$, is related to the electric potential, ϕ_E, by

$$\boldsymbol{E} = -\nabla \phi_E \tag{3.5}$$

Gauss's Law can then be rewritten as

$$\nabla \cdot (\epsilon \nabla \phi_E) = -\rho_c \tag{3.6}$$

The charge density, ρ_c, can be expressed as a sum of the charged particle densities multiplied by elementary charge, e_0, and is calculated as

$$\rho_c = e_0 \sum_k s_k N_k \tag{3.7}$$

where s_k is the charge sign: -1 for electrons, 0 for neutrals and equal to the net charge of negative or positive ions.

Along with multiple levels of ionization, fluid particles may also occupy various levels of excitation, dissociate, or recombine to form species not initially present. As such, the mechanisms considered in this work must be established. Only electron-neutral ionization and electron-ion recombination collisions are considered. For the five species examined in this work, experimental evidence shows that singly-ionized

positive ions are the dominant product of ionization collisions [39–44]. Thus, the modelling consists of three distinct particles types: neutral particles, positive (singly-ionized) ions, and electrons. Equations 3.8-3.9 summarize the general ionization and recombination reactions considered.

$$X + e^- \rightarrow X^+ + 2e^- \tag{3.8}$$

$$X^+ + e^- \rightarrow X \tag{3.9}$$

where X is any given neutral species.

Continuity

The particle densities, N_k [m^{-3}], that fluctuate via the collisions in 3.8-3.9 are governed by the law of continuity. The number of continuity equations required depends on the number of species involved, in which the number density of each unique particle must be conserved. Thus, each unique particle requires a continuity equation in the form of Equation 3.10.

$$\frac{\partial N_k}{\partial t} + \nabla \cdot \mathbf{\Gamma}_k = S_k \tag{3.10}$$

Subscript k represents either electrons (e), ions ($+$) or neutrals (n). For a multi-species fluid of j components, in which only first-order ionization is considered, there will be $2j+1$ continuity equations: j equations conserving all neutrals, j equations conserving all positive ions and an additional equation conserving electrons.

Built into each continuity equation is the convection and diffusion of particles, contained within the total flux term, $\mathbf{\Gamma}_k$ [$\mathrm{m}^{-2}\,\mathrm{s}^{-1}$]. This total flux term, expressed as

$$\boldsymbol{\Gamma}_k = N_k \boldsymbol{U} + s_k \mu_k \boldsymbol{E} N_k - D_k \nabla N_k \tag{3.11}$$

accounts for the bulk flow of particles ($N_k \boldsymbol{U}$), the movement due to electromagnetic forces ($s_k \mu_k \boldsymbol{E} N_k$) and the diffusion term ($D_k \nabla N_k$). While the bulk flow term is included here, the velocity, $\boldsymbol{U}$, is set to zero in quiescent flow. The diffusion term, D_k, is dictated by the Einstein relation for the diffusion of charged particles:

$$D_k = \frac{\mu_k k_B T_k}{q_k} \tag{3.12}$$

where μ_k [$\mathrm{m^2\,V^{-1}\,s^{-1}}$] is the particle mobility, T_k [K] is the particle temperature, and k_B [$\mathrm{J\,K^{-1}}$] and q_k [C] are the Boltzmann constant and electric charge of the particle, respectively. For non-thermal plasma, ions typically have a temperature around 0.01 eV while electrons have a temperature of about 1.0 eV [25, 27, 45]. These values correspond to $T_+ \approx 116\,\mathrm{K}$ and $T_e \approx 11\,605\,\mathrm{K}$. For neutrals, no electromagnetic forces are exerted and all terms in the flux equation 3.11 are zero.

Also included in the continuity equation is the source term, S_k [$\mathrm{m^{-3}\,s^{-1}}$], which governs the rate at which particles are generated or extinguished. The term must be treated differently for each unique particle. The source term for ions, $S_{+,i}$, is expressed as

$$S_{+,i} = \alpha_i \Gamma_e y_i - \beta_i N_e N_{+,i} \tag{3.13}$$

where subscript i indicates the specific gas undergoing ionization. The rate of ionization ($\alpha_i \Gamma_e y_i$) governs the production of ions and consists of Townsend's first ionization coefficient, α_i [$\mathrm{m^{-1}}$], electron flux, Γ_e [$\mathrm{m^{-2}\,s^{-1}}$], and the neutral number density fraction, y_i [unitless]. Townsend's ionization coefficient, α_i, is the number

of ionization events performed by an electron along a unit length path through an electric field. Townsend derived the following equation relating said coefficient to the reduced electric field, E/P [$\mathrm{V\,cm^{-1}Torr^{-1}}$]:

$$\frac{\alpha_i}{P} = A \cdot \exp^{-B/(E/P)} \tag{3.14}$$

where A and B are parameters unique to each species i, listed in Table 3.1. Derived from experimental evidence, α_i only depends on electric field strength and local pressure, and operates under the assumption that all neutrals present are of species i, and thus assumes that all ionization events will involve neutral species i. To generalize the continuity equations for multi-species environments, y_i is introduced to dictate what fraction of ionization events determined by α_i will involve a neutral of species i. The number density fraction is expressed as,

$$y_i = \frac{N_{n,i}}{N_{\text{total}}} \tag{3.15}$$

where N_{total} is the sum of all neutrals and ions:

$$N_{\text{total}} = \sum_{i=1}^{j} N_{n,i} + N_{+,i} \tag{3.16}$$

Lastly, the electron flux, Γ_e, represents the rate at which electrons transfer through a given unit area, as calculated by Equation 3.11. In a physical sense, Γ_e dictates the number of electrons viable to collide with any neutral within a given volume, α_i governs the number of collisions (with sufficient energy to ionize a neutral of species i) each electron will have per unit length, and y_i dictates the fraction of said collisions

that will involve neutral species i.

The rate of recombination ($\beta_i N_e N_{+,i}$) consists of the coefficient of recombination, β_i [$\mathrm{m^3\,s^{-1}}$], and the number density of both electrons, N_e [$\mathrm{m^{-3}}$], and ions, $N_{+,i}$ [$\mathrm{m^{-3}}$]. Unlike ionization, there is no ambiguity as to how many ions and electrons are available to recombine, and there is no need for y_i in determining the rate of recombination. As ionization and recombination collisions proceed, the number density of neutrals for each species i must be conserved by

$$S_{n,i} = -S_{+,i} \tag{3.17}$$

which states that for every ion of species i that is produced via ionization, there must be a neutral of species i removed. Similarly, for every electron-ion recombination, a neutral is produced.

Electron density must also be conserved. The process of first-order ionization produces an additional free electron, while recombination extinguishes a free electron. However, all electrons are alike and only one source term is required:

$$S_e = \sum_{i=1}^{j} S_{+,i} \tag{3.18}$$

The source term for electrons will only be positive if the rate of ionization exceeds the rate of recombination. In the limiting case as N_e approaches zero, the rates of ionization and recombination both tend to zero, as expected, due to the dependence on Γ_e for ionization and N_e for recombination. Similarly, in the limiting case that $N_{+,i}$ goes to zero for any given species i, the rate of recombination will tend to zero due to it's dependence on $N_{+,i}$. Ionization depends on the number density of neutrals

as dictated by y_i and is thus unchanged in the case that $N_{+,i}$ goes to zero. Conversely, as either N_e or $N_{+,i}$ tend toward the upper limit dictated by initial neutral densities, the rate of recombination will increase by virtue of its dependence on both N_e and $N_{+,i}$, while ionization may increase or decrease as Γ_e increases and y_i decreases.

Ionization Parameters

As discussed, α_i is unique to each species. Table 3.1 summarizes the coefficients for each species within the scope of this work, which are then applied to Eq. 3.14. Since this relationship tends toward some limit as E/P increases, these coefficients are typically provided with an associated region of applicability. The coefficients provided in Table 3.1 are reasonable within the range of $E/P < 3000\,\mathrm{V\,cm^{-1}\ Torr^{-1}}$ simulated here.

Table 3.1: Coefficients used to determine α.

Gas	**A** $[\mathrm{cm^{-1}Torr^{-1}}]$	**B** $[\mathrm{V\,cm^{-1}Torr^{-1}}]$	**E/P Range** $[\mathrm{V\,cm^{-1}Torr^{-1}}]$	**Ref.**
N_2	8.8 12	275 342	$E/P \leq 150$ $E/P > 150$	[46]
H_2O	13	290	$E/P > 0$	[46]
CO	4.7	259	$E/P > 0$	[47]
H_2	5.4	139	$E/P > 0$	[46]
CO_2	5.5 20	180 466	$E/P \leq 500$ $E/P > 500$	[46]

Table 3.2 lists the coefficient of recombination, β_i, and ion mobility, μ_+, for each species. As dissociated species are not considered, recombination is assumed to produce the initial neutral. Ion mobility, μ_+, indicates the proportionality between the

Table 3.2: Coefficients of recombination, β_i, and ion mobility, μ_+.

Gas	$\boldsymbol{\beta_i}$ $[\mathrm{m^3\,s^{-1}}]$	**Ref.**
N_2	1×10^{-13}	[30]
H_2O	0.66×10^{-13}	[48]
H_2	2.8×10^{-13}	[49]
CO	6.8×10^{-13}	[50]
CO_2	11.06×10^{-13}	[49]

Gas	$\boldsymbol{\mu_+}$ $[\mathrm{cm^2\,V^{-1}\,s^{-1}}]$	**Ref.**
N_2	$(1.8 \cdot 750)/P[\mathrm{Torr}]$	[30]
H_2O	$(1.181 \cdot 750)/P[\mathrm{Torr}]$	[51]
CO_2	$(1.302 \cdot 750)/P[\mathrm{Torr}]$	[52]
CO	$(1.6 \cdot 750)/P[\mathrm{Torr}]$	[49]
H_2	$(8.73 \cdot 750)/P[\mathrm{Torr}]$	[53]

ion drift velocity and the electric field strength. Similarly, electron mobility, μ_e, indicates the proportionality between electron drift velocity and electric field strength, and is used in Equations 3.11-3.12. Table 3.3 provides the coefficients for Eq. 3.19, by which electron mobility is calculated.

$$\begin{aligned} V_{dr,e}[m/s] &= exp(a \cdot ln(E/N) + b)(1 + exp(-c \cdot ln(E/N) - d) \\ \mu_e &= \frac{V_{dr,e}}{E} \end{aligned} \tag{3.19}$$

Table 3.3: Coefficients used to determine electron drift velocity, $V_{dr,e}$.

Gas	a	b	c	d	Ref.
N_2	0.69813	42.267	0.6634	33.703	[30]
CO_2	0.7429	44.12	0.7358	33.46	[54]
CO	0.8741	49.81	0.6427	40.55	[55]
H_2	0.9852	54.34	0.5852	26.42	[56]
H_2O	0.68001	41.715	0.6855	39.583	[57]

3.2 Dielectric Domain

The solid dielectric region only requires Gauss's Law,

$$\nabla \cdot (\epsilon \nabla \phi_E) = 0 \tag{3.20}$$

which, unlike in the fluid domain, does not depend on volume charge density. However, at the interface between two discrete regions, the difference in electric displacement must be equal to the accumulated surface charge density such that the following equation is satisfied:

$$(\epsilon E_\perp)_{\text{fluid}} - (\epsilon E_\perp)_{\text{diel}} = \sigma_c \tag{3.21}$$

Here, ϵ is the absolute permittivity of each medium (air or dielectric) while $E_\perp$ is the electric field perpendicular to the air-dielectric surface. The surface charge density, σ_c [$\mathrm{C\,m^{-2}}$], results from the accumulation or emission of charges along the dielectric surface. This is computed by the time integral of charged particle fluxes, $\mathbf{\Gamma}_+$ and $\mathbf{\Gamma}_e$ [$\mathrm{m^{-2}\,s^{-1}}$]),

$$\sigma_c = \delta_\sigma e_0 \int (\mathbf{\Gamma}_+ - \mathbf{\Gamma}_e) \cdot \mathbf{n}\, dt \tag{3.22}$$

To differentiate the boundaries, δ_σ is used, and is set to 1 for the dielectric surface and 0 for all other boundaries, as the dielectric surface is the only boundary upon which a surface charge may accumulate. The unit normal vector is denoted by $\mathbf{n}$. As heat transfer effects are not considered, the dielectric region is greatly simplified in that only the electric field needs to be calculated.

Chapter 4

Numerical Methods

This model follows the work of Boeuf and Pitchford [27] and Murzionak et al. [30], and illustrates the generation and propagation of plasma initiated by a constant applied voltage of 1.2 kV at atmospheric pressure and temperature (100 kPa, 300 K). Although DBD actuators require AC voltage to operate, the applied voltage function may vary greatly in shape, magnitude and frequency. Sine, square or triangle AC functions in the 1–50 kV, 0.5–25 kHz range are typical [3], and may include a DC bias. At such frequencies, the constant 1.2 kV applied voltage in this work would model the first 50 ns of a square-wave voltage. The bulk flow is considered quiescent and the movement of plasma is due only to electromagnetic forces acting on the charged particles. The simulations are limited to the dynamics of the plasma and does not explore the influence said plasma has on the surrounding flow field.

4.1 Computational Domain

All models employed by this work are simulated with identical initial conditions within identical geometric domains, though the mesh was adapted as needed for different species. OpenFOAM version 5.x software [58] is used for pre-processing, mesh generation and processing, whereas Paraview version 5.4.x [59] and Matlab version 9.9.x [60] software is employed for post-processing and visualization. The rectangular computational domain is 0.80 mm in length and 0.20 mm in height. The grounded

(embedded) electrode spans the entire length of the bottom surface, covered by a 0.05 mm thick dielectric. The exposed electrode is assumed to be infinitely thin and extends 0.1 mm from the left boundary along the dielectric surface. The fluid region occupies the remaining 0.80 mm x 0.15 mm region above the dielectric, as illustrated in Fig. 4.1.

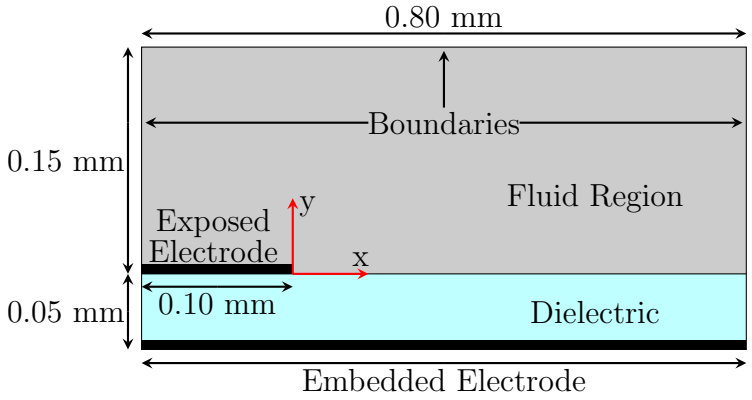

Figure 4.1: Computational domain (not to scale) used in OpenFOAM v5. Origin located at right edge of the exposed electrode.

The domain is separated into two distinct fluid and dielectric regions, with a patched interface between them. The mesh consists of 40,400 uniform 2 µm square cells, which are refined into 1 µm square cells near the dielectric surface, and further refined to 0.5 µm square cells near the exposed electrode. The grid for the N_2 simulation is illustrated in Figure 4.2, though the refined regions shown are extended in the x-direction for simulations in which the plasma travelled a greater distance along the dielectric. This establishes adequate refinement in regions where particle generation and electric field gradients are highest, and ensures that regions of high ion-density do not extend into coarse mesh. Upon imposing the relevant boundary conditions and initial values, fluid and solid characteristics are applied to the respective regions.

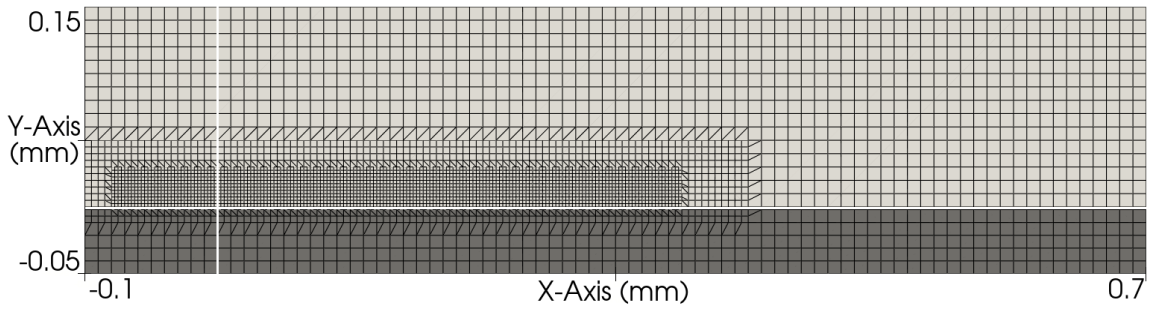

Figure 4.2: Example of grid refinement for N_2, with the origin located at the right edge of the exposed electrode. The number of cells is reduced by a factor of 25 in order to resolve the cell shapes and regions of refinement.

4.2 Discretization Schemes

Along with the spatial discretization of the computational domain through mesh generation, the governing equations must also be discretized. To illustrate the Finite Volume Method (FVM), the general transport equation for the flow variable ϕ is expressed as:

$$\underbrace{\frac{\partial \rho\phi}{\partial t}}_{\text{Transient}} + \underbrace{\nabla \cdot (\rho \boldsymbol{u}\phi)}_{\text{Convection}} - \underbrace{\nabla \cdot (\rho\Gamma\nabla\phi)}_{\text{Diffusion}} = \underbrace{S_\phi}_{\text{Source}} \tag{4.1}$$

By integrating these terms over a control volume, V_p, the following is derived:

$$\int_{V_p} \frac{\partial \rho\phi}{\partial t} dV + \int_{V_p} \nabla \cdot (\rho \boldsymbol{u}\phi) dV - \int_{V_p} \nabla \cdot (\rho\Gamma\nabla\phi) dV = \int_{V_p} S_\phi dV \tag{4.2}$$

FVM is aimed at solving the different terms in Equation 4.2, and Table 4.1 lists the various methods employed in this work.

Table 4.1: Discretization and interpolation schemes applied to the governing equations.

Term	General Expression	Scheme	Order	Interpolation Scheme
Time	$\frac{\partial}{\partial t}$	Euler	$O(h)$	-
Gradient	$\nabla\phi$	Gauss	$O(h^2)$	Linear
Divergence	$\nabla \cdot (\rho \boldsymbol{u}\phi)$	Gauss	$O(h^2)$	Van Leer
Laplacian	$\nabla \cdot (\Gamma \nabla\phi)$	Gauss	$O(h^2)$	Linear Corrected

All spatial terms make use of the Gauss (or Divergence) theorem, a fundamental component of FVM, which allows volume integrals to be converted into surface integrals. In general, the theorem takes the form:

$$\int_V \nabla \cdot \boldsymbol{F} dV = \oint_S \boldsymbol{F} \cdot \boldsymbol{n} dS \tag{4.3}$$

Divergence theorem states that the for a control volume V bounded by a surface S, the net flux of a vector field $\boldsymbol{F}$ through the surface S is equal to the divergence of $\boldsymbol{F}$ within the surface S. Physically, the net flow through the boundary of V is equal to the sum of sources and sinks contained within V. Applying Divergence theorem to Equation 4.2 provides the following:

$$\int_{V_p} \frac{\partial \rho\phi}{\partial t} dV + \oint_S (\rho \boldsymbol{u}\phi) \cdot \boldsymbol{n} dS - \oint_S (\rho\Gamma\nabla\phi) \cdot \boldsymbol{n} dS = \int_{V_p} S_\phi dV \tag{4.4}$$

These surface integrals are converted to finite sums, where f represents the discrete

faces that make up the surface S:

$$\int_{V_p} \frac{\partial \rho\phi}{\partial t} dV + \sum_f \boldsymbol{S}_f \cdot (\rho \boldsymbol{u}\phi)_f - \sum_f \boldsymbol{S}_f \cdot (\rho\Gamma\nabla\phi)_f = \int_{V_p} S_\phi dV \tag{4.5}$$

As such, Equation 4.2 calls for values at the cell faces rather than the cell centers, which requires the interpolation schemes listed in Table 4.1.

Temporal Discretization

The simulations also require temporal discretization. Modelling DBD plasma has difficulties in numerical analysis as a result of the variation in time scales. Ionization and recombination reactions occur on the order of nanoseconds or smaller, whereas the operation of a plasma actuator is on the order of microseconds to milliseconds. Thus, the presence of plasma modelling is prohibitive in that it requires sufficiently small time-steps while keeping computational run-time within reason.

For this work, the Euler implicit time scheme listed in Table 4.1 is used. An adaptive time scheme determines time-steps in the range of 10^{-20} to 5×10^{-14} s, which are adjusted based on several different Courant/control numbers. These control numbers limit excessive generation of charged particles and spatial movement of the plasma in a given time-step.

The movement of electrons is limited by C_e

$$\mathrm{C}_e = \frac{1}{2} \cdot \max\Big[\frac{\sum \Gamma_e}{N_e \cdot V}\Big] \cdot \Delta t \tag{4.6}$$

where $\sum \Gamma_e$ is the magnitude of flux through all surfaces, in or out, of a given cell, N_e is the number of electrons contained in the cell and V is the volume of the cell. The

global maximum from all cells is taken to determine C_e. Similarly, the movement of ions is defined as:

$$C_+ = \frac{1}{2} \cdot \max\left[\frac{\sum \Gamma_+}{N_+ \cdot V}\right] \cdot \Delta t \tag{4.7}$$

Additionally, to limit the rate at which electrons and ions are generated, C_{gen} is defined:

$$C_{gen} = \frac{1}{2} \cdot \max\left[\frac{\sum S_e}{N_n}\right] \cdot \Delta t \tag{4.8}$$

where S_e is the source term for electrons and N_n is the number of neutrals within the cell.

These control numbers are then compared to the user defined maximums, by which the minimum is taken to adjust the time-step Δt. The time-step as calculated by these control numbers is only applied if it does not exceed the user defined maximum Δt, set to 5×10^{-14} s for all simulations. Additionally, decreases to the time-step as imposed by the control numbers are applied immediately to ensure their conditions are met, after which Δt may only be incremented by a factor of 1.1–1.3. Limiting the rate at which Δt is increased prevents time-step oscillations which may otherwise cause numerical instability.

4.3 Matrix Systems and Pre-conditioners

Given the electrodynamic theory discussed in Section 3.1, solutions for the electric potential and charge densities are reliant on FVM to evaluate the partial differential equations (PDEs). OpenFOAM's Diagonal Incomplete Cholesky Preconditioned Conjugate Gradient (DICPCG) solver is used to solve for electric potential in the fluid

and solid regions. A Diagonal Incomplete LU Preconditioned Bi-Conjugate Gradient (DILUPBiCG) solver is then employed to solve for all charge densities in the fluid region. Once the domain is discretized in space by the computational mesh and Equations 3.6 and 3.10 are discretized, a system of algebraic equations is constructed,

$$\mathbf{A}\mathbf{x} = \mathbf{b} \tag{4.9}$$

the solution to which provides the unknown value in each cell of the computational mesh. $\mathbf{A}$ is a coefficient matrix, $\mathbf{b}$ is the source vector of known values, and $\mathbf{x}$ represents the solution vector or the vector of unknowns (e.g. ϕ_E and N_k). The system takes on the form

$$\begin{bmatrix} a_{11} & a_{12} & \dots & a_{1n} \\ a_{21} & a_{22} & \dots & a_{2n} \\ \vdots & \vdots & \ddots & \vdots \\ a_{n1} & a_{n2} & \dots & a_{nn} \end{bmatrix} \begin{bmatrix} x_1 \\ x_2 \\ \vdots \\ x_n \end{bmatrix} = \begin{bmatrix} b_1 \\ b_2 \\ \vdots \\ b_n \end{bmatrix} \tag{4.10}$$

where n refers to the number of cells in the mesh, thus creating n equations for n unknowns in vector $\mathbf{x}$. The coefficient matrix $\mathbf{A}$ is sparse and square, generated by OpenFOAM based on geometrical quantities and the discretized governing equations [61]. Every cell has a diagonal coefficient, i.e. for $1 \leq i \leq n$,

$$a_{ii} \neq 0 \tag{4.11}$$

and these diagonal elements correspond to properties within cell i. All off-diagonal elements correspond to cell-pairs that influence one another. Given a simple 3 x 3

mesh of 9 cells and 12 internal faces, shown in Figure 4.3, a square coefficient matrix **A** of 9 rows and columns will be arranged, with 9 non-zero diagonal and 24 non-zero off-diagonal coefficients, as shown in Figure 4.4.

1	2	3
6	5	4
7	8	9

Figure 4.3: Arbitrary 9-cell mesh.

$_i\backslash^j$	1	2	3	4	5	6	7	8	9	**x**		**b**
1	a_{11}	a_{12}				a_{16}				x_1		b_1
2	a_{21}	a_{22}	a_{23}		a_{25}					x_2		b_2
3		a_{32}	a_{33}	a_{34}						x_3		b_3
4			a_{43}	a_{44}	a_{45}				a_{49}	x_4	=	b_4
5		a_{52}		a_{54}	a_{55}	a_{56}		a_{58}		x_5		b_5
6	a_{61}				a_{65}	a_{66}	a_{67}			x_6		b_6
7						a_{76}	a_{77}	a_{78}		x_7		b_7
8					a_{85}		a_{87}	a_{88}	a_{89}	x_8		b_8
9				a_{94}				a_{98}	a_{99}	x_9		b_9

Figure 4.4: Simple 9-cell mesh and associated matrix equation.

The blank coefficients are zero-valued as they correspond to cells i and j which do influence each other. In populating the matrix with appropriate coefficients, the two off-diagonal coefficients for a given internal face must be distinguished. For each of these faces, OpenFOAM assigns an owner cell and a neighbour cell, such that a positive surface-normal vector is defined which points away from the owner cell to the neighbour cell. This distinction becomes necessary when the mathematical operations involved are sign dependent, such as instances when fluxes are involved.

Owner, diagonal and neighbour coefficients are defined as:

$$a_{i,j} = \begin{cases} \text{owner}, & i > j \\ \text{diagonal}, & i = j \\ \text{neighbour}, & i < j \end{cases} \tag{4.12}$$

Following this notation, owner and neighbour coefficients populate the lower and upper triangles of the matrix, respectively. With the system of equations determined, the solver begins an iterative method of solving for vector $\mathbf{x}$. In general, $\mathbf{x}_0$ is assumed for the solution vector, often by using the solution from the previous time-step, and applied to

$$\mathbf{x}_{k+1} = \mathbf{A}\mathbf{x}_k \tag{4.13}$$

for $k = 0 \rightarrow k_{\max}$, where $k_{\max}$ is a user-defined maximum number of iterations. With every iteration, the resulting x_{k+1} solution vector provides a residual vector:

$$\mathbf{r}_{k+1} = ||\mathbf{A}\mathbf{x}_{k+1} - \mathbf{b}|| \tag{4.14}$$

This iterative process is terminated when either the maximum number of iterations is reached (k=$k_{\max}$), or when the residual drops below a user-defined tolerance. This method is employed to solve for all unknown values for each time-step. The algorithm used to solve for $\mathbf{x}_{k+1}$ varies and will be discussed further.

Computational efficiency can be improved by accelerating the solution process through the use of pre-conditioners. Pre-conditioners are algorithms meant to modify Equation 4.9 in an effort to increase the speed of convergence. Preconditioning

involves finding a matrix such that:

$$\mathbf{M}^{-1}\mathbf{A}\mathbf{x} = \mathbf{M}^{-1}\mathbf{b} \tag{4.15}$$

while ensuring $\mathbf{M}$ is easily inverted. The two preconditioning methods employed are Diagonal Incomplete LU (DILU) and Diagonal Incomplete Cholesky (DIC) preconditioners. DLU (diagonal lower-upper) decomposition or factorization turns the coefficient matrix $\mathbf{A}$ into two factors, a lower (L) and upper (U) triangular matrix. For example, if $\mathbf{A}$ is defined as:

$$\mathbf{A} = \begin{bmatrix} 1 & 2 & 4 \\ 3 & 8 & 14 \\ 2 & 6 & 13 \end{bmatrix} \tag{4.16}$$

then $\mathbf{A}$ is factored into $\mathbf{LU}$

$$\mathbf{A} = \mathbf{LU} \tag{4.17}$$

$$\begin{bmatrix} 1 & 2 & 4 \\ 3 & 8 & 14 \\ 2 & 6 & 13 \end{bmatrix} = \begin{bmatrix} 1 & 0 & 0 \\ 3 & 1 & 0 \\ 2 & 1 & 1 \end{bmatrix} \begin{bmatrix} 1 & 2 & 4 \\ 0 & 2 & 2 \\ 0 & 0 & 3 \end{bmatrix} \tag{4.18}$$

DILU factorization instead finds triangular matrices such that $\mathbf{A} \approx \mathbf{LU}$,

$$\mathbf{A} = \mathbf{LU} - \mathbf{R} \tag{4.19}$$

where the elements of $\mathbf{R}$ are ignored depending on thresholds and the sparsity pattern

of **A**. The triangular matrices **L** and **U** are then used as the pre-conditioner $\mathbf{M} = \mathbf{LU}$ to accelerate the solution process.

Diagonal Cholesky (DC) factorization uses only the lower triangular matrix and its conjugate transpose to express **A**, where **A** is a symmetric matrix. For the matrix **A**:

$$\mathbf{A} = \begin{bmatrix} 4 & 12 & -16 \\ 12 & 37 & -43 \\ -16 & -43 & 98 \end{bmatrix} \tag{4.20}$$

A is factored in **L** and $\mathbf{L}^*$:

$$\mathbf{A} = \mathbf{L}\mathbf{L}^* \tag{4.21}$$

$$\mathbf{L}\mathbf{L}^* = \begin{bmatrix} 2 & 0 & 0 \\ 6 & 1 & 0 \\ -8 & 5 & 3 \end{bmatrix} \begin{bmatrix} 2 & 6 & -8 \\ 0 & 1 & 5 \\ 0 & 0 & 3 \end{bmatrix} \tag{4.22}$$

Similarly, DIC factorization finds the lower matrix **L** such that $\mathbf{A} \approx \mathbf{L}\mathbf{L}^*$, and is then used as the pre-conditioner for the iteration process.

The iteration processes employed are conjugate gradient (CG) and bi-conjugate gradient (BiCG) methods, both of which are similar algorithms for solving Equation 4.9. The coefficient matrix in solving for ϕ_E is diagonal, and as such DIC preconditioning can be applied to the CG method. The coefficient matrices in solving for charge densities are asymmetric, and instead the DILU pre-conditioner is used with

the BiCG method. In the case of fluid-mixture simulations, similar conservation equations for the neutral particle densities must be included, however Equation 3.10, when applied to neutrals, lacks the flux term, $\mathbf{\Gamma}$, needed for charged particle densities. As such, the coefficient matrix $\mathbf{A}$ is a square diagonal, and all non-diagonal elements are zero. Thus, the system of equations for neutrals is explicit, and does not require the same iterative method as the charged particle densities.

4.4 Initial and Boundary Conditions

Charge densities and fluxes at the exposed electrode and dielectric surface boundaries are governed by Equations 4.23–4.26, while Figures 4.5 and 4.6 illustrate said equations in physical terms. Though the exposed electrode is constant at 1200 V, the direction of the electric field will change spatially within the domain. Electric field lines always point away from the exposed electrode and into the dielectric surface, toward the grounded electrode. Thus, $E_\perp > 0$ corresponds to the exposed electrode boundary, while $E_\perp < 0$ corresponds to the dielectric surface boundary.

$$\mathbf{\Gamma}_e = \begin{cases} -\mu_e \boldsymbol{E} N_e & if \quad E_\perp > 0 \\ -\gamma \mathbf{\Gamma}_+ & if \quad E_\perp < 0 \end{cases} \tag{4.23}$$

$$\mathbf{\Gamma}_+ = \begin{cases} 0 & if \quad E_\perp > 0 \\ \mu_+ \boldsymbol{E} N_+ & if \quad E_\perp < 0 \end{cases} \tag{4.24}$$

$$N_e = \begin{cases} \nabla(N_e) = 0 & if \quad E_\perp > 0 \\ \gamma N_+ \frac{\mu_+}{\mu_e} & if \quad E_\perp < 0 \end{cases} \tag{4.25}$$

$$N_+ = \begin{cases} 0 & if \quad E_\perp > 0 \\ \nabla(N_+) = 0 & if \quad E_\perp < 0 \end{cases} \tag{4.26}$$

Equations 4.23 and 4.24 govern flux into, or out of, the boundary. Flux is defined as positive when charges are emitted out from the surface, and negative when directed into the surface. At the electrode surface, show in Figure 4.5, where the perpendicular electric field is positive, electrons are drawn toward the electrode with a particle flux of $\mathbf{\Gamma}_e = -\mu_e \boldsymbol{E} N_e$ [$\mathrm{m^{-2}\,s^{-1}}$]. The bombardment of electrons into the electrode does not induce the emission of ions, thus $\mathbf{\Gamma}_+ = 0$ [$\mathrm{m^{-2}\,s^{-1}}$].

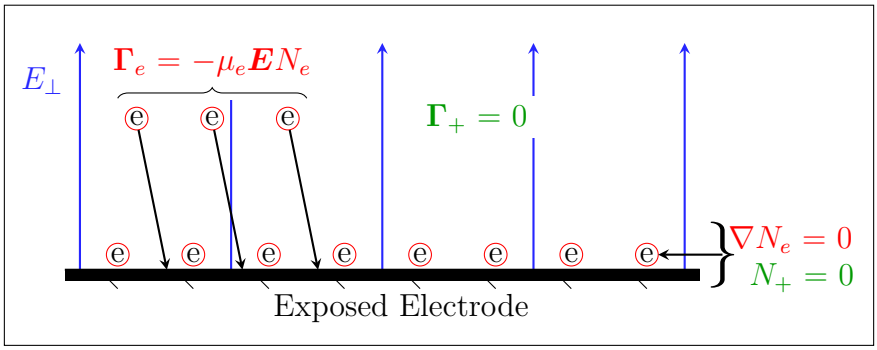

Figure 4.5: Flux of charged particles and number density at the exposed electrode.

At the dielectric surface, shown in Figure 4.6, the perpendicular electric field is negative,and ions are drawn toward the electrode at $\mathbf{\Gamma}_+ = \mu_+ \boldsymbol{E} N_+$ [$\mathrm{m^{-2}\,s^{-1}}$]. However, this bombardment of ions into the dielectric induces the emission of electrons at a rate governed by the emissivity of the dielectric, such that $\mathbf{\Gamma}_e = -\gamma \mathbf{\Gamma}_+$ [$\mathrm{m^{-2}\,s^{-1}}$].

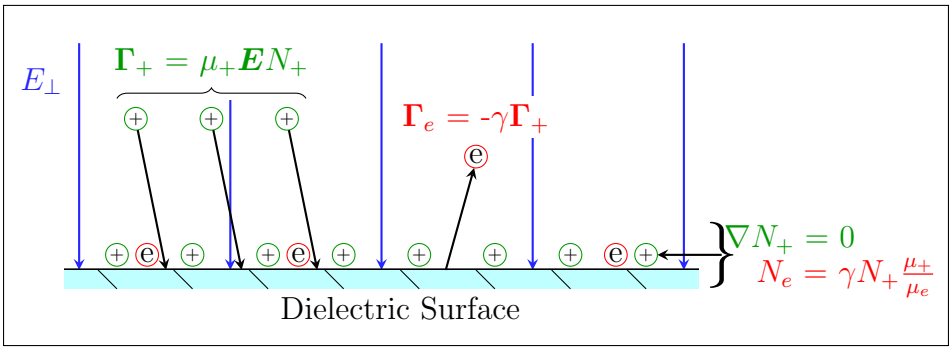

Figure 4.6: Flux of charged particles and number density at the dielectric surface.

Equations 4.25 and 4.26 govern the charge densities at these surfaces. At the exposed electrode, electron density is dictated by the zero-gradient condition: $\nabla N_e = 0$. Because no ions are emitted from the electrode, and any ions in the region would be accelerated away from the electrode, ion density at the electrode surface is zero: $N_+ = 0$ [m^{-3}].

At the dielectric surface, ion density is governed by a zero-gradient condition: $\nabla N_+ = 0$. However, due to the emission of electrons from the dielectric, the density of electrons at the surface will be non-zero and in higher concentration where ion flux is larger. The electron density depends on the emissivity of the dielectric, the density of ions on the surface, and the mobility of ions relative to the mobility of electrons: $N_e = \gamma N_+ \frac{\mu_+}{\mu_e}$ [m^{-3}]. In this form, the expression has little physical meaning, but it can be shown to reduce to $N_e = |\boldsymbol{\Gamma}_e|/V_{dr,e}$ i.e. the electron density at the surface is directly proportional to the magnitude of electron flux and inversely proportional to the local drift velocity of electrons.

Table 4.2 provides the initial and boundary conditions for each case, while the thermophysical properties of all fluids and the dielectric are shown in Table 4.3.

Table 4.2: Initial conditions for fluid and dielectric region, denoted with subscript i, and boundary conditions

Location	Parameter	Value
Fluid Region	ϵ_r	1
	T_i	300 K (375 K for H_2O)
	P_i	100 kPa
	N_{e_i}	1e13 m^{-3}
	N_{+_i}	1e13 m^{-3}
	ϕ_{E_i}	0 V
Dielectric Region	ϵ_r	10
	ϕ_{E_i}	0V
Exposed Electrode	ϕ_E	1200 V
	N_e, N_+	Calculated (Eq. 4.23, 4.24)
	$\mathbf{\Gamma}_e, \mathbf{\Gamma}_+$	Calculated (Eq. 4.25. 4.26)
	δ_σ	0
Interface–Fluid Region	N_e, N_+	Calculated (Eq. 4.23, 4.24)
	$\mathbf{\Gamma}_e, \mathbf{\Gamma}_+$	Calculated (Eq. 4.25, 4.26)
	δ_σ	1
Outer Boundaries	ϕ_E, N_e, N_+	Zero Gradient
	$\mathbf{\Gamma}_e, \mathbf{\Gamma}_+$	Calculated
	δ_σ	0
Dielectric Walls	ϕ_E	Zero Gradient
Embedded Electrode	ϕ_E	0 V

Table 4.3: Thermophysical properties of all gases and the dielectric.

Gas	Molar Weight (g/mol)	C_p (J/kg·K)	μ_v (Pa·s)	Pr
N_2	28.90	1000	$1.8{\cdot}10^{-5}$	0.72
CO_2	44.01	849	$1.5{\cdot}10^{-5}$	0.76
CO	28.01	1046	$1.78{\cdot}10^{-5}$	0.74
H_2	2.02	14310	$8.89{\cdot}10^{-6}$	0.70
H_2O	18.02	1890	$2.76{\cdot}10^{-4}$	1.03

Dielectric	Molar Weight (g/mol)	C_p (J/kg·K)	ρ (kg/m^3)
	50	450	8000
	k (W/m·K)	absorptivity	emissivity γ
	80	0	0.05

Chapter 5

Grid Sensitivity Analysis

With any CFD simulation, spatial discretization will introduce some degree of error to the numerical solutions. As such, it is important to evaluate the extent by which these errors influence the accuracy of the reported results. The approach used is that presented by Roache [62], which introduces a Grid Convergence Index (GCI) to quantify the error introduced by the spatial discretization of the grid.

5.1 GCI Theory

Order of Convergence

Each grid solution is dependent on the resolution of the grid itself, which will differ from the exact solution that would be obtained on a grid with zero spacing. The difference between the two solutions can be expressed as:

$$e = f(h) - f_0 = Ch^p + H.O.T \tag{5.1}$$

in which $f(h)$ is the numerical solution obtained from a grid with spacing h, and f_0 is the true solution for zero grid spacing. C is a constant, and p is the observed order of convergence. The error, e, is then the difference between the numerical result and the zero-spacing solution. If the grids are assumed to be sufficiently refined, such that the

results fall within the asymptotic region, i.e. the results do not change significantly with each grid refinement, the higher order terms ($H.O.T$) can be neglected. This leaves three unknowns, f_0, C and p. By using three grids, Equation 5.1 can be expressed three times and solved for p. For three analytical solutions,

$$\begin{aligned} e_1 &= f_1 - f_0 = Ch_1^p \\ e_2 &= f_2 - f_0 = Ch_2^p \\ e_3 &= f_3 - f_0 = Ch_3^p \end{aligned} \tag{5.2}$$

both f_0 and C can be eliminated:

$$\frac{e_3 - e_2}{e_2 - e_1} = \frac{Ch_3^p - Ch_2^p}{Ch_2^p - Ch_1^p} \quad \rightarrow \quad \frac{f_3 - f_2}{f_2 - f_1} = \frac{h_3^p - h_2^p}{h_2^p - h_1^p} \tag{5.3}$$

The grid spacing values, h_i, and the difference between numerical solutions can be replaced by the following:

$$\begin{aligned} r_{21} &= \frac{h_2}{h_1} & r_{32} &= \frac{h_3}{h_2} \\ \varepsilon_{21} &= f_2 - f_1 & \varepsilon_{32} &= f_3 - f_2 \end{aligned} \tag{5.4}$$

$$\frac{\varepsilon_{32}}{\varepsilon_{21}} = \frac{r_{21}^p(r_{32}^p - 1)}{(r_{21}^p - 1)} \quad \rightarrow \quad r_{21}^p = \frac{\varepsilon_{32}(r_{21}^p - 1)}{\varepsilon_{21}(r_{32}^p - 1)} \tag{5.5}$$

The observed order of convergence, p, can then be expressed as,

$$p = \ln\left[\frac{\varepsilon_{32}(r_{21}^p - 1)}{\varepsilon_{21}(r_{32}^p - 1)}\right] \Big/ \ln[r_{21}] \tag{5.6}$$

Generally, Equation 5.6 needs to be solved iteratively. However, in the case where the grid is refined uniformly each time, i.e. $r_{32} = r_{21} = r$, Equation 5.6 reduces to:

$$p = \ln\Big[\frac{(f_3 - f_2)}{(f_2 - f_1)}\Big]\Big/\ln[r] \tag{5.7}$$

Typical grid convergence analysis uses a constant ratio of $r = 2$, in which each refinement doubles the number of grid points in each direction. For 2-D simulations, this would result in doubling the grid points in the x and y directions, increasing the total number of cells by a factor of 4. However, it can be computationally prohibitive to refine the grid by a constant ratio, nor is it required that the ratio be an integer value. It has been found that grid refinement ratios be greater than 1.3 for adequate grid refinement analysis [63].

Error estimation

With the order of convergence, p, determined, one can estimate the exact value at zero grid spacing ($h = 0$). Richardson extrapolation is used for this estimate. The computed result of any quantity f can be expressed as,

$$f = f_0 + g_1 h + g_2 h^2 + g_3 h^3 + ... \tag{5.8}$$

in which the functions g are independent of grid spacing. The solution f is considered second-order if $g_1 = 0$. By assuming a second-order solution for two grids, f_1 and f_2,

and neglecting higher order terms, two equations in the form of 5.8 are derived,

$$\begin{aligned} f_1 &\approx f_0 + g_2 h_1^2 \\ f_2 &\approx f_0 + g_2 h_2^2 \end{aligned} \tag{5.9}$$

which can be used to approximate the zero spacing solution f_0.

$$f_0 \approx \ f_1 + \frac{f_1 - f_2}{r_{21}^2 - 1} \tag{5.10}$$

This can be generalized for a p^{th} order solution and rearranged into two equivalent expressions,

$$f_0 \approx \ f_1 + \frac{f_1 - f_2}{r_{21}^p - 1} \tag{5.11a}$$

$$f_0 \approx \ f_2 + \frac{(f_1 - f_2) r_{21}^p}{r_{21}^p - 1} \tag{5.11b}$$

In the approximations of Equation 5.11, the second term is an error estimator for either f_1 or f_2. Equation 5.11a can be manipulated to represent this term as a fractional error estimator, E:

$$E_1 = \frac{f_1 - f_0}{f_1} = \frac{1}{f_1} \frac{f_2 - f_1}{r_{21}^p - 1} \tag{5.12}$$

Including the notation from 5.4, the fractional error estimators for grids 1 and 2 reduce to

$$E_1 = \frac{\varepsilon_{21}}{f_1(r_{21}^p - 1)} \tag{5.13a}$$

$$E_2 = \frac{\varepsilon_{21} r_{21}^p}{f_1(r_{21}^p - 1)} \tag{5.13b}$$

The estimated fractional errors of E_1 and E_2 are an improvement of the relative error ε_{21}, as E_1 and E_2 consider both r and p. Using relative error alone, one could make ε_{21} artificially small by selecting r very close to 1, thus E is recommended.

Grid Convergence Index

Often, CFD simulations involve simulations in which the exact solution is unknown. In such cases, the Grid Convergence Index (GCI) can be used to measure the percentage the computed value is from the asymptotic numerical solution. For the finest grid, the GCI is defined as,

$$GCI_{\text{fine}} = F_s |E_1| \tag{5.14}$$

where F_s is a safety factor. In the event that a large number of simulations are required and a coarser grid is desired for computational economy, the GCI can be calculated for the medium grid as,

$$GCI_{\text{medium}} = F_s |E_2| \tag{5.15}$$

Though E_1 and E_2 only depend on the numerical results of f_1 and f_2, the coarse grid solution f_3 is needed to accurately estimate the order of convergence, p. Therefore,

the recommended safety factor is $F_s = 3.0$ for a two grid comparison, and $F_s = 1.25$ for a three (or more) grid comparison. The GCI values can be considered a representation of the bound on the estimated error, in which the converged numerical solution is expected to fall within.

5.2 Grid Convergence Results

The dependence of the simulations on the grid size is tested for three levels of refinement: coarse, medium and fine. For all three tests, the grid is uniformly spaced, then refined along the dielectric surface and near the exposed electrode, as shown in Figure 4.2. These tests model ionization in pure N_2. In anticipation of running large numbers of simulations within the scope of this work, the medium grid was first designed to be as fine as possible without incurring unreasonable computational cost in future use. The grid was then coarsened as much as possible while maintaining numerical stability to generate grid 3, while the fine mesh was chosen in consideration of a computational threshold. The resulting refinement ratios were non-uniform, i.e. $r_{32} \neq r_{21}$, and Equation 5.6 was used. The grid features can be found in Table 5.1, with simulations handled by 4 cores of an Intel® Xeon® E5-2687W 3.10 GHz CPU.

Table 5.1: Mesh features and computational cost.

Grid	**Grid Spacing (h)**	**Number of Cells**	**Computational Time [hr]**
Coarse (3)	1.4	55 506	14.37
Medium (2)	1	105 070	29.46
Fine (1)	0.625	269 392	79.04

Pertinent results for the simulations, and thus for grid sensitivity analysis, include ion density, N_+ [m^{-3}], current density [$\mathrm{A\,m}^{-1}$], the extent of plasma propagation [m], and surface charge density along the dielectric surface [$\mathrm{C\,m}^{-2}$]. Due to the transient nature of the simulations, the results for each grid are expected to change both in time and space, thus care must be taken when choosing how to compare results. Ion density, for example, is not expected to peak at the same time or location on each grid. A global maximum for N_+ over then entire 50 ns period is then used to assess the accuracy of each grid.

Figure 5.1 shows the maximum ion density for each grid over 50 ns, irrespective of where in space the maximum resides. For each grid, ion density peaks around 8 ns, after which the fluctuations stabilize. Figure 5.2 plots the magnitude of each peak along with the estimated convergence value expected on a zero-spacing grid. The non-zero grid spacing results in an overestimation of peak ion density, though

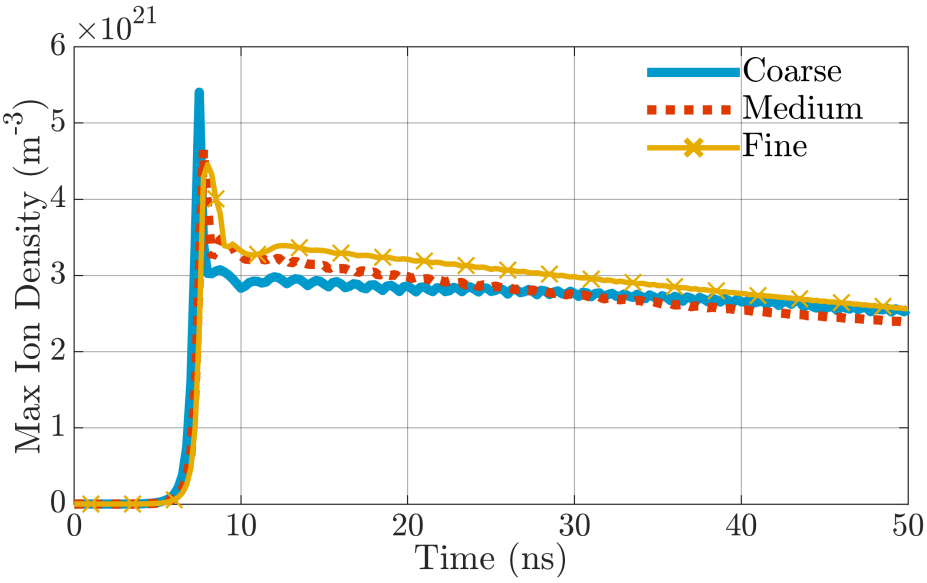

Figure 5.1: Peak ion density over 50 ns.

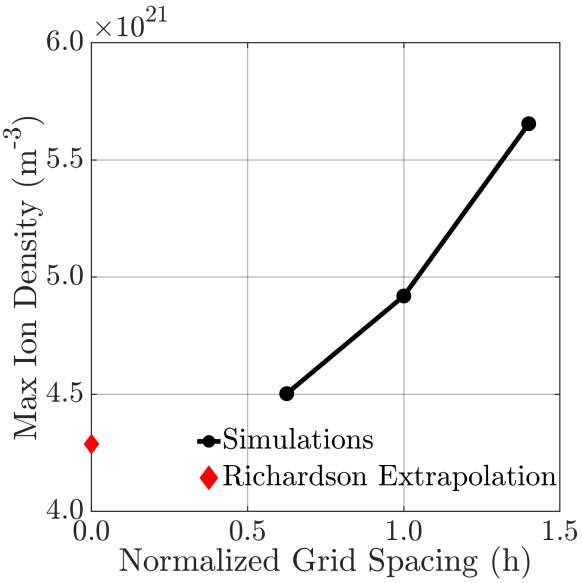

Grid (h)	Max Ion Density [m^{-3}]
Coarse (1.4)	5.6544×10^{21}
Medium (1)	4.9194×10^{21}
Fine (0.625)	4.5026×10^{21}
Estimated Convergence	4.2876×10^{21}

Grid Convergence Index	
p	2.2934
GCI_{medium}	17.54%
GCI_{fine}	5.97%

Figure 5.2: GCI analysis for maximum ion density.

each successive refinement is shown to approach the $4.2876 \times 10^{21}\,m^{-3}$ asymptote. Additionally, after 10 ns, the medium and fine mesh exhibit similar rates of decay in ion density, whereas the coarse mesh produces oscillatory behaviour and a lessened rate of decay. However, the GCI values for the medium and fine grids, 17.54% and 5.97% respectively, are relatively high and ion density appears to be sensitive to grid refinement. This is likely a symptom of electron-avalanche, in which the charge density increases exponentially. It is also expected that applying GCI analysis to maximum values, as opposed to averages, will result in a larger interval of error estimation.

The current density along the exposed electrode is directly impacted by the flux of ions and electrons in the region, and thus closely related to the rate of ionization. Figure 5.3 shows the current density for each grid with peak values around 8 ns, mirroring the peaks in Figure 5.1. Figure 5.4 plots the peak for each grid, all of

which overestimate the estimated convergence value, with the medium grid GCI of 10.60%.

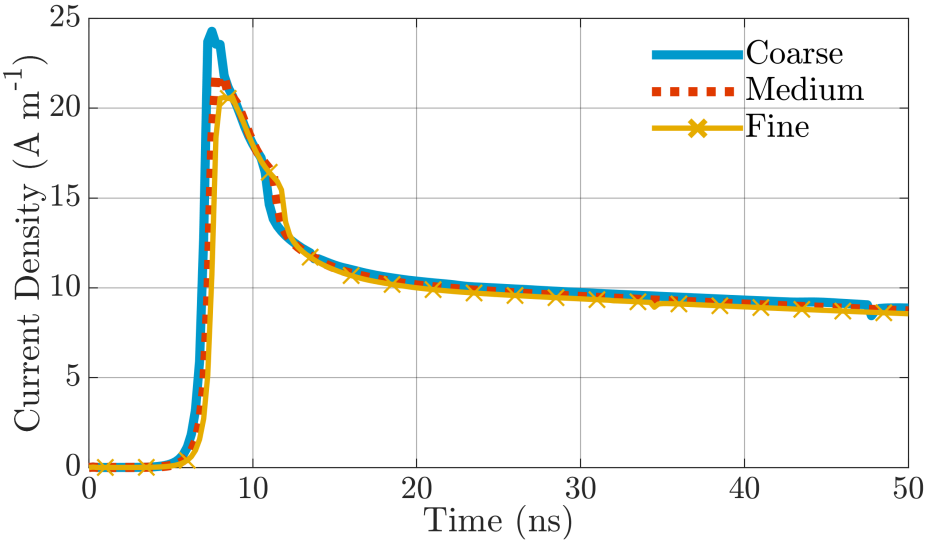

Figure 5.3: Current density through the exposed electrode over 50 ns.

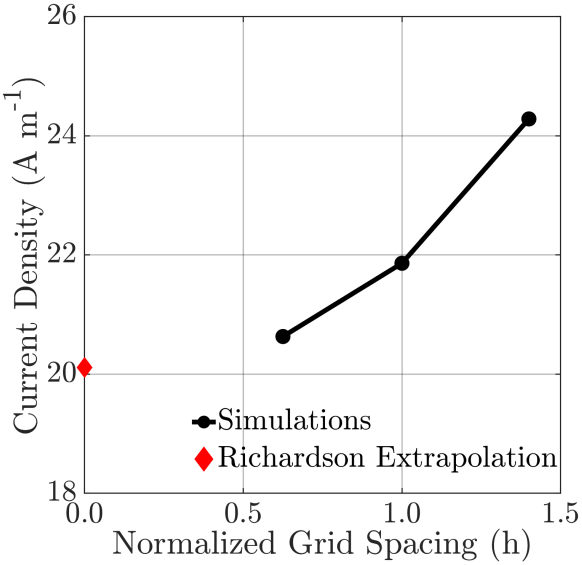

Grid (h)	**Max Current Density [Am^{-1}]**
Coarse (1.4)	24.2828
Medium (1)	21.8606
Fine (0.625)	20.6309
Estimated Convergence	20.1114

Grid Convergence Index	
p	2.5829
GCI_{medium}	10.60%
GCI_{fine}	3.15%

Figure 5.4: GCI analysis for maximum current density along the exposed electrode.

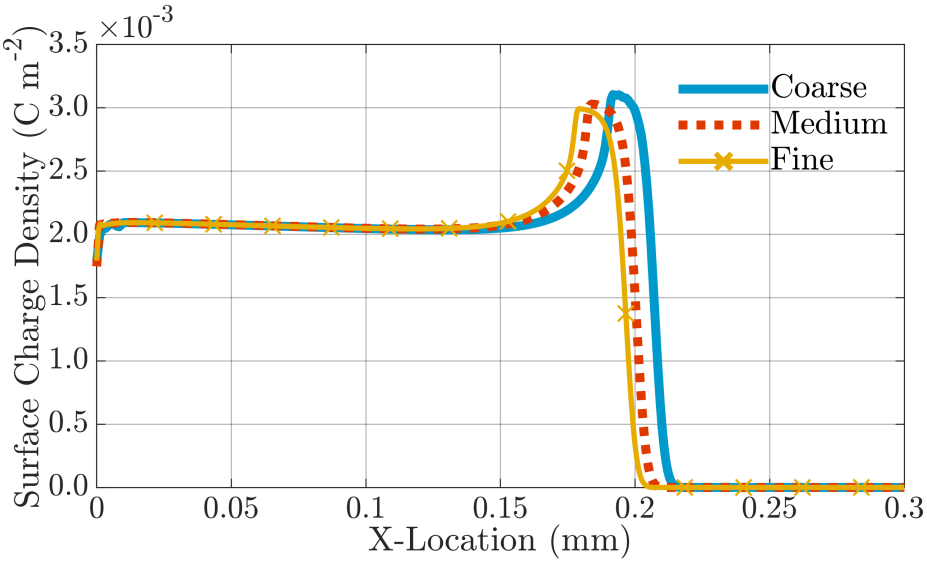

Figure 5.5: Surface charge distribution along dielectric at 50 ns.

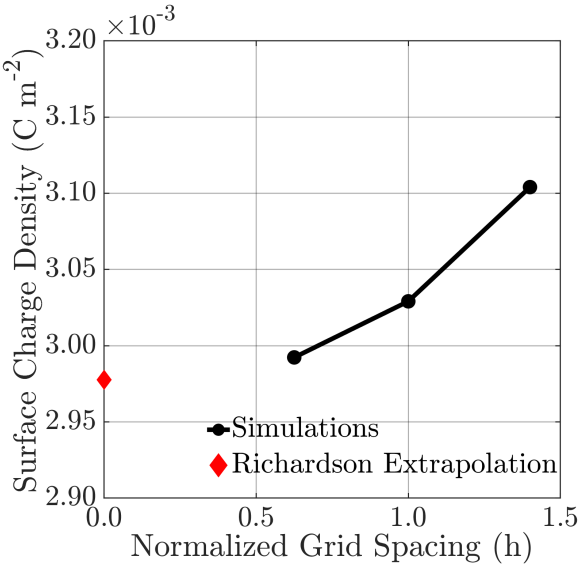

Grid (h)	Max Surface Charge [Cm^{-2}]
Coarse (1.4)	3.1040×10^{-3}
Medium (1)	3.0291×10^{-3}
Fine (0.625)	2.9923×10^{-3}
Estimated Convergence	2.9776×10^{-3}

Grid Convergence Index	
p	2.2670
GCI_{medium}	2.15%
GCI_{fine}	0.61%

Figure 5.6: GCI analysis for maximum surface charge density along the dielectric surface at 50 ns.

Surface charge density has a similar relationship to ion density, as increased ionization will increase the rate at which ions are deposited on the dielectric surface. The

surface charge along the dielectric surface at 50 ns is shown in Figure 5.5, in which the peak for each grid coincides with the region of greatest ionization at the front of the plasma. However, by 50 ns, the previously mentioned spike has passed, and ion densities have stabilized at this point, leading to far better GCI values of less than 3.0% for both the medium and fine grids.

Ion density is used to determine the propagation of the plasma as it evolves, in which the location of maximum ion density is tracked over the 50 ns period. Figure 5.7 illustrates the movement of the plasma on each grid, all of which are linear after 10 ns. Figure 5.8 plots the maximum streamwise location of the plasma head reached at 50 ns, estimated to be 1.9357×10^{-4} m on a zero-spacing grid. Coarsening again leads to an overestimation of the streamwise movement of the plasma, partially due to overestimated ion densities on coarser grids, and partially due to the plasma region forming quicker on the coarser grids, as illustrated in Figure 5.1.

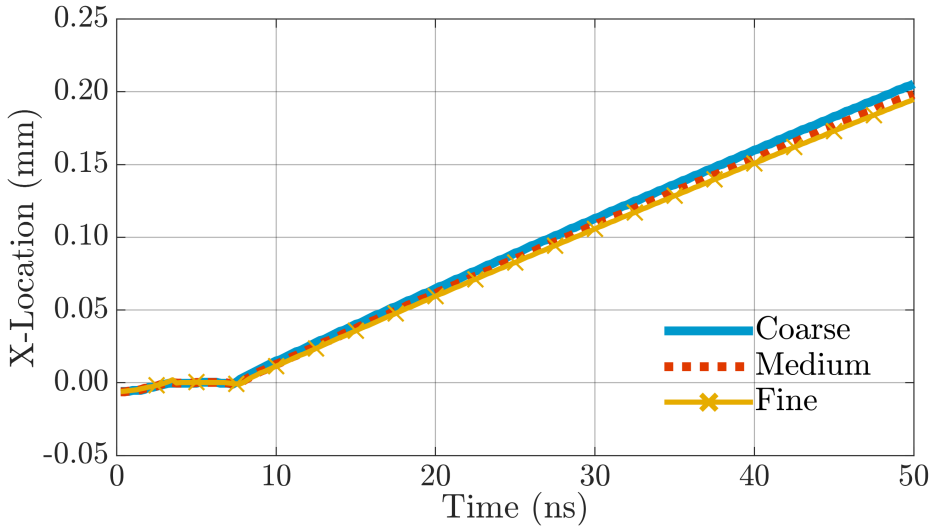

Figure 5.7: X-Location of maximum ion density over 50 ns.

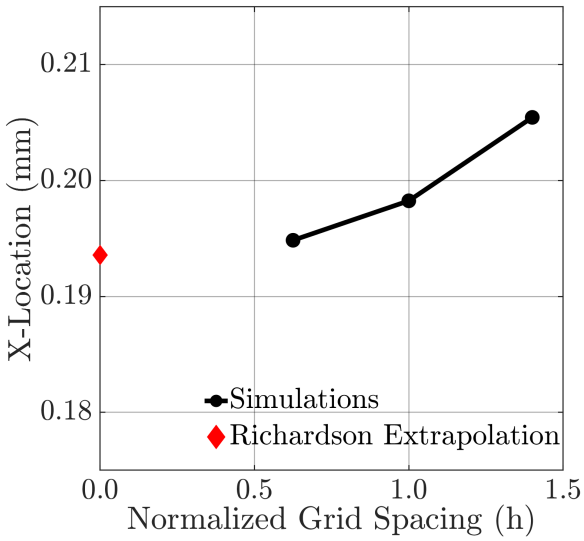

Grid (h)	Max Extent of Plasma [m]
Coarse (1.4)	2.0545×10^{-4}
Medium (1)	1.9825×10^{-4}
Fine (0.625)	1.9484×10^{-4}
Estimated Convergence	1.9357×10^{-4}

Grid Convergence Index	
p	2.7685
GCI_{medium}	3.00%
GCI_{fine}	0.82%

Figure 5.8: GCI analysis for maximum streamwise extent of plasma cloud at 50 ns.

Ultimately, the medium grid was deem suitable for the remainder of the simulations. Although the fine grid offers improved numerical results, the medium grid is shown to follow similar trends while offering a significantly reduced computational cost. The GCI values provide a suitable estimation of the error caused by the medium grid discretization and offer a useful bound within which the solution can be expected to lie. Additionally, the use of similar grids across several species allows for consistent comparison, despite discretization error brought about by the medium grid.

Chapter 6

Results

6.1 Single Species Simulations

Each of the five individual species (N_2, H_2O, CO_2, CO, H_2) is simulated under identical operating conditions to explore the behaviour of the plasma region generated. As the fluid domain is considered quiescent with constant atmospheric pressure and temperature, the salient features of the plasma are dependent on the electrical properties of each fluid. The generation, movement and structure of the plasma are found to be largely dependent on the rate of ionization, rate of recombination and ion mobility. While the shape and structure of the plasma is qualitative, certain metrics are required for a consistent comparison of quantitative results. The degree of ionization, ζ, is the proportion of neutrals that have been ionized:

$$\zeta = \frac{N_+}{(N_+ + N_n)} \tag{6.1}$$

The criteria chosen to define the plasma region within the scope of this work is a minimum degree of $\zeta = 10^{-6}$, which for an ideal gas at atmospheric pressure and temperature, coincides with a minimum ion density of roughly 10^{19} m^{-3} (6 orders of magnitude greater than the initial ion and electron density of 10^{13} m^{-3}). Ion density is also used to quantify the speed at which the plasma propagates downstream along

the dielectric surface. The location of maximum ion density, located at the head of the plasma, is the physical point by which plasma velocity is calculated. The average velocities between 10 and 50 ns are reported in Table 6.1, while the velocity evolution during that time period is shown in Figure 6.16, both found on page 82. The plasma trail then constitutes the region of lower ion density trailing behind the head. The results for each pure species are meant to illustrate the influence of specific electrical parameters (α, β, μ_+), with nitrogen as the basis for comparison. Though ion mobility depends on the local pressure, pressure remains constant, and the values of μ_+ reported henceforth will be for atmospheric pressure of 750 Torr [100 kPa]. Relevant quantities will be reported with an associated percentage [%] in reference to the relative difference between nitrogen and the species being discussed.

6.1.1 Validation Case

Air is the most frequently modelled fluid in the study of DBD plasma which provides a means of validation across various studies. Pure molecular nitrogen, N_2, is commonly used to model air, as the use of a single species greatly reduces computational cost. The coefficient of ionization, α, as a function of E/P, can be found in Figure 6.1, while the coefficient of recombination, β, for N_2 is taken to be constant at 10^{-13} $m^3\,s^{-1}$. N_2^+ ion mobility, μ_+, at 750 Torr is 1.8 $cm^2\,V^{-1}\,s^{-1}$. These values for α, β and μ_+ are the values by which the features exhibited by other species will be compared.

Figure 6.2 shows the generation and movement of plasma in N_2 over 50 nanoseconds. These results are in good agreement with Boeuf and Pitchford, Abdollahzadeh et al. and Murzionak et al. [27, 28, 30] in terms of ion density and velocity. The ion density is on the order of 10^{21} m^{-3}, with a peak ion density of $4.92 \times 10^{21}\,m^{-3}$ at

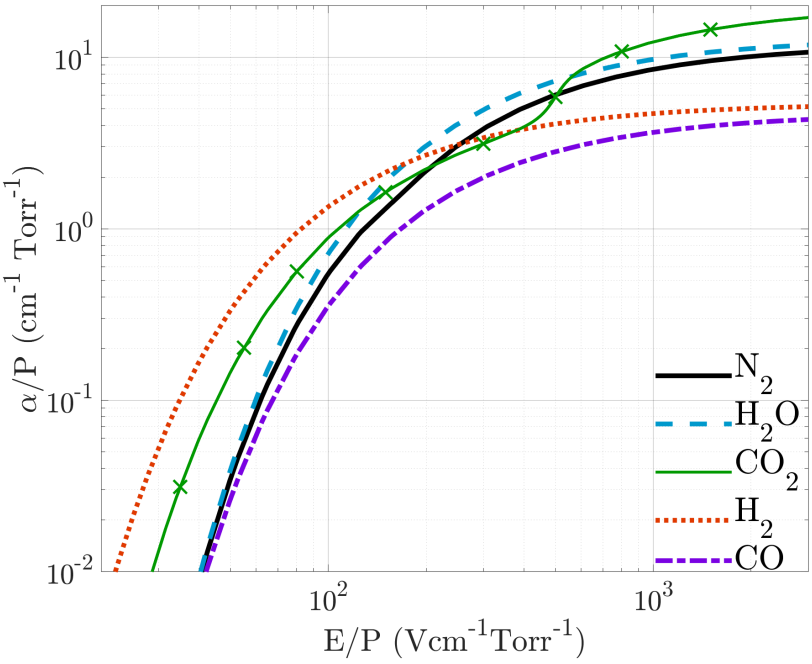

Figure 6.1: Ionization Coefficient, α_i as a function of reduced electric field, E/P. Discontinuities in N_2 and CO_2 due to the change of coefficients A and B in differing regions of applicability. Limits of the chart coincide with the range of E/P simulated.

around 8 ns. Once the plasma has been established at roughly 10 ns, the ion-front propagates parallel to the dielectric surface at an average of $4.65\,\mathrm{mm\,\mu s^{-1}}$.

At 50 ns, the plasma trail along the dielectric surface is fairly evenly distributed, with a high concentration of ions at the head.

The plasma cloud extends to a maximum of 4×10^{-5} m above the dielectric surface. The electric potential, as illustrated by the contour lines in Figure 6.2, have a concentrated gradient at the plasma head responsible for pushing the ions downstream and away from the exposed electrode. While the plasma exhibits quasineutrality, it is not entirely uniform and a non-neutral region is formed at the head of the plasma,

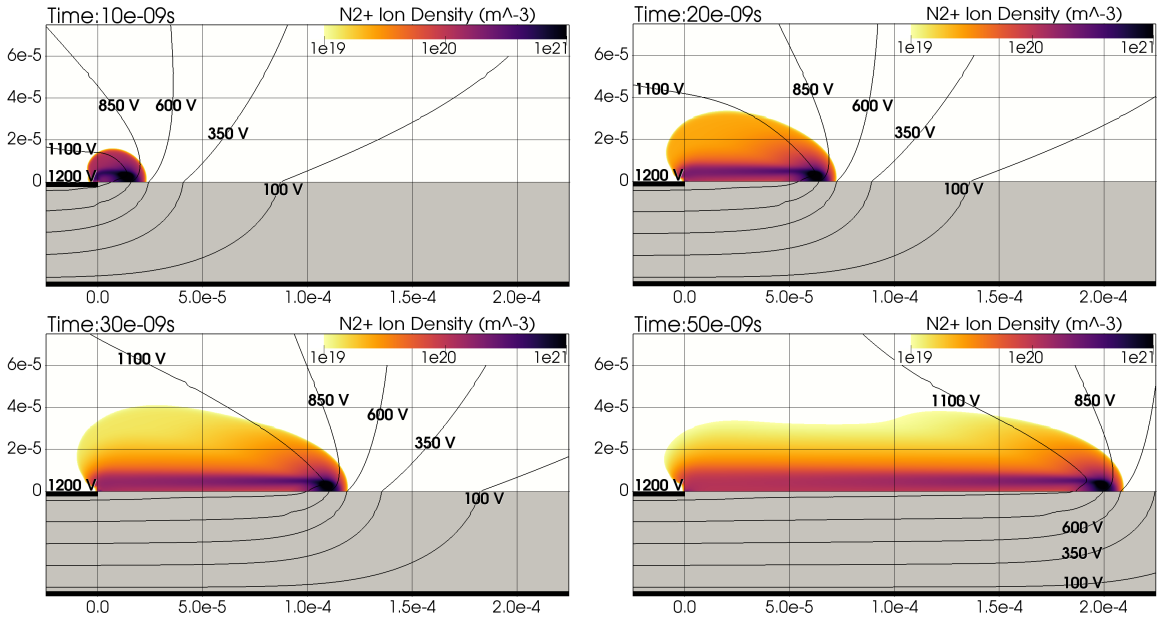

Figure 6.2: Distribution of N_2^+ ion density per cubic meter. Contour lines representing electric field potential, ϕ_E. Axes in meters.

a phenomenon observed by Boeuf and Pitchford [27] and Murzionak et al. [30]. However, the non-neutrality is restricted to the plasma head, and for the bulk of the plasma cloud $N_e \approx N_+$. Thus, the changing electric field is a result of surface charge density. As ions accelerate toward the grounded electrode they accumulate on the dielectric surface, as shown in Figure 6.3, and the potential along the surface rises toward the that of the exposed electrode, 1200 V. Figure 6.3 illustrates the components of the electric potential along the dielectric surface. The dashed curve representing the external potential is unchanging over time, as the applied voltage remains constant at 1200 V. As the plasma evolves, the potential due to charge density, represented by the crossed curve, approaches 1200 V along the dielectric surface, though a small drop in the total voltage, represented by the solid curve, does remain. The potential due to charge density includes both volume charge density, ρ_C, and surface

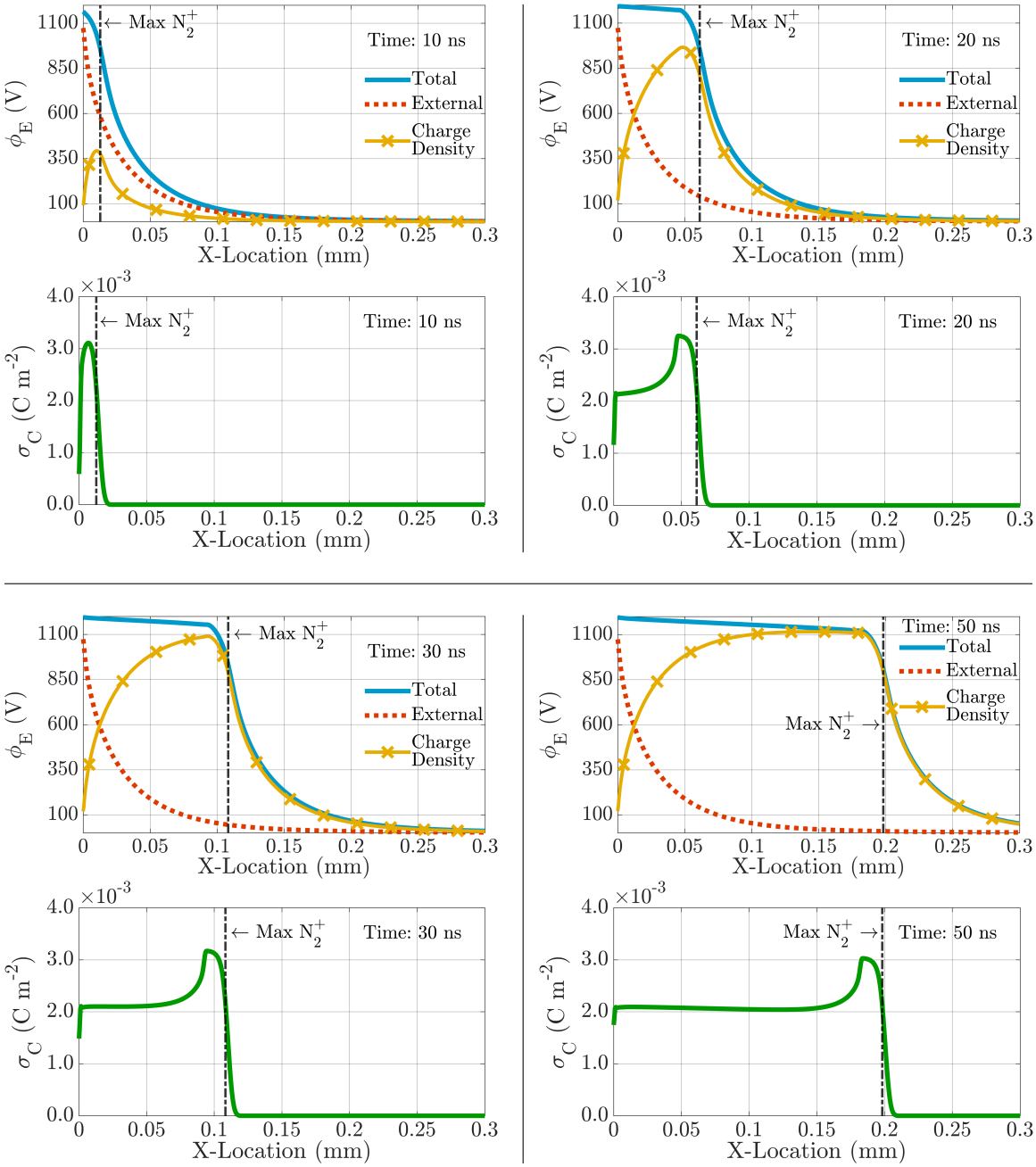

Figure 6.3: Top: Components of ϕ_E along dielectric surface in N_2 plasma. Vertical line indicates location of maximum N_2^+ density. Bottom: Surface charge accumulation due to ions bombarding the dielectric surface.

charge density, σ_C, though it is dominated by the latter. Thus, the exposed electrode is effectively extended along the dielectric to the location of the plasma head, as indicated by the extended plateaus of total electric potential and surface charge density, i.e. the solid potential curve and the σ_C curve in Figure 6.3. Beyond the plasma head, the potential gradient steepens and the potential quickly falls off toward zero.

Figure 6.4 shows the current density per unit width along the exposed electrode, corresponding to the results in Figure 6.2, and compares it to previous works. The large spike in current is an unexpected numerical artifact caused by the assumption of an infinitely thin electrode. Despite the spike of roughly 22 A m^{-1} at 8 ns, by 20 ns the current drops off to previously observed levels around 10 A m^{-1}, following a similar trend to that observed by Boeuf and Pitchford [27] and by Abdollahzadeh et al. [28].

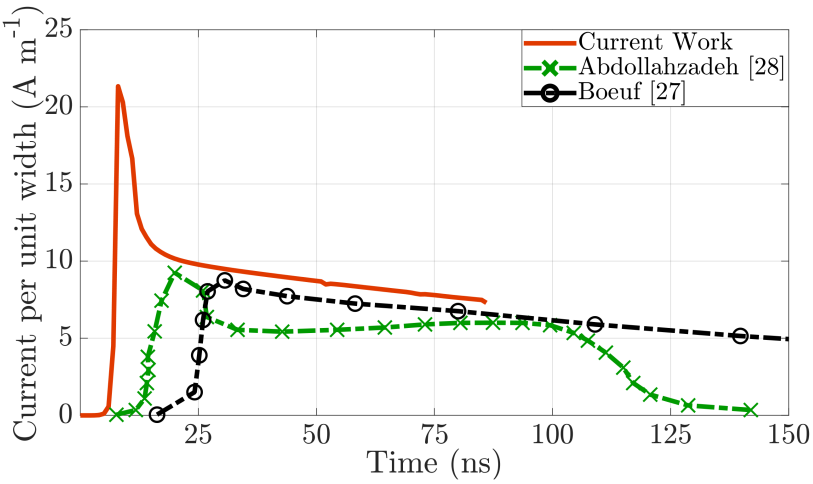

Figure 6.4: Current density per unit width along exposed electrode.

6.1.2 Reduced Coefficient of Recombination

H_2O and N_2 possess a similar rate of ionization over the range of E/P simulated, 0–3000 $\mathrm{V\,cm^{-1}Torr^{-1}}$, as demonstrated in Figure 6.1. The recombination coefficient of H_2O, $0.66 \times 10^{-13}\,\mathrm{m^3\,s^{-1}}$ [66%], and H_2O^+ ion mobility, $1.181\,\mathrm{cm^2\,V^{-1}\,s^{-1}}$ [65.6%], are both lower than in N_2. Figure 6.5 shows the plasma cloud in H_2O (top) with that of N_2 mirrored across the horizontal axis (bottom) for direct comparison. Peak H_2O^+ ion density of $8.35 \times 10^{21}\,\mathrm{m^{-3}}$ [169.7%] occurs at 7 ns. However, unlike N_2, these ions linger in higher densities due to the reduced coefficient of recombination of H_2O^+. This effect is best illustrated at 20 and 30 ns of Figure 6.5, in which there is a dark line extending from the plasma head back to the exposed electrode. Figure 6.6 highlights the plasma trail with a ion density contour line at $2.5 \times 10^{20}\,\mathrm{m^{-3}}$. This decreased rate of recombination does not seem to significantly impact the structure

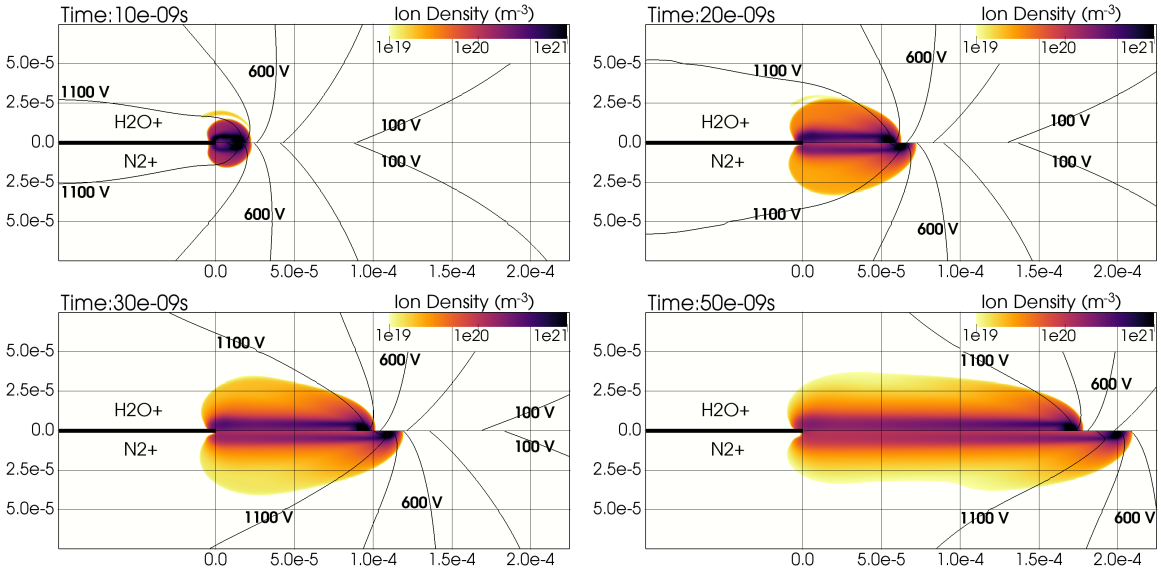

Figure 6.5: Comparison of H_2O and N_2 plasma propagation. The H_2O has a similar ion density to N_2 and propagates slightly slower than CO_2. Axes in meters.

of the plasma, as both H_2O and N_2 exhibit similar plasma cloud shapes, with the electric potential gradient concentrated in the plasma head. The reduced mobility of H_2O^+ ions causes the plasma head in H_2O to travel at a slightly lower average velocity of $3.90\,\mathrm{mm\,\mu s^{-1}}$ [83.9%].

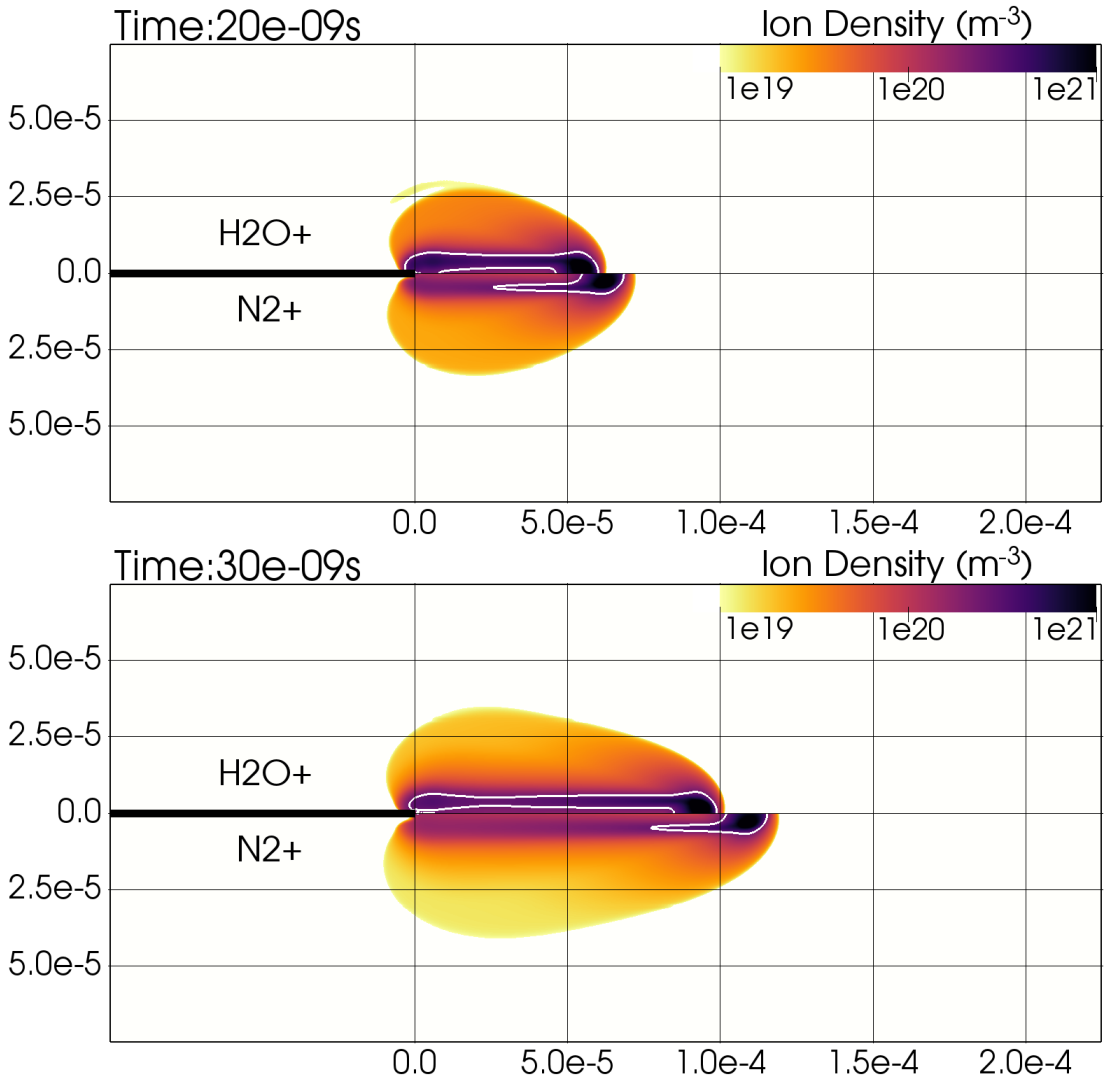

Figure 6.6: Comparison of H_2O and N_2 at 20 and 30 nanoseconds. The contour line at $2.5 \times 10^{20}\,\mathrm{m^{-3}}$ illustrates the pronounced plasma trail in H_2O due to the lower coefficient of recombination.

6.1.3 Increased Coefficient of Recombination

Conversely, the coefficient of recombination of CO_2^+, $11.06\,m^3\,s^{-1}$ [1106%], is an order of magnitude greater than N_2^+, and the CO_2^+ ions are quickly neutralized rather than lingering above the dielectric. Figures 6.7 and 6.8 illustrate the unique plasma structure found in CO_2 as a result. CO_2^+ ion density peaks at $5.26 \times 10^{21}\,m^{-3}$ [106.9%] at 7 ns, slightly greater than that of N_2 as expected from the increased ionization coefficient (Figure 6.1). With the increased rate at which ions recombine with electrons to form neutrals, the plasma trail seen in H_2O and N_2 is significantly shortened in the case of CO_2. Instead, the high density of ions is localized within a triangular region near the head of the plasma, with a gap of lower ion density between the

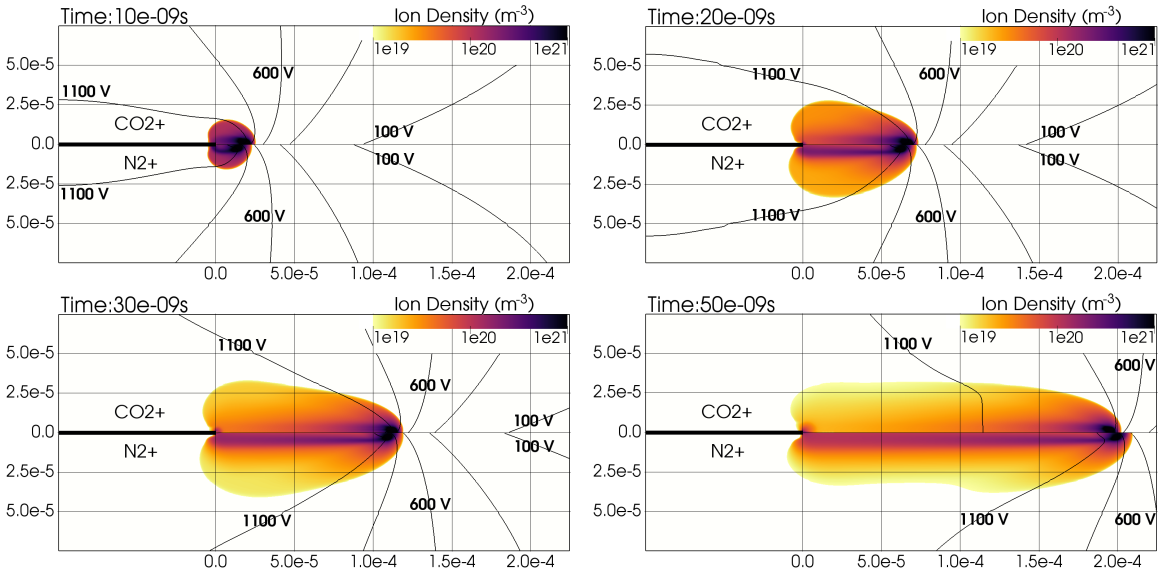

Figure 6.7: Comparison of CO_2 and N_2 plasma propagation. The CO2 has a greater density of positive ions at the head, but propagates slower due to lower ion mobility. Axes in meters.

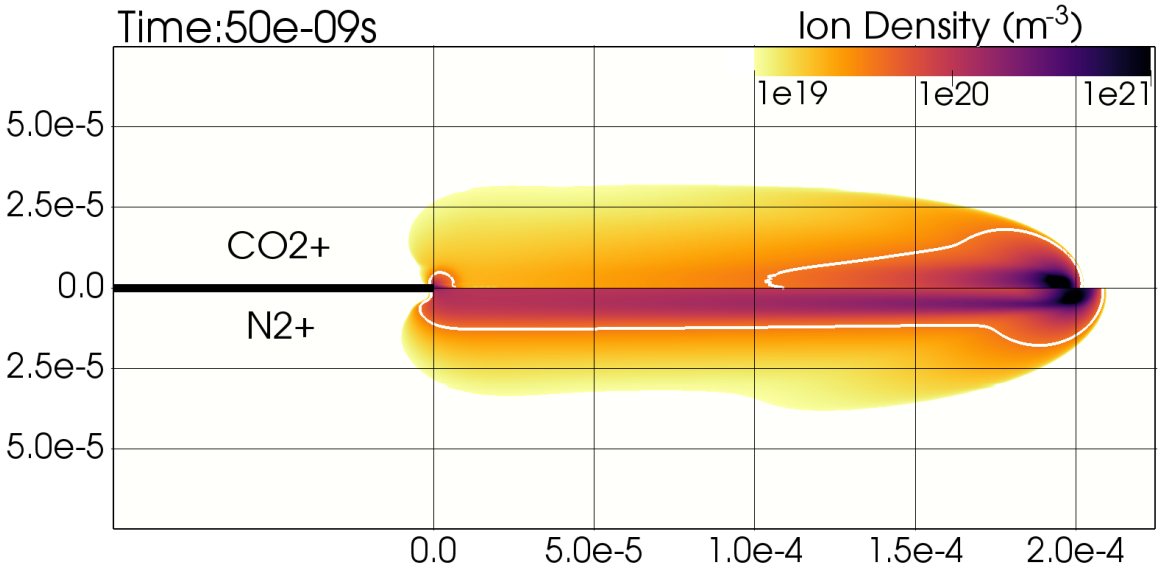

Figure 6.8: Ion density in CO_2 (top) and N_2 (bottom) at 50 ns. Highlighted by ion density contour of $4 \times 10^{19}\,\mathrm{m}^{-3}$ illustrating effect of heightened recombination in the plasma trail.

electrode and the head, as shown in Figure 6.8. Though the electric potential contours are mainly located in the plasma head of CO_2, at 50 ns some of that gradient has been shifted backward into the plasma trail due to the decreased surface charge accumulation behind the plasma head. The previously mentioned effect seen in N_2 and H_2O, by which the exposed electrode is effectively extended, is lessened in the case of CO_2. Ion mobility in CO_2, $1.302\,\mathrm{cm}^2\,\mathrm{V}^{-1}\,\mathrm{s}^{-1}$ [72.3%], is also slightly reduced and the average plasma velocity in CO_2 is $4.39\,\mathrm{mm}\,\mu\mathrm{s}^{-1}$ [94.4%].

There is also a small region of higher CO_2^+ ion density adjacent to the exposed electrode at 30 and 50 ns. It is unlikely that ions would remain in such close proximity to the exposed electrode, and this is instead thought to be a numerical artifact. The assumption of an infinitely thin electrode has improved stability and computational cost in the simulations, but has resulted in electrons moving toward the infinitely

thin right edge of the electrode. This essentially squeezes large quantities of electrons into a very limited region, resulting in inflated ion production. This artifact is most prominent in CO_2 due to the lack of a distinguished plasma trail, as discussed above.

6.1.4 Decreased Rate of Ionization

Due to the low rate of CO^+ ionization over the entire range of E/P modelled in these simulations (see Figure 6.1), it is expected that the CO^+ ion density will be lower than all other species modelled. Figure 6.9 compares the generation of CO^+ ions with that of N_2^+ ions, noting that the lower bound of ion density is reduced to 10^{16} m^{-3} in order to resolve the CO^+ ion cloud. The maximum CO^+ ion density reached at 50 ns, $6.7 \times 10^{19}\,m^{-3}$ [1.36%], is 2 orders of magnitude lower than that of the maximum N_2^+ ion density. It appears that, in atmospheric conditions, an applied potential of

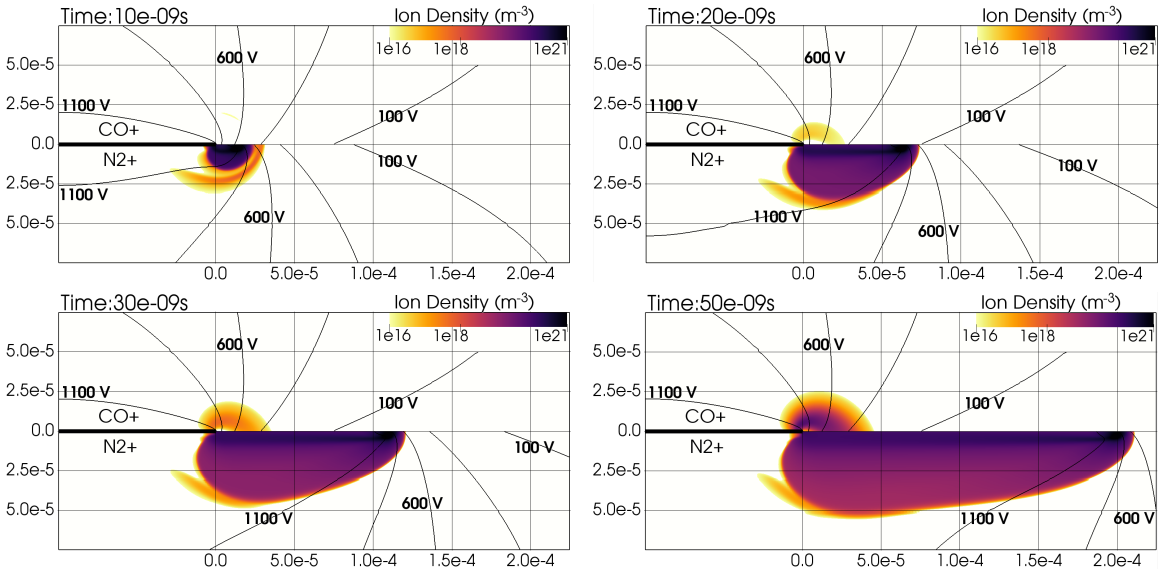

Figure 6.9: Comparison of CO and N_2 plasma propagation. The CO^+ ions take much longer to form, and at a far lower density. Note the change to $10^{16}\,m^{-3}$ for the lower bound of ion density. Axes in meters.

1200 V does not sufficiently generate a plasma cloud in CO gas. However, a region of lower density CO^+ ions is ultimately generated, and it must be considered that the ionization process is simply delayed rather than inhibited entirely. Longer simulations are needed to confirm whether plasma can be generated in CO under these conditions and as such, a quantification of the plasma velocity cannot confidently be made.

6.1.5 Increased Ion Mobility

Finally, the mobility of ions is shown to have a significant impact on the behaviour of the plasma. H_2^+ ions have a mobility of $8.73\,\mathrm{cm^2\,V^{-1}\,s^{-1}}$ [485%]. Figures 6.10–6.11 compare the plasma region generated in H_2 with that of N_2. Note that because the plasma propagates further in H_2, the plots in Figures 6.10–6.11 have been extended

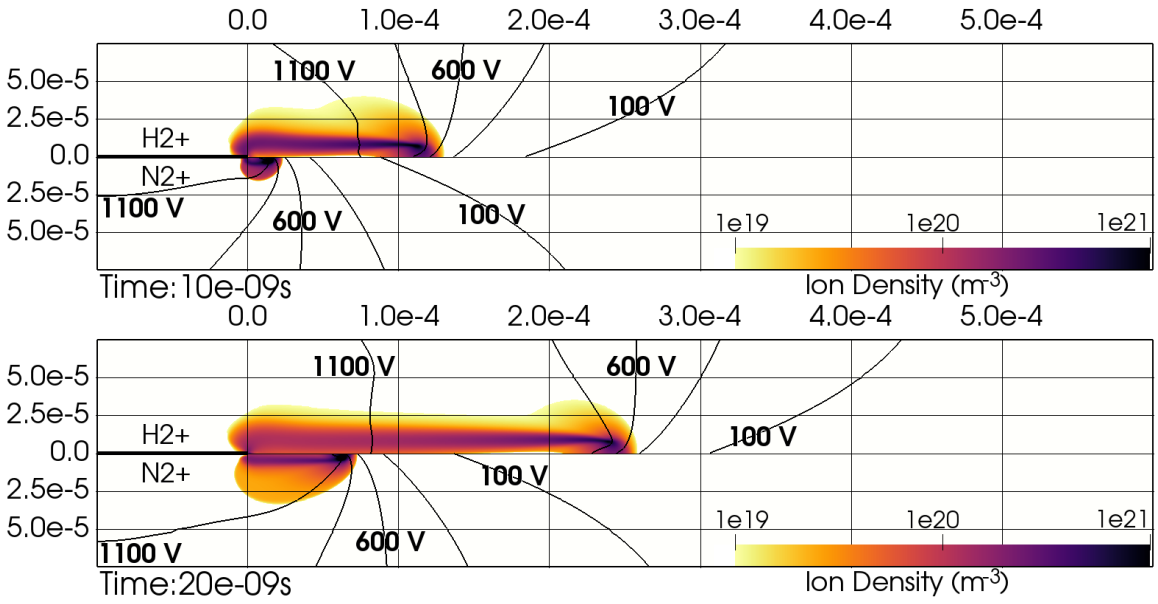

Figure 6.10: Comparison of H_2 and N_2 plasma propagation at 10 ns and 20 ns. Axes in meters.

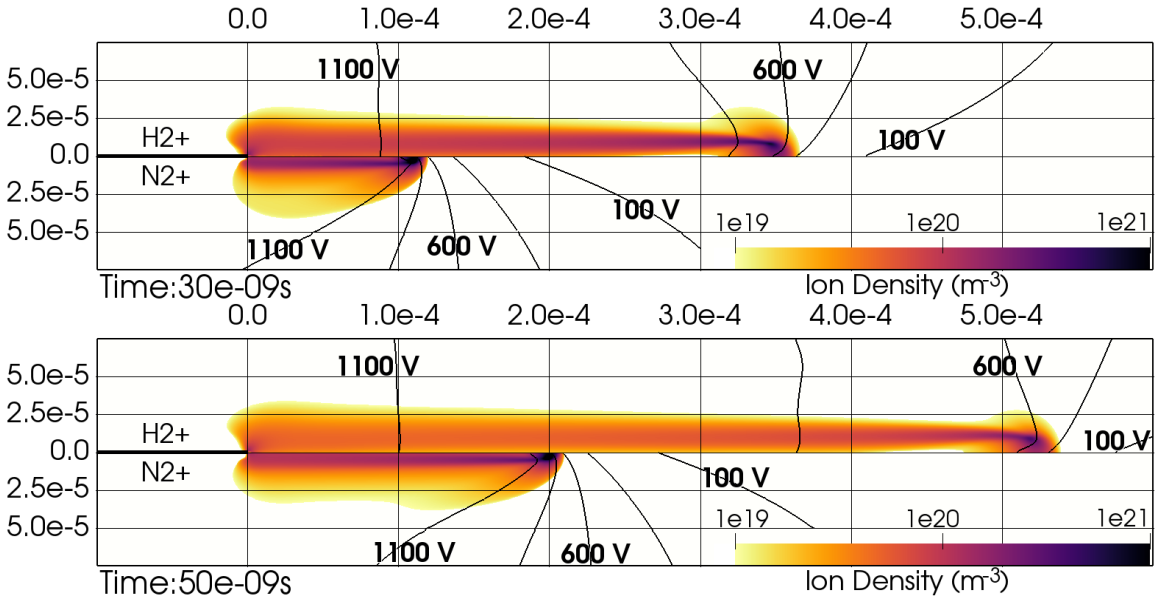

Figure 6.11: Comparison of H_2 and N_2 plasma propagation at 30 ns and 50 ns. Axes in meters.

from 0.2 mm to 0.6 mm. The H_2^+ ion density is slightly lower than N_2^+, with a peak ion density of $1.61 \times 10^{21}\,\mathrm{m}^{-3}$ [32.7%] at 6 ns. The plasma head propagates along the dielectric surface at an average of $10.27\,\mathrm{mm\,\mu s}^{-1}$ [220.9%], but unlike previous species, the movement is no longer constant. As the plasma head extends away from the exposed electrode, its movement is reduced. The coefficient of recombination in H_2 is $2.8\,\mathrm{m}^3\,\mathrm{s}^{-1}$ [280%], though both N_2 and H_2 exhibit similar plasma trails in the first 20 ns. However, the increased ion mobility and plasma velocity cause the H_2^+ plasma cloud to diffuse at a greater rate. By 50 ns, peak H_2+ ion density has been reduced to $3.95 \times 10^{20}\,\mathrm{m}^{-3}$ [16.6%], and the ion density in the trail is visibly lower than that of N_2. As mentioned in the case of CO_2, there is a streamwise gradient in the electric potential behind the plasma head, as illustrated by the contour lines in Figures 6.10–6.11. As shown in Figure 6.12, the electric potential between the electrode and

the plasma head has a steeper gradient in the case of H_2 as the surface charge accumulation is limited, and the previously discussed extension of the exposed electrode is lessened. In the case of CO_2, it was the high rate of recombination that restricted the growth of a surface charge, as ions were neutralized at a greater rate. In H_2, the high ion mobility allows for the plasma to be pushed further downstream, decreasing the rate at which ions reach the dielectric surface and limiting the concentration of a surface charge density.

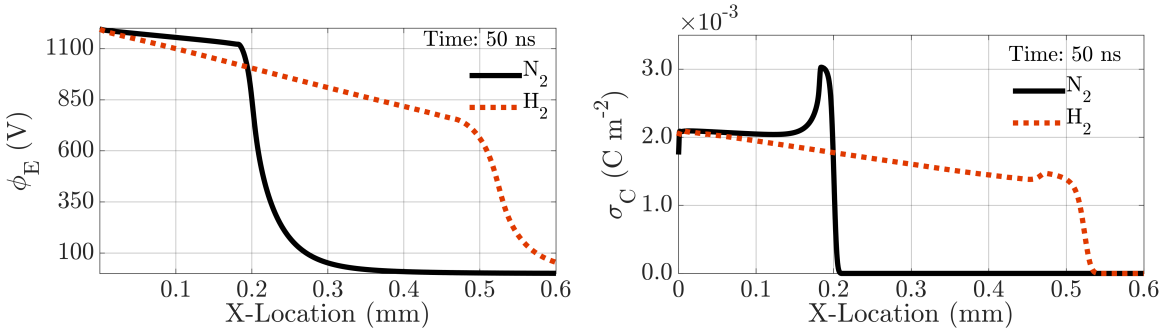

Figure 6.12: Electric potential, left, and surface charge density, right, along the dielectric surface in N_2 and H_2 at 50 ns.

6.1.6 Increased N_2^+ Mobility

Given that each of the species possess unique electrical properties (α, β, μ_+), the distinctive results in H_2 might not be solely dependent on ion mobility. To better understand the extent to which ion mobility alters the plasma region, N_2 was modelled again, changing only its value of μ_+. This fictitious species is identical to N_2 in all respects, except that its ion mobility is increased to 8.73 $cm^2\,V^{-1}\,s^{-1}$, equal to that of H_2^+ mobility at 750 Torr. Figure 6.13 compares this fictitious species to the control case of N_2, in which standard N_2^+ mobility is 1.8 $cm^2\,V^{-1}\,s^{-1}$. Thus, any difference

between the two can only be attributed to the difference in ion mobility.

While ion densities are initially comparable on the order of $10^{21}\,\mathrm{m}^{-3}$, maximum

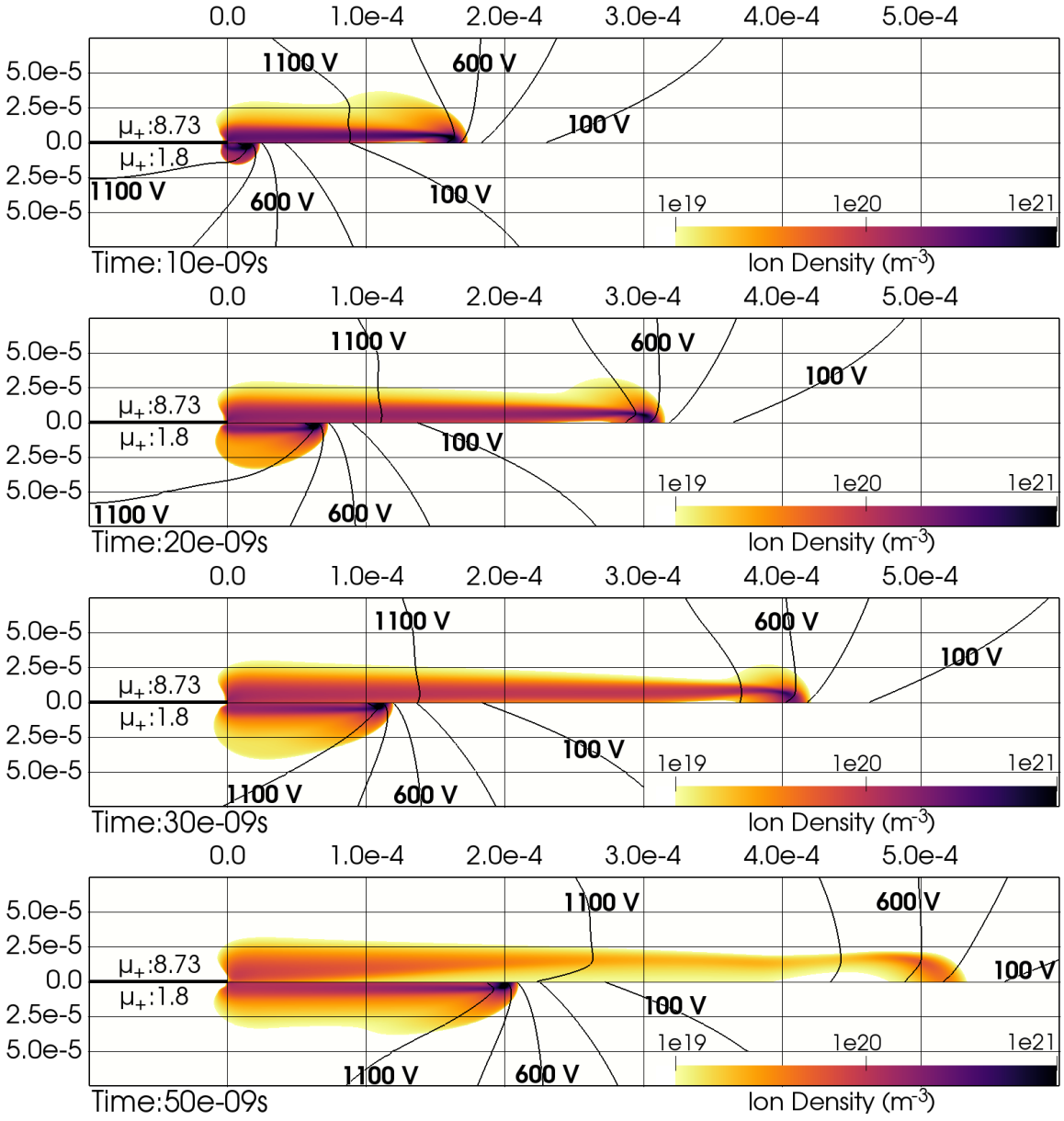

Figure 6.13: N_2 modified with an increased ion mobility of 8.73 $\mathrm{cm}^2\,\mathrm{V}^{-1}\,\mathrm{s}^{-1}$ (top) compared to N_2 with a standard ion mobility of 1.8 $\mathrm{cm}^2\,\mathrm{V}^{-1}\,\mathrm{s}^{-1}$ (bottom).

ion density is only $3.15 \times 10^{21}\,\mathrm{m}^{-3}$ [64.0%]. However, the speed at which the plasma propagates across the dielectric surface is significantly increased. With a 485% increase to N_2^+ ion mobility, the plasma propagates at an average of $9.87\,\mathrm{mm\,\mu s}^{-1}$ [212%], far quicker than that of the N_2 control case. In comparison to H_2, though the ion mobility of the fictitious N_2 and H_2 gases are equal, the plasma velocity still differs. As shown in Figures 6.14–6.15, in the initial 30 ns, the fictitious N_2 propagates even faster than H_2. This suggests that the streamwise plasma velocity is partially influenced by the differing rates of ionization and recombination as well, though ion mobility appears to be the dominant factor. Figures 6.14–6.15 also demonstrate the similarities that arise when ion mobility is equal in each gas, as both cases exhibit similar plasma structure and ion density. Alterations to the electric potential gradient are also evident, which were earlier attributed to the heightened ion mobility of H_2^+.

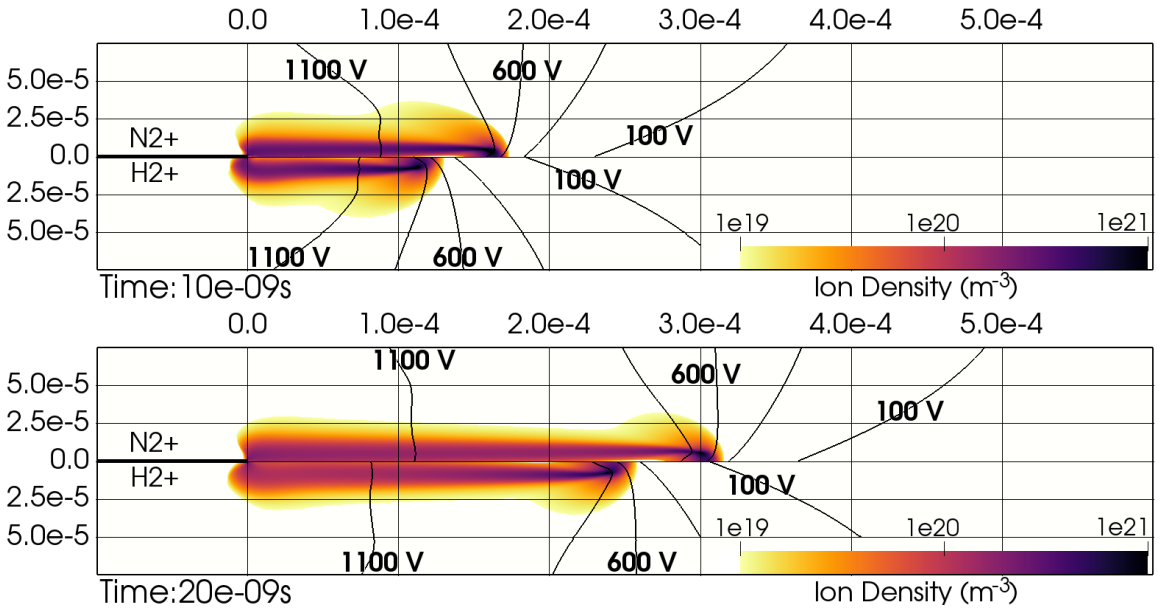

Figure 6.14: N_2 (top) modified with an increased ion mobility of $8.73\,\mathrm{cm}^2\,\mathrm{V}^{-1}\,\mathrm{s}^{-1}$ compared to H_2 (bottom), which possesses an equal ion mobility, at 10 ns and 20ns.

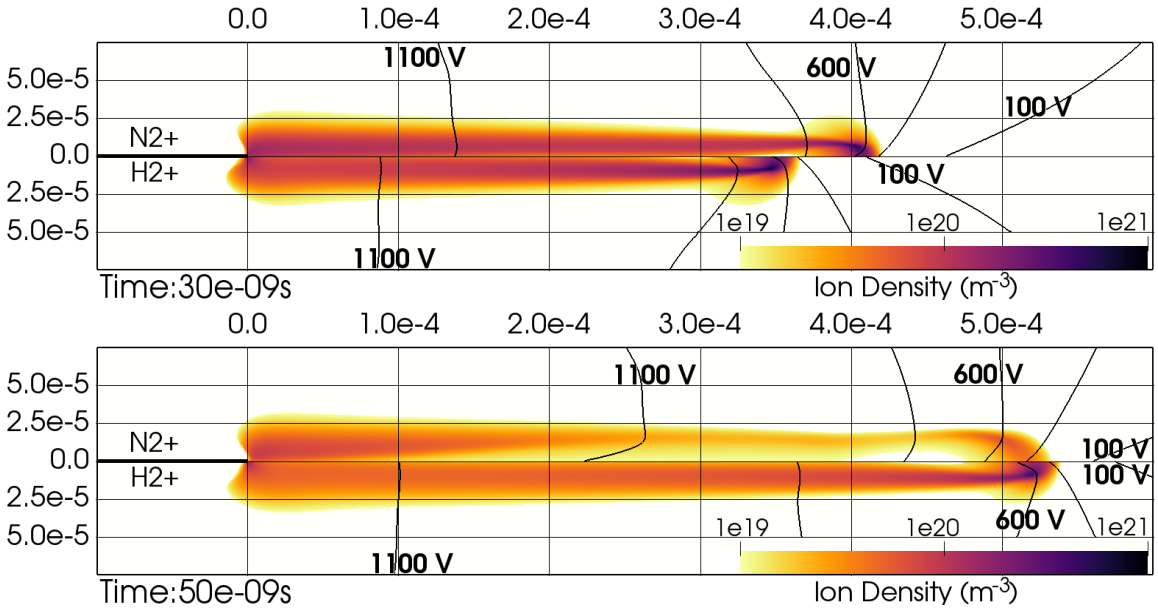

Figure 6.15: N_2 (top) modified with an increased ion mobility of 8.73 $cm^2\,V^{-1}\,s^{-1}$ compared to H_2 (bottom), which possesses an equal ion mobility, at 30 ns and 50ns.

Despite the low mobility of ions relative to electrons, ion mobility is shown to be a key factor in facilitating the movement of the plasma.

6.1.7 Plasma Velocity

Table 6.1 summarizes the average velocity of the plasma and the associated ion mobility for each pure species, while Figure 6.16 shows the change in velocity over time. The discrete velocity at each nanosecond time-step has been fitted to a 3rd-order polynomial. Plasma propagation in the first 10 ns is not considered, as the plasma region is still forming during this time. The plasma velocity dependence on ion mobility is again highlighted, but it also clear that the high mobility of H_2^+ does not sustain the inflated velocity. As the ion front diffuses in the case of H_2, the propagation of the

Table 6.1: Plasma velocities averaged from 10–50 ns, with associated ion mobility at atmospheric pressure, 750 Torr [100 kPa].

Species	**Ion Mobility at 750 Torr** $[cm^2\,V^{-1}\,s^{-1}]$	**Average Plasma Velocity** $[mm\,\mu s^{-1}]$
N_2	1.8	4.65
H_2O	1.181	3.90
CO_2	1.302	4.39
CO	1.6	-
H_2	8.73	10.27

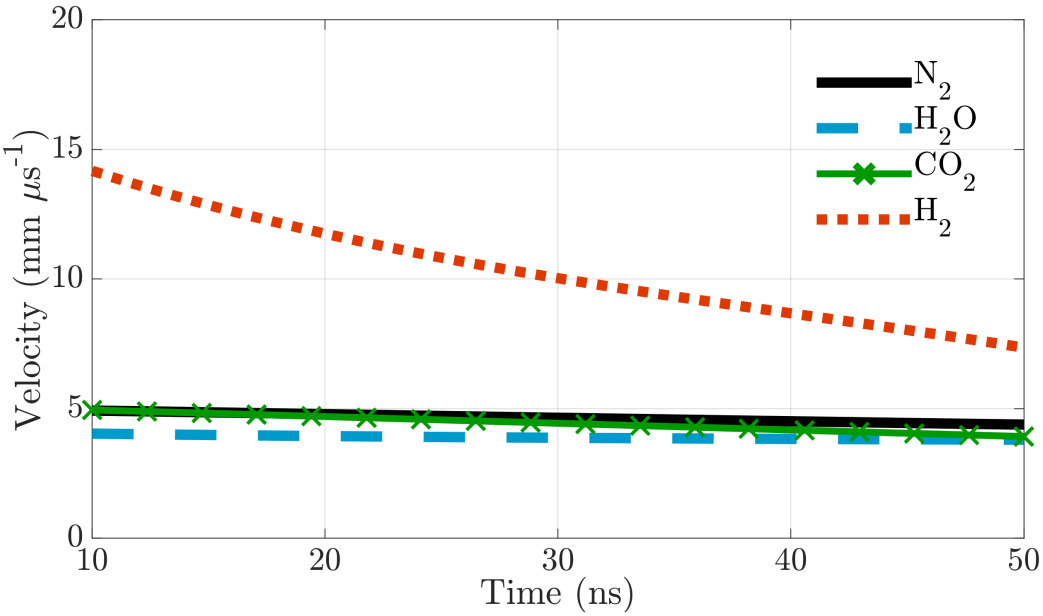

Figure 6.16: Plasma front streamwise velocity between 10 and 50 ns, fitted to a 3rd-order polynomial. CO omitted, as the plasma region was not sufficient enough to discern the movement of the plasma front.

plasma falls off toward the values observed in N_2, H_2O and CO_2. This is expected, in that as the ion front gets further from the exposed electrode and the ion density

drops, the net force exerted on the ions decreases, hindering the ion movement.

6.1.8 Current

Shown in figure 6.17 is the current per unit width across the exposed electrode. In all cases an unexpected current spike is generated in the first 10 ns, aside from CO, in which the ionization is not sufficient to generate any appreciable current. Its been determined that this spike is a result of assuming an infinitely thin exposed electrode. Modelling the electrode with finite thicknesses on the order of a few µm reduces the spike, regardless of whether the electrode is flush with the dielectric or protruding above it. The magnitude of the spike is directly related to the rate of ionization, as species with greater rates of ionization will produce greater quantities of electrons that facilitate the production of current through the electrode. By 20 ns, each species returns to acceptable levels of current density as shown in Figure 6.4, following similar

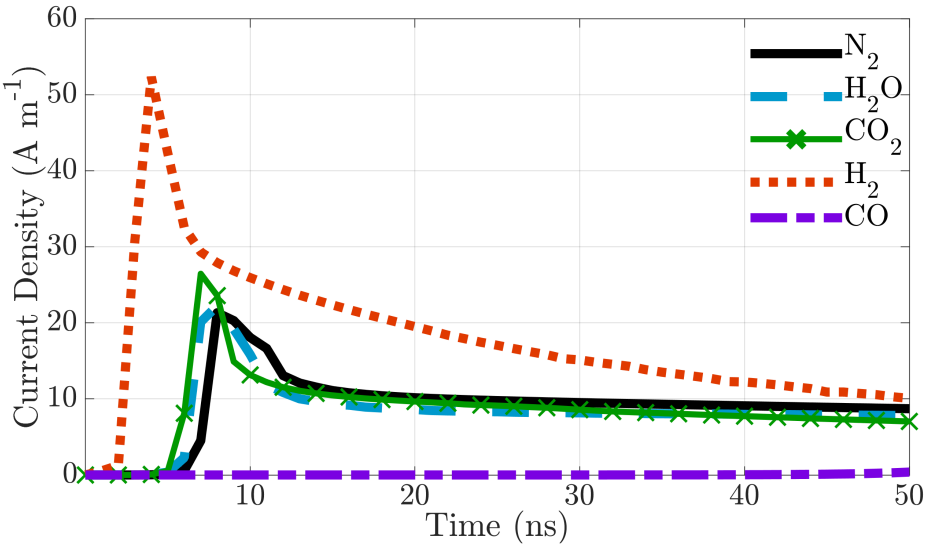

Figure 6.17: Current per unit width of the exposed electrode.

trends as the ion front moves away from the exposed electrode, limiting the electron density in the region of the exposed electrode.

6.2 Mixture Simulations

6.2.1 Binary Mixtures

Having simulated plasma generation for several single species, modelling was extended to various mixtures of species. CO was seeded with different proportions of H_2 in an attempt to induce appreciable ionization of CO neutrals. It was found that as little as 5% H_2 on a number density basis was enough to increase CO ionization, while a 60:40 CO-to-H_2 mixture further increased CO ionization, along with facilitating a discernible plasma velocity. Identical operation conditions and computational mesh were applied to all mixtures, while the governing equations were modified to account for changes to ionization and recombination rates, which now depend on the number density fraction of each neutral species. The density of neutrals was expected to fluctuate as ionization proceeded, though it was determined that ionization caused the total neutral density to drop by no more than 0.02%, and to drop by no more than 0.03% for any given neutral species.

95:5 CO:H_2 Mixture

Figure 6.18 compares the CO^+ ion density in a 95:5 CO:H_2 molar basis mixture (top) and in pure CO (bottom). Again, the lower bound of the ion density scale is reduced to $10^{16}\,\mathrm{m}^{-3}$ in order to resolve the low ion density in pure CO. As shown in Figure 6.9, ionization was inhibited or delayed in pure CO, whereas introducing 5%

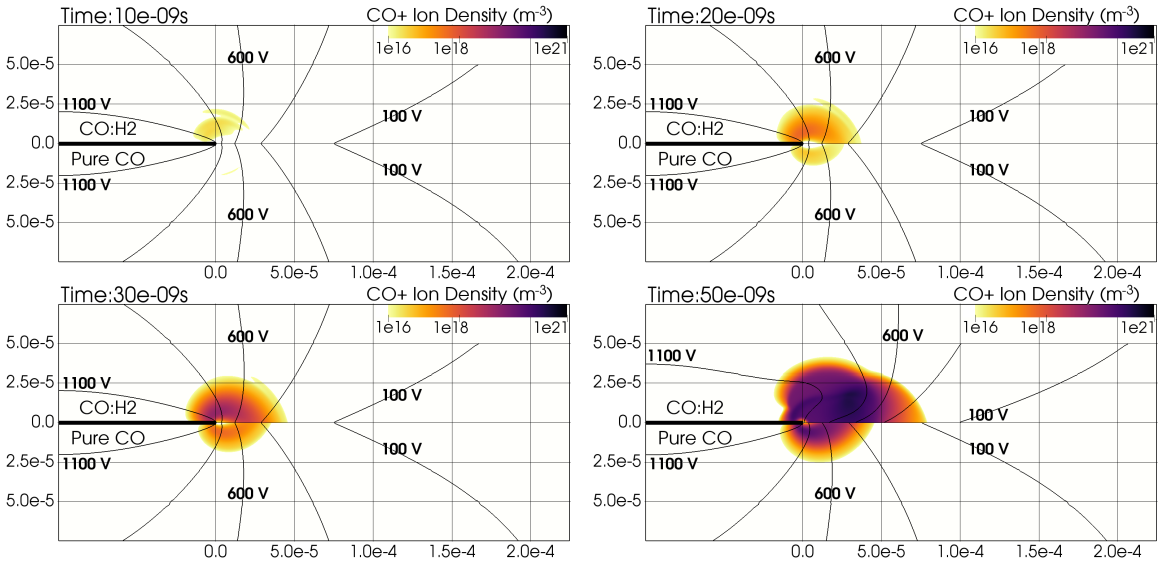

Figure 6.18: Comparison of CO^+ ion density between a 95:5 CO:H_2 mixture and pure CO. H_2 stimulates ionization of CO in the mixture, while pure CO ionization is inhibited or delayed.

H_2 to the fluid region allows for a greater degree of CO^+ to be generated. H_2, being more susceptible to ionization, generates higher densities of free electrons which then increase the rate at which CO is ionized. However, the low percentage of H_2 present here does not facilitate CO^+ densities on the same order of magnitude as those seen in pure N_2, CO_2, H_2O or H_2. Peak ion density of $6.44 \times 10^{20}\,\mathrm{m}^{-3}$ [13.1%] is reached at 40 ns, with CO^+ making up 97.7% of the peak ion density. Though the mobility of CO^+ ions is similar to that of N_2^+ ions, the plasma cloud here is relatively stationary and grows upward rather than moving downstream, thus a definite plasma velocity cannot yet be determined.

60:40 $CO:H_2$ Mixture

Increasing the percentage of H_2 present in the mixture further facilitates the ionization of CO and produces a plasma cloud similar to what was observed in the previous pure species. Figures 6.19–6.20 compares the total ion density (CO^+ and H_2^+) in a 60:40 $CO:H_2$ mixture (top) with the ion density in N_2 (bottom). The plasma region now

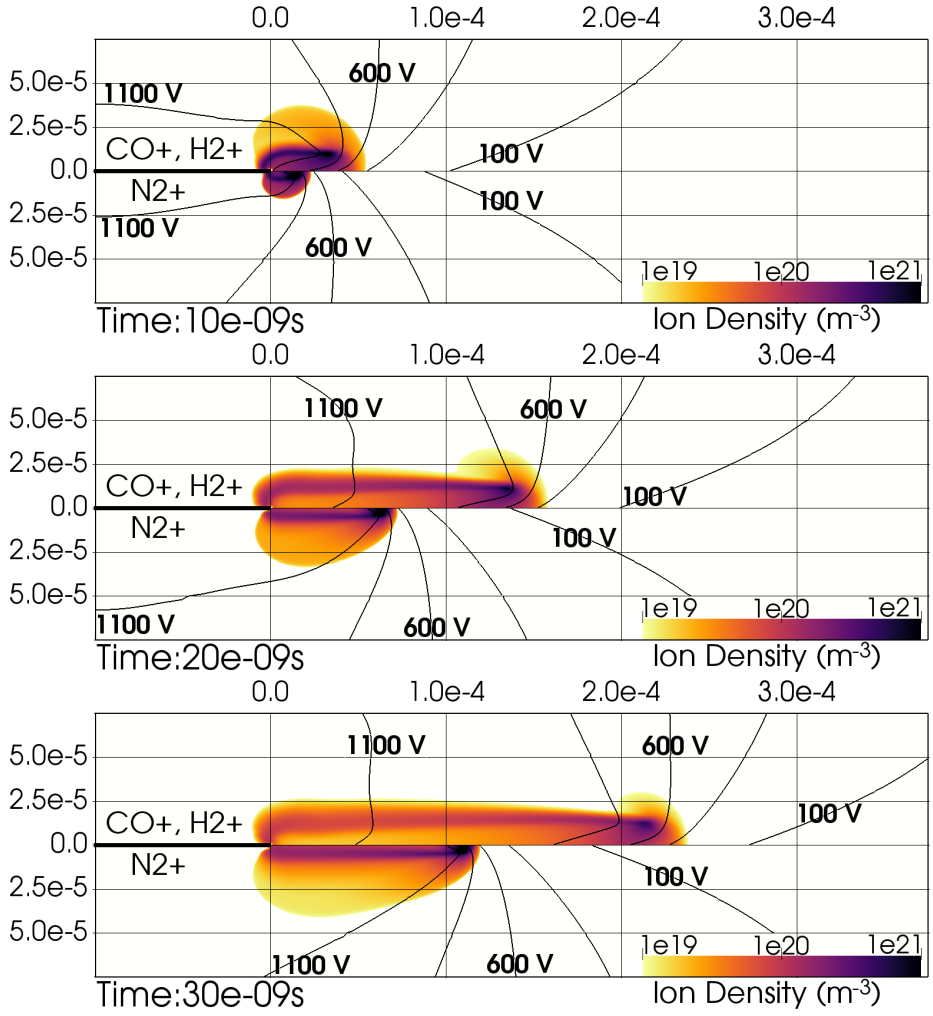

Figure 6.19: Total ion density (CO^+ and H_2^+) in 60:40 mixture (top) compared to N_2^+ density of validation case (bottom), at 10, 20 and 30 ns.

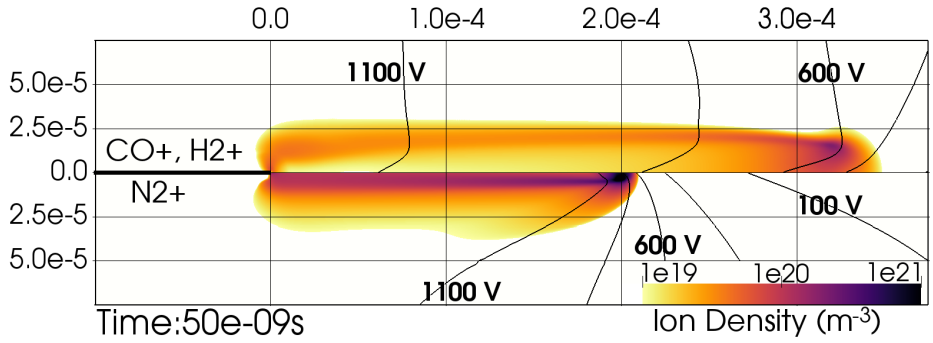

Figure 6.20: Total ion density (CO^+ and H_2^+) in 60:40 mixture (top) compared to N_2^+ density of validation case (bottom), at 50 ns.

extends much further along the dielectric surface in the 50 ns period, where it had previously been restricted to the region just adjacent the exposed electrode in the cases of pure CO and the 95:5 CO-H_2 mixture. Given that the ionization of H_2 is what facilitates the ionization of CO, it would follow that the location of highest densities of CO^+ would coincide with the highest densities of H_2^+. It has been shown that the higher ion mobility and ionization rates of H_2 cause the plasma to extend further along the dielectric and produce a streamwise electric potential gradient, and that same effect is seen here. The high mobility of H_2^+ and the relatively high coefficient of recombination of CO^+ results in the low ion density plasma trail.

Figure 6.21 shows the same 60:40 CO:H_2 mixture, but isolates each ion species, with CO^+ density on top and H_2^+ density below. Maximum total ion density of $1.51 \times 10^{21}\,\mathrm{m}^{-3}$ [30.6%] is reached at 10 ns, with CO^+ making up 76.1% of the peak density. As expected, the regions of high CO^+ density are located where H_2^+ densities are high, such that large numbers of free electrons are able to ionize CO. The plasma trail is largely composed of H_2^+, in regions where electron density is not great enough to sufficiently ionize CO, and the relatively high recombination coefficient of

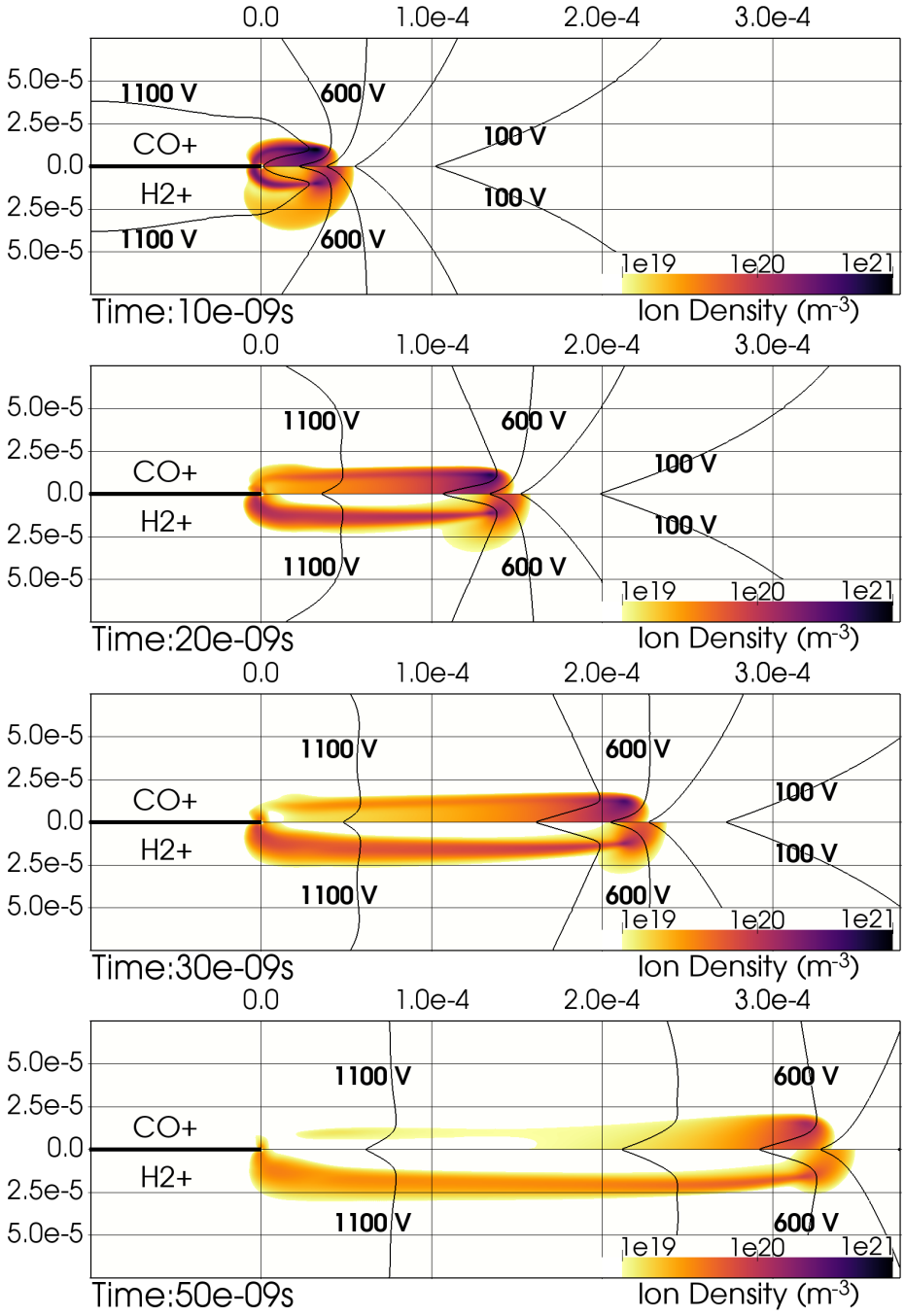

Figure 6.21: Isolated ion densities of 60:40 mixture.

CO^+ ($\beta = 6.8 \times 10^{-13}\,\mathrm{m^3\,s^{-1}}$) has extinguished most of the lingering CO^+ ions. The movement of the plasma downstream allows the plasma velocity to be calculated at $7.20\,\mathrm{mm\,\mu s^{-1}}$[154.8%], largely attributed to the high mobility of H_2^+.

6.2.2 Exhaust Mixture

Finally, modelling was extended to a mixture of gases that would commonly be found in a post-combustion environment. The products of combustion generated by SpaceX's Merlin 1D+ engine, fueled by refined petroleum-1 and liquid oxygen (RP-1/LOx), can be found in table 6.2 [1]. Only species contributing $\geq 5\%$ on a mass basis are considered to limit computational cost. Thus, the mixture consists of CO, H_2O, H_2 and CO_2, with the initial number density fractions listed in Table 6.2.

Given that H_2 composes nearly 70% of the mixture on a number density basis, it is expected that the mixture will exhibit qualities similar to pure H_2, and Figure

Table 6.2: Top: Mass composition of exhaust generated by Merlin 1 D+ engines [1]. Bottom: Composition of exhaust mixture simulated.

Species	Mass Percentage (%)	Species	Mass Percentage (%)
CO	39.5470	O	0.1935
H_2O	30.7060	O_2	0.1520
H_2	15.0240	HCO	0.0047
CO_2	9.7310	COOH	0.0018
H	2.2984	HO_2	0.0014
OH	2.3384		

Species	H_2	H_2O	CO	CO_2
Number Density Fraction (%)	69.0699	15.7961	13.0848	2.0492

6.22 compares the mixture (top) to that of pure H_2 (bottom). The total ion density in the mixture peaks at $2.86 \times 10^{21}\,\mathrm{m}^{-3}[58.1\%]$, which is 177.5% that of the peak ion density in pure H_2, increased due to the presence of other species. The mixture

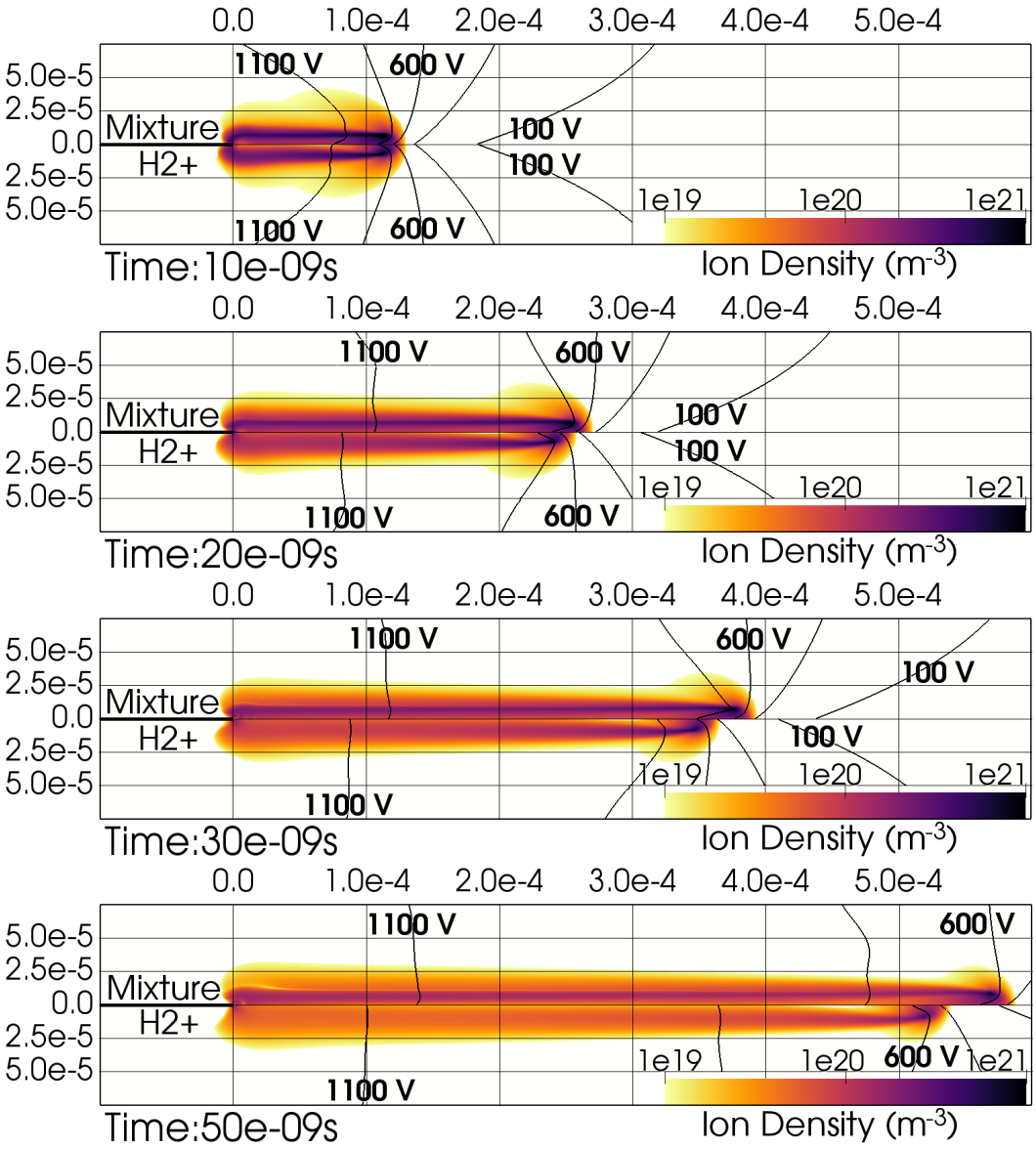

Figure 6.22: Total ion density of mixture (H_2^+, H_2O^+, CO^+, CO_2^+) compared to pure H_2^+ ion density.

moves streamwise at an average of 11.59 mm µs^{-1}[249.2%], 112.9% that of the velocity in pure H_2.

Figure 6.23 illustrates these similarities, as the current density and plasma movement in H_2 and the mixture both follow similar trends at comparable magnitudes. As seen in H_2, the plasma velocity is not constant, and decreases as the plasma head moves downstream and diffuses. Further, the surface charge responsible for altering the electric potential exhibits similar trends in both cases, as shown in Figure 6.24, giving rise to the potential drop along the length of the plasma.

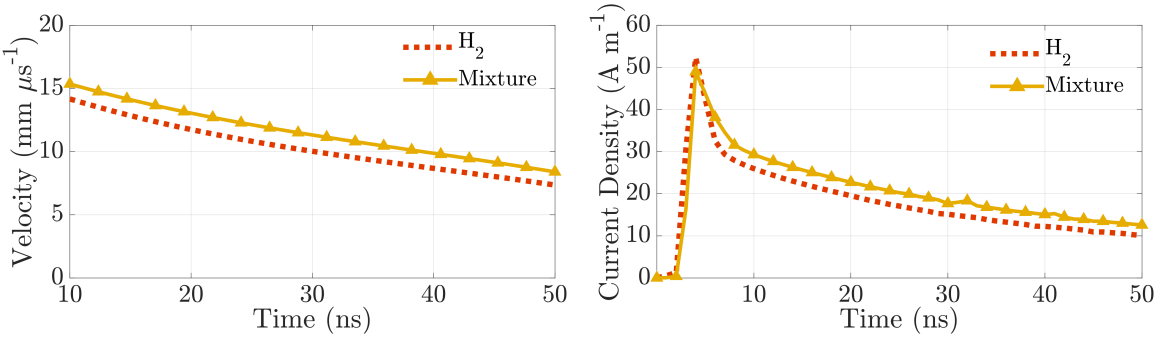

Figure 6.23: Plasma velocity (left) fitted to 3rd order polynomial and current density (right) along exposed electrode, in pure H_2 and mixture.

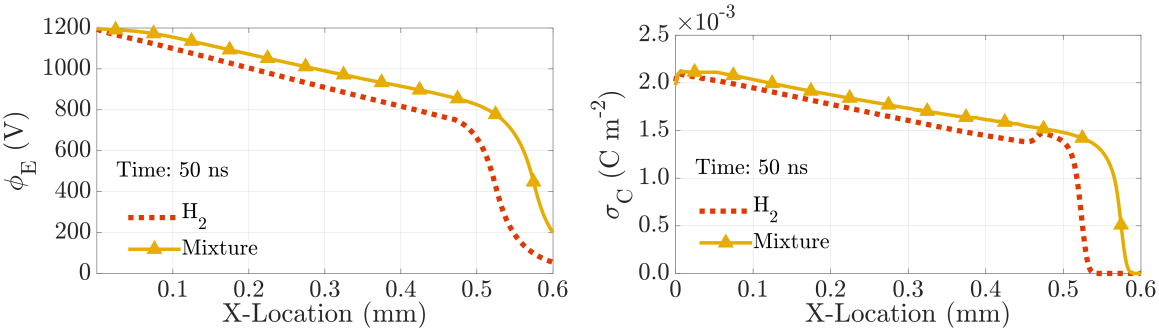

Figure 6.24: Electric potential (left) and surface charge density (right) along dielectric surface in H_2 and mixture at 50 ns.

After 20 ns, the presence of species other than H_2 become evident, notably in the trail where higher ion densities are maintained. Figures 6.25 and 6.26 show the isolated ion density of each individual species to better illustrate how the full plasma cloud is composed. In Figure 6.25, the H_2^+ ions make up the bulk of the plasma head along with the top half of the plasma trail. Because H_2 has a higher coefficient of ionization for lower electric field strengths (see Figure 6.1), it is more readily ionized in areas of lower electron density, i.e. the top region of the trail. Additionally, H_2^+ ions extend slightly further than any other ion species, aiding in downstream movement of the plasma. Conversely, the plasma trail is largely compose of H_2O^+ ions, attributed to the low coefficient of recombination discussed earlier. As such, H_2 is responsible for pushing the ions downstream and facilitating high rates of ionization in the plasma head, while H_2O is responsible for ions lingering above the dielectric surface. Given that the mixture contains relatively high percentages of H_2 and H_2O, it is expected that the traits observed in their single-species simulations would be the dominant features in the mixture.

Figure 6.26 displays the remaining species found in the mixture. Despite similar proportions of CO and H_2O, CO^+ density is limited by the mechanisms discussed in pure CO, i.e. limited CO ionization. Although CO has been shown to readily ionize in the presence of H_2, CO makes up only 13.08% of the mixture. This small CO proportion along with a relatively high coefficient of recombination ($6.8 \times 10^{-13}\,\mathrm{m^3\,s^{-1}}$ [680%]) restricts the CO^+ density to the head of the plasma, where rates of ionization are highest for all species. Similarly, the mixture contains only 2.05% CO_2, which also possesses a very high coefficient of recombination ($11.06 \times 10^{-13}\,\mathrm{m^3\,s^{-1}}$ [1106%]), restricting CO_2^+ ion density to an even smaller region within the plasma head.

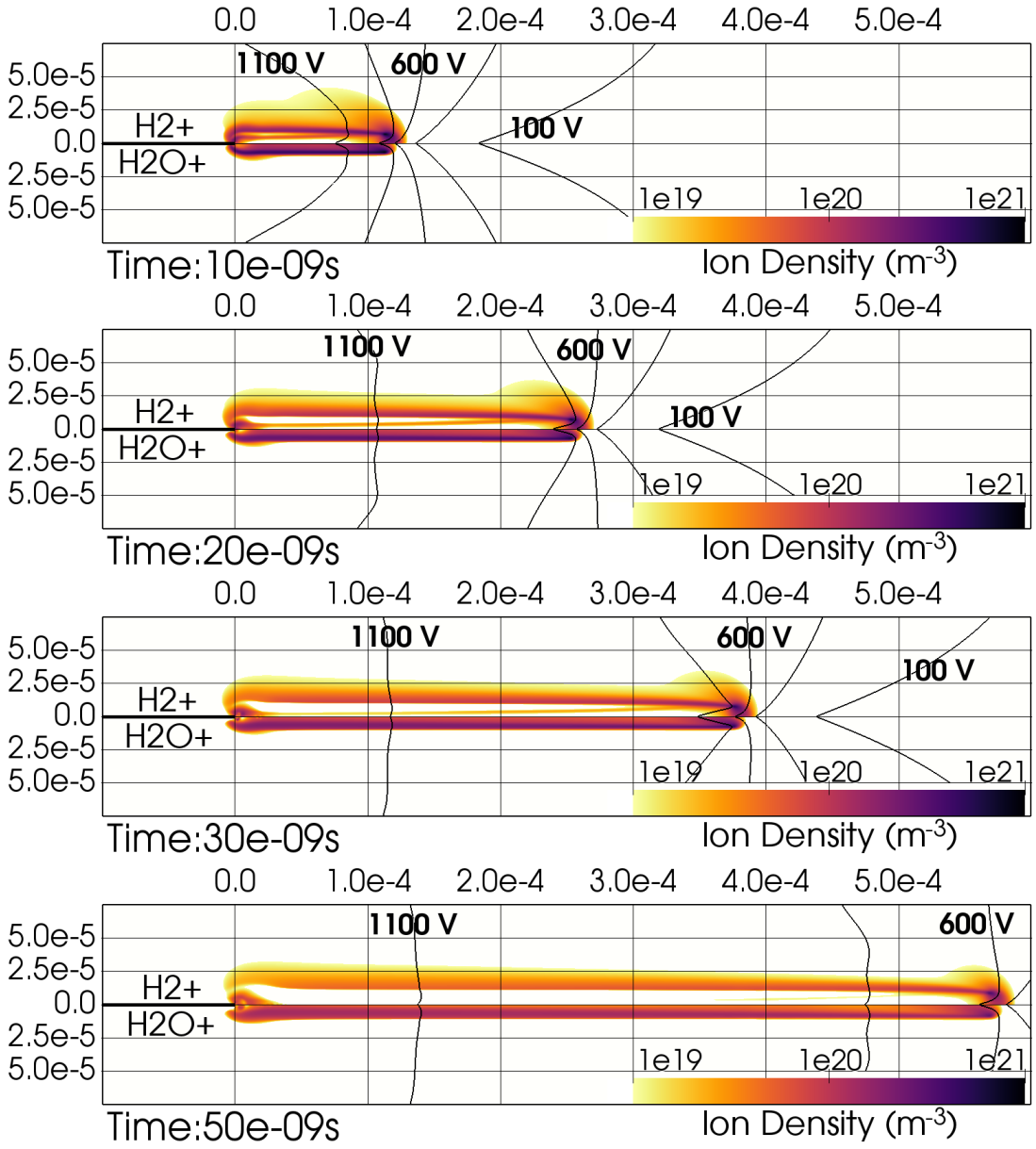

Figure 6.25: Isolated ion species within mixture. H_2^+ (top) and H_2O^+ (bottom) ion densities.

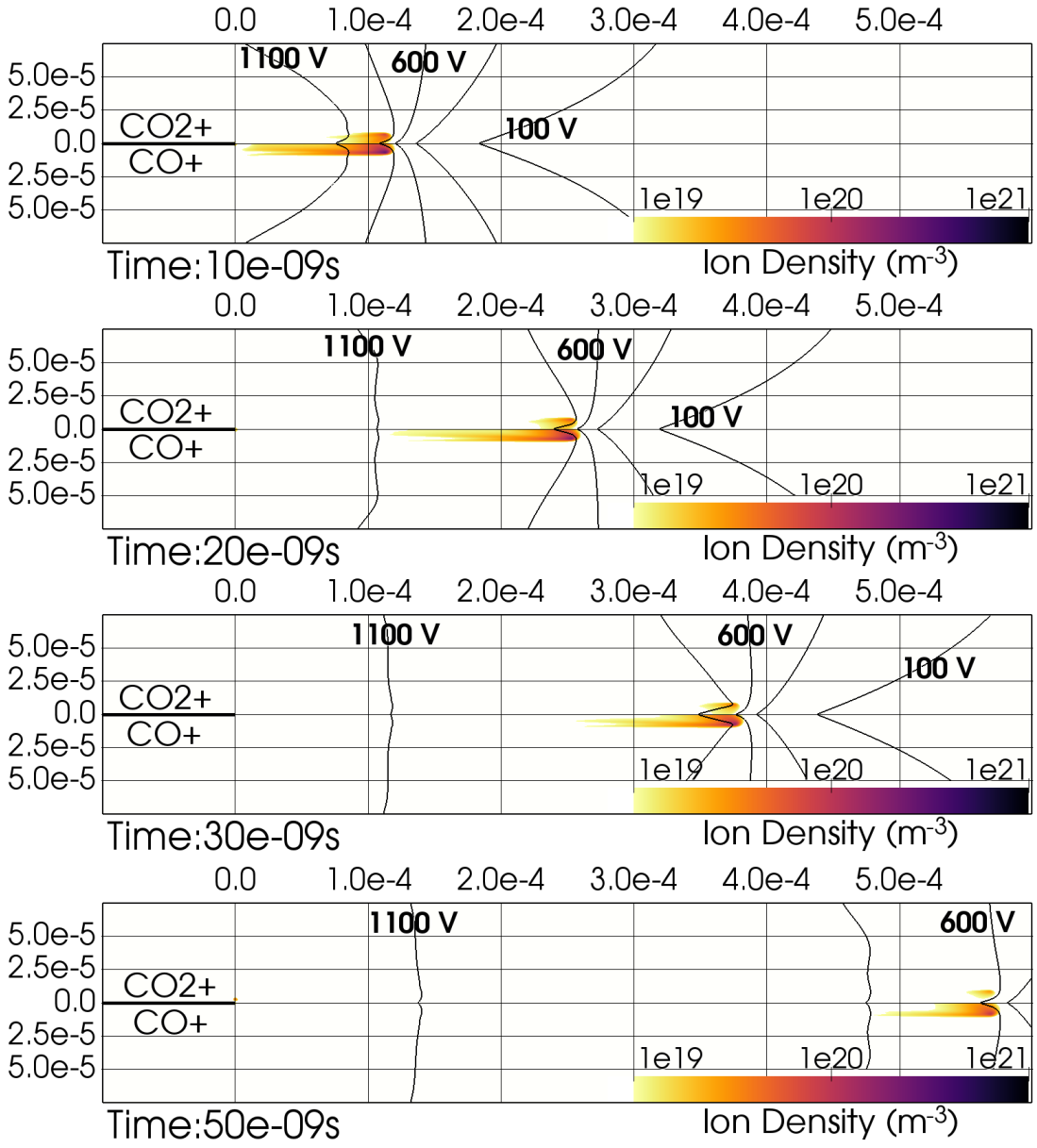

Figure 6.26: Isolated ion species within mixture. CO_2^+ (top) and CO^+ (bottom) ion densities.

6.3 Summary

Table 6.3 condenses the peak ion densities and average velocities quoted in the discussion of results, along with the associated ion properties of ion mobility and coefficient of recombination. All values are normalized with respect to the case of pure N_2, with extrema highlighted in bold. Figure 6.27 is included to reference the differing ionization coefficient functions. The relationship between ion mobility and plasma movement is reiterated, as average velocity increases with increasing mobility. However, other factors must also influence plasma velocity as well, as the exhaust mixture

Table 6.3: Salient features of plasma development in each simulation. Average velocities are not listed for cases where a defined plasma front was indiscernible.

Normalized Results				
Species	**Ion Properties**		**Peak Ion Density**	**Average Velocity**
	$\boldsymbol{\mu_+}$	$\boldsymbol{\beta_i}$		
N_2	1	1	1	1
H_2O	**0.66**	**0.66**	**2.14**	**0.84**
CO_2	0.72	**11.06**	1.35	0.94
CO	0.89	6.8	**0.02**	-
H_2	**4.85**	2.8	0.41	2.21
Fictitious N_2	**4.85**	1	0.64	2.12
CO:H_2 (95:5)	-	-	0.13	-
CO:H_2 (60:40)	-	-	0.31	1.55
Exhaust Mixture	-	-	0.58	**2.49**

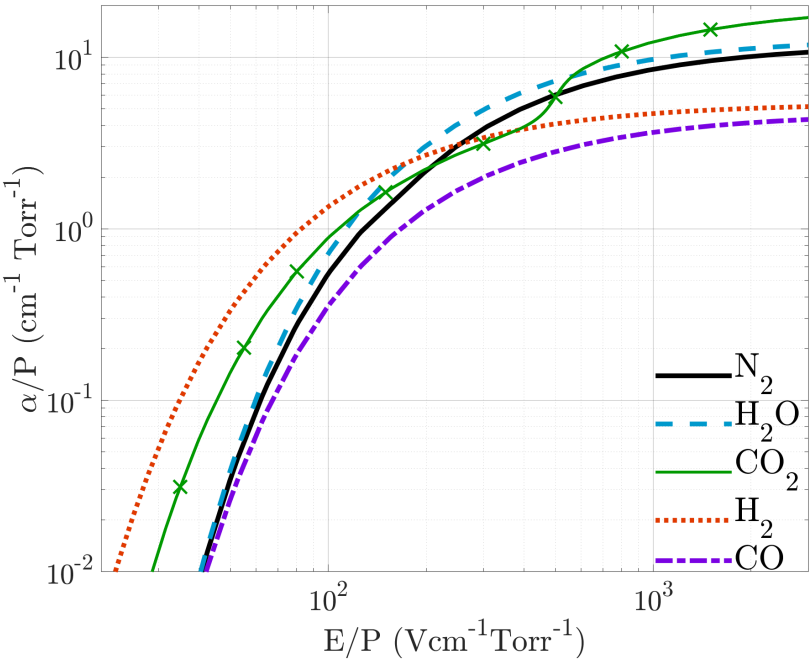

Figure 6.27: Ionization Coefficient, α_i as a function of reduced electric field, E/P. Discontinuities in N_2 and CO_2 due to the change of coefficients A and B in differing regions of applicability. Limits of the chart coincide with the range of E/P simulated.

propagates furthest in 50 ns despite 30% of the mixture containing the low ion mobility species of H_2O, CO and CO_2. As expected, a heightened rate of recombination is shown to limit ion densities as demonstrated by CO_2, while a lessened rate of recombination leads to large ion densities in H_2O. Multi-species gases offer unique results depending on the proportions of their constituents. Previously inhibited ionization of CO is promoted by the presence of H_2, and the degree of this effect increases with increasing H_2 percentage. Mixtures that are able to sufficiently ionize will take on characteristics of its main components, as seen in the high velocity of the exhaust mixture due to H_2^+ mobility.

Chapter 7

Conclusions and Recommendations

7.1 Conclusions

The current work covers the relevant literature on numerical modelling of DBD plasma actuators in a range of different configurations and operating conditions, along with a brief review of experimental work on the topic. A fluid model developed by Murzionak et al. [30] using OpenFOAM software has been validated by the previous works of Boeuf and Pitchford, and Abdollahzadeh et al. [27, 28], which is then adapted for plasma modelling in various pure gases and mixtures. The study finds that, given an applied voltage of 1200 V, pure gases of CO_2, H_2O and H_2 exhibit similar ion densities to that of pure N_2, while the ionization of CO is notably inhibited or delayed. The coefficients of recombination, β, are shown to impact the structure of the plasma region, with lower coefficients allowing for high ion densities to linger in the plasma trail. Despite ion mobility, μ_+, being much smaller relative to electron mobility, unique values of μ_+ are shown to be the dominant factor in altering the movement of plasma downstream along the dielectric surface. This is best illustrated by modelling a fictitious N_2 species with an inflated μ_+ value and observing the marked increase in plasma velocity.

Mixtures of different species are shown to be heavily dependent on the proportion of components in the mixture, as expected. CO mixed with H_2 allows for an increase

in the rate of CO^+ generation for mixtures with as little as 5% H_2. Higher percentages of H_2 mixed with CO causes further CO^+ generation, though the plasma begins to exhibit characteristics associated with H_2. A more comprehensive post-combustion fluid is modelled, in which the plasma exhibits qualities unique to its component species. Plasma velocity is largely dependent on the highest ion mobility found within the mixture, as more mobile ions will move along the dielectric surface quicker and facilitate further ionization of all species in the plasma head. The structure of the plasma is dependent on the proportion of each component gas. As shown in the mixture of H_2, H_2O, CO and CO_2, species typical of a post combustion environment, a relatively large proportion of H_2O allows for ion densities to remain high in the trailing region due to the low coefficient of recombination of H_2O^+, while the effect of a high coefficient of recombination in CO_2^+ is negated by the small proportion of CO_2. Ultimately, a DBD actuator operating within a typical post combustion environment would be able to generate a region of plasma comparable to that generated in air, while also inducing relatively high plasma velocities.

7.2 Recommendations

The model used in the scope of this work also has its limitations, introduced largely to improve upon computational costs. Several features that would otherwise be present in the working fluid, such as excitation, dissociation and higher degree ionization, are not considered. Most notably, negative ions are not considered, which have been shown to have a noticeable impact on the plasma behaviour. While negative ions are the product of secondary ionization reactions in the gases modelled here, negative

oxygen ions can be generated in appreciable densities for fluids containing oxygen. The inclusion of oxygen would be crucial in expanding the current model to a more comprehensive post-combustion environment. Operating conditions (temperature, pressure, etc.) are also assumed constant which prevents the model from offering insight into how the plasma alters the bulk flow. Additionally, plasma actuation depends largely on the voltage function applied to the electrodes. A parametric analysis of various voltages (DC, AC, pulsed voltage functions) would need to be explored if actuation in these gases is to be optimized. The current model shows promise in extending the plasma to non-quiescent conditions, by which the impact of plasma actuation on velocity profiles, pressure distributions and heat transfer properties might be explored. The current work is successful in illustrating the salient features of plasma generated through dielectric barrier discharge for various species. While an air-like working fluid is commonly assumed, the unique properties of individual gases are shown here to alter the behaviour of the plasma, and these properties must be considered if a reliable model is to be developed for specific environments.

Bibliography

[1] T. Ecker, S. Karl, E. Dumont, S. Stappert, and D. Krause, "Numerical study on the thermal loads during a supersonic rocket retropropulsion maneuver," *Journal of Spacecraft and Rockets*, vol. 57, no. 1, pp. 131–146, 2020. [Online]. Available: https://doi.org/10.2514/1.A34486

[2] F. A. Zainuddin and N. Md Daud, "A review on dielectric barrier discharge (dbd) plasma actuator in aeronautics applications," *Journal of Advanced Research in Fluid Mechanics and Thermal Sciences*, vol. 48, no. 2, p. 125–132, Dec. 2020. [Online]. Available: https://akademiabaru.com/submit/index.php/arfmts/article/view/2270

[3] J. Kriegseis, B. Simon, and S. Grundmann, "Towards in-flight applications? a review on dielectric barrier discharge-based boundary layer control," *Applied Mechanics Reviews*, vol. 68, no. 2, Jul. 2016, 020802. [Online]. Available: https://doi.org/10.1115/1.4033570

[4] E. Moreau, R. Sosa, and G. Artana, "Electric wind produced by surface plasma actuators: a new dielectric barrier discharge based on a three-electrode geometry," *Journal of Physics D: Applied Physics*, vol. 41, no. 11, p. 115204, May. 2008. [Online]. Available: https://doi.org/10.1088/0022-3727/41/11/115204

[5] J. P. Boeuf, Y. Lagmich, T. Unfer, T. Callegari, and L. C. Pitchford, "Electrohydrodynamic force in dielectric barrier discharge plasma actuators,"

Journal of Physics D: Applied Physics, vol. 40, no. 3, pp. 652–662, Jan. 2007. [Online]. Available: https://doi.org/10.1088/0022-3727/40/3/s03

[6] S. Grundmann and C. Tropea, "Experimental damping of boundary-layer oscillations using dbd plasma actuators," *International Journal of Heat and Fluid Flow*, vol. 30, no. 3, pp. 394–402, 2009, the Seventh International Symposium on Engineering Turbulence Modelling and Measurements, ETMM7. [Online]. Available: https://www.sciencedirect.com/science/article/pii/S0142727X09000575

[7] A. Seraudie, O. Vermeersch, and D. Arnal, "Dbd plasma actuator effect on a 2d model laminar boundary layer. transition delay under ionic wind effect." in *29th AIAA Applied Aerodynamics Conference*, 2011. [Online]. Available: https://arc.aiaa.org/doi/abs/10.2514/6.2011-3515

[8] N. Szulga, O. Vermeersch, M. Forte, and G. Casalis, "Experimental and numerical study of boundary layer transition control over an airfoil using a dbd plasma actuator," *Procedia IUTAM*, vol. 14, pp. 403–412, 2015, iUTAM ABCM Symposium on Laminar Turbulent Transition. [Online]. Available: https://www.sciencedirect.com/science/article/pii/S2210983815000930

[9] A. Duchmann, "Boundary-layer stabilization with dielectric barrier discharge plasmas for free-flight application," Ph.D. dissertation, Technical University of Darmstadt, Dec. 2012. [Online]. Available: https://tuprints.ulb.tu-darmstadt.de/3351/7/DissDuchmann.pdf

[10] W. Shyy, B. Jayaraman, and A. Andersson, "Modeling of glow discharge-induced fluid dynamics," *Journal of Applied Physics*, vol. 92, no. 11, pp. 6434–6443, Jan. 2002. [Online]. Available: https://doi.org/10.1063/1.1515103

[11] J. Roth, D. Sherman, and S. Wilkinson, "Boundary layer flow control with a one atmosphere uniform glow discharge surface plasma," in *36th AIAA Aerospace Sciences Meeting and Exhibit*, 1998. [Online]. Available: https://arc.aiaa.org/doi/abs/10.2514/6.1998-328

[12] J. R. Roth, D. M. Sherman, and S. P. Wilkinson, "Electrohydrodynamic flow control with a glow-discharge surface plasma," *AIAA Journal*, vol. 38, no. 7, pp. 1166–1172, 2000. [Online]. Available: https://doi.org/10.2514/2.1110

[13] J. R. Roth, *Industrial Plasma Engineering: Volume 2: Applications to Nonthermal Plasma Processing*. Taylor & Francis [Imprint], Aug. 2001. [Online]. Available: https://doi.org/10.1201/9781420034127

[14] T. Corke, E. Jumper, M. Post, D. Orlov, and T. McLaughlin, "Application of weakly-ionized plasmas as wing flow-control devices," in *40th AIAA Aerospace Sciences Meeting & Exhibit*, 2002. [Online]. Available: https://arc.aiaa.org/doi/abs/10.2514/6.2002-350

[15] Y. Suzen, G. Huang, J. Jacob, and D. Ashpis, "Numerical simulations of plasma based flow control applications," in *35th AIAA Fluid Dynamics Conference and Exhibit*, 2005. [Online]. Available: https://arc.aiaa.org/doi/abs/10.2514/6.2005-4633

[16] T. Brauner, S. Laizet, N. Benard, and E. Moreau, "Modelling of dielectric barrier discharge plasma actuators for direct numerical simulations," in *8th AIAA Flow Control Conference*, 2016. [Online]. Available: https://arc.aiaa.org/doi/abs/10.2514/6.2016-3774

[17] D. Orlov, T. Corke, and M. Patel, "Electric circuit model for aerodynamic plasma actuator," in *44th AIAA Aerospace Sciences Meeting and Exhibit*, 2006. [Online]. Available: https://arc.aiaa.org/doi/abs/10.2514/6.2006-1206

[18] Y. Suzen, G. Huang, and D. Ashpis, "Numerical simulations of flow separation control in low-pressure turbines using plasma actuators," in *45th AIAA Aerospace Sciences Meeting and Exhibit*, 2007. [Online]. Available: https://arc.aiaa.org/doi/abs/10.2514/6.2007-937

[19] R. D. Whalley and K.-S. Choi, "Turbulent boundary-layer control with spanwise travelling waves," *Journal of Physics: Conference Series*, vol. 318, no. 2, p. 022039, Dec. 2011. [Online]. Available: https://doi.org/10.1088/1742-6596/318/2/022039

[20] R. Whalley and K.-S. Choi, "The starting vortex in quiescent air induced by dielectric-barrier-discharge plasma," *Journal of Fluid Mechanics*, vol. 703, pp. 192–203, Jul. 2012. [Online]. Available: https://doi.org/10.1017/jfm.2012.206

[21] R. Khoshkhoo and A. Jahangirian, "Numerical simulation of flow separation control using multiple dbd plasma actuators," *Journal of Applied Fluid Mechanics*, vol. 9, no. 4, pp. 1865–1875, Oct. 2016. [Online]. Available: https://www.jafmonline.net/article_1757.html

[22] B. Jayaraman and W. Shyy, "Flow control and thermal management using dielectric glow discharge concepts," in *33rd AIAA Fluid Dynamics Conference and Exhibit*, 2003. [Online]. Available: https://arc.aiaa.org/doi/abs/10.2514/6.2003-3712

[23] I. H. Ibrahim and M. Skote, "Simulating plasma actuators in a channel flow configuration by utilizing the modified suzen–huang model," *Computers and Fluids*, vol. 99, p. 144–155, Jul. 2014. [Online]. Available: https://www.sciencedirect.com/science/article/pii/S0045793014001558

[24] Y. Babou, E. N. Martin, and P. F. Peña, "Simple body force model for dielectric barrier discharge plasma actuator," in *7th European Conference for Aeronautics and Aerospace Sciences*, 2017. [Online]. Available: https://www.eucass.eu/doi/EUCASS2017-122.pdf

[25] G. Font and W. Morgan, "Plasma discharges in atmospheric pressure oxygen for boundary layer separation control," in *35th AIAA Fluid Dynamics Conference and Exhibit*, 2005. [Online]. Available: https://arc.aiaa.org/doi/abs/10.2514/6.2005-4632

[26] S. Ebato, Y. Ogino, and N. Ohnishi, "Numerical analysis of momentum transfer process in dbd plasma actuator," in *41st Plasmadynamics and Lasers Conference*, 2010. [Online]. Available: https://arc.aiaa.org/doi/abs/10.2514/6.2010-4635

[27] J. P. Boeuf and L. C. Pitchford, "Electrohydrodynamic force and aerodynamic flow acceleration in surface dielectric barrier discharge," *Journal of Applied*

Physics, vol. 97, pp. 103 307–103 307, 05 2005. [Online]. Available: https://doi.org/10.1063/1.1901841

[28] M. Abdollahzadeh, J. Páscoa, and P. Oliveira, "Two-dimensional numerical modeling of interaction of micro-shock wave generated by nanosecond plasma actuators and transonic flow," *Journal of Computational and Applied Mathematics*, vol. 270, pp. 401 – 416, 2014, fourth International Conference on Finite Element Methods in Engineering and Sciences (FEMTEC 2013). [Online]. Available: http://www.sciencedirect.com/science/article/pii/S0377042713007036

[29] H. Nishida and T. Abe, "Numerical analysis of plasma evolution on dielectric barrier discharge plasma actuator," *Journal of Applied Physics*, vol. 110, no. 1, p. 013302, 2011. [Online]. Available: https://doi.org/10.1063/1.3603001

[30] A. Murzionak, J. Etele, and R. Pimentel, "Study of surface dielectric barrier discharge plasma actuator in supersonic flow," in *2018 AIAA Aerospace Sciences Meeting*, 2018. [Online]. Available: https://arc.aiaa.org/doi/abs/10.2514/6.2018-1294

[31] A. Mushyam, F. Rodrigues, and J. Páscoa, "A plasma-fluid model for ehd flow in dbd actuators and experimental validation," *International Journal for Numerical Methods in Fluids*, vol. 90, no. 3, pp. 115–139, Jan. 2019. [Online]. Available: https://onlinelibrary.wiley.com/doi/abs/10.1002/fld.4714

[32] M. Kotsonis, S. Ghaemi, L. Veldhuis, and F. Scarano, "Measurement of the body force field of plasma actuators," *Journal of Physics D:*

Applied Physics, vol. 44, p. 045204, Jan. 2011. [Online]. Available: https://doi.org/10.1088/0022-3727/44/4/045204

[33] T. Unfer and J. P. Boeuf, "Modelling of a nanosecond surface discharge actuator," *Journal of Physics D: Applied Physics*, vol. 42, no. 19, p. 194017, Sep. 2009. [Online]. Available: https://doi.org/10.1088%2F0022-3727%2F42%2F19%2F194017

[34] K. P. Singh and S. Roy, "Modeling plasma actuators with air chemistry for effective flow control," *Journal of Applied Physics*, vol. 101, no. 12, p. 123308, 2007. [Online]. Available: https://doi.org/10.1063/1.2749467

[35] F. Rogier, G. Dufour, and K. Kourtzanidis, "Numerical simulation of sinusoidal dbd actuators and comparison with experiments," in *45th AIAA Plasmadynamics and Lasers Conference*, 2014. [Online]. Available: https://arc.aiaa.org/doi/abs/10.2514/6.2014-2808

[36] R. Durscher and S. Roy, "Evaluation of thrust measurement techniques for dielectric barrier discharge actuators," *Exp. Fluids*, vol. 53, pp. 1165–1176, Oct. 2012. [Online]. Available: https://doi.org/10.1007/s00348-012-1349-6

[37] R. Durscher and S. Roy, "Force measurement techniques and preliminary results using aerogels and ferroelectrics for dielectric barrier discharge actuators," in *42nd AIAA Plasmadynamics and Lasers Conference*, 2011. [Online]. Available: https://arc.aiaa.org/doi/abs/10.2514/6.2011-3735

[38] G. Dufour and F. Rogier, "Numerical modeling of dielectric barrier discharge based plasma actuators for flow control : the copaier/cedre

example," *Aerospace Lab*, no. 10, Dec. 2015. [Online]. Available: https://hal.archives-ouvertes.fr/hal-01270823

[39] H. D. Smyth and E. C. G. Stueckelberg, "The ionization of carbon dioxide by electron impact," *Phys. Rev.*, vol. 36, pp. 472–477, Aug. 1930. [Online]. Available: https://link.aps.org/doi/10.1103/PhysRev.36.472

[40] N. Bussières and P. Marmet, "Ionization and dissociative ionization of co2 by electron impact," *Canadian Journal of Physics*, vol. 55, no. 21, pp. 1889–1897, 02 1977. [Online]. Available: https://doi.org/10.1139/p77-230

[41] T. R. Hogness and R. W. Harkness, "The ionization of carbon monoxide by controlled electron impact, interpreted by the mass spectrograph," *Phys. Rev.*, vol. 32, pp. 936–941, Dec. 1928. [Online]. Available: https://link.aps.org/doi/10.1103/PhysRev.32.936

[42] T. R. Hogness and E. G. Lunn, "The ionization of hydrogen by electron impact as interpreted by positive ray analysis," *Phys. Rev.*, vol. 26, pp. 44–55, Jul. 1925. [Online]. Available: https://link.aps.org/doi/10.1103/PhysRev.26.44

[43] T. J. Dolan, "Electron and ion collisions with water vapour," pp. 4–8, Jan. 1993. [Online]. Available: https://doi.org/10.1088/0022-3727/26/1/002

[44] H. D. Smyth and D. W. Mueller, "The ionization of water vapor by electron impact," *Phys. Rev.*, vol. 43, pp. 116–120, Jan. 1933. [Online]. Available: https://link.aps.org/doi/10.1103/PhysRev.43.116

[45] S. Sato, M. Takahashi, and N. Ohnishi, "Induced flow simulation with detailed discharge modeling in dielectric-barrier-discharge plasma actuator,"

in *2018 AIAA Aerospace Sciences Meeting*, 2018. [Online]. Available: https://arc.aiaa.org/doi/abs/10.2514/6.2018-1293

[46] Y. Raizer, V. Kisin, and J. Allen, *Gas Discharge Physics*. Springer Berlin Heidelberg, 2011. [Online]. Available: https://books.google.ca/books?id=zd-KMAEACAAJ

[47] M. S. Bhalla and J. D. Craggs, "Measurement of ionization and attachment coefficients in carbon dioxide in uniform fields," *Proceedings of the Physical Society*, vol. 76, no. 3, pp. 369–377, Sep. 1960. [Online]. Available: https://doi.org/10.1088%2F0370-1328%2F76%2F3%2F307

[48] S. Avtaeva, A. General, and V. Kel'man, "Kinetic model for low-density non-stationary gas discharge in water vapour," *Journal of Physics D: Applied Physics*, vol. 43, no. 31, p. 315201, Jul. 2010. [Online]. Available: https://doi.org/10.1088/0022-3727/43/31/315201

[49] Kaye and Laby, "Table of physical & chemical constants. 4.4 free electrons and ions in gases." 2005. [Online]. Available: https://www.npl.co.uk/resources

[50] R. E. Center, "Carbon monoxide laser," AVCO Everett Research Lab Inc, Tech. Rep., 1973. [Online]. Available: https://apps.dtic.mil/sti/citations/AD0759755

[51] J. de Urquijo, A. Bekstein, G. Ruiz-Vargas, and F. J. Gordillo-Vázquez, "Drift and clustering of daughter negative ions of h2o in parent gas," *Journal of Physics D: Applied Physics*, vol. 46, no. 3, p. 035201, Dec. 2012. [Online]. Available: https://doi.org/10.1088%2F0022-3727%2F46%2F3%2F035201

[52] P. Encarnação, A. Cortez, R. Veenhof, P. Neves, F. Santos, A. Trindade, F. Borges, and C. Conde, "Experimental ion mobility measurements in ne-CO2and CO2-n2mixtures," *Journal of Instrumentation*, vol. 11, no. 05, pp. P05 005–P05 005, May. 2016. [Online]. Available: https://doi.org/10.1088%2F1748-0221%2F11%2F05%2Fp05005

[53] S. Surzhikov, "Numerical study of acceleration of the hydrogen ions in the penning discharge at pressures around 1 torr," in *55th AIAA Aerospace Sciences Meeting*, 2017. [Online]. Available: https://arc.aiaa.org/doi/abs/10.2514/6.2017-0155

[54] M. Vass, I. Korolov, D. Loffhagen, N. Pinhão, and Z. Donkó, "Electron transport parameters in CO2: scanning drift tube measurements and kinetic computations," *Plasma Sources Science and Technology*, vol. 26, no. 6, p. 065007, May. 2017. [Online]. Available: https://doi.org/10.1088%2F1361-6595%2Faa6789

[55] W. Roznerski and K. Leja, "Electron drift velocity in hydrogen, nitrogen, oxygen, carbon monoxide, carbon dioxide and air at moderate e/n," *Journal of Physics D: Applied Physics*, vol. 17, no. 2, pp. 279–285, Feb. 1984. [Online]. Available: https://doi.org/10.1088%2F0022-3727%2F17%2F2%2F012

[56] H. T. Saelee and J. Lucas, "Simulation of electron swarm motion in hydrogen and carbon monoxide for high e/n," *Journal of Physics D: Applied Physics*, vol. 10, no. 3, pp. 343–354, Feb. 1977. [Online]. Available: https://doi.org/10.1088%2F0022-3727%2F10%2F3%2F014

[57] G. Raju, *Gaseous Electronics: Tables, Atoms, and Molecules*. CRC Press, 2018. [Online]. Available: https://books.google.ca/books?id=B6LsDwAAQBAJ

[58] OpenFOAM, "Openfoam v5 user guide," 2016. [Online]. Available: https://cfd.direct/openfoam/user-guide

[59] ParaView, "Paraview documentation," 2020. [Online]. Available: https://docs.paraview.org/en/latest/index.html

[60] MATLAB, *version 9.9.0 (R2020b)*, 2020. [Online]. Available: https://www.mathworks.com/help/matlab/index.html

[61] "High level programming in openfoam® building blocks." [Online]. Available: http://www.wolfdynamics.com/training/introOF8/supplement_programming_openfoam.pdf

[62] P. Roache, *Fundamentals of Computational Fluid Dynamics*. Hermosa Publishers, 1998. [Online]. Available: https://books.google.ca/books?id=rhh2QgAACAAJ

[63] L. E. Schwer, "Is your mesh refined enough? estimating discretization error using gci," in *7th LS-DYNA Anwenderforum*, 2008. [Online]. Available: https://www.dynamore.de/en/downloads/papers/08-forum